ALMA MATER STUDIORUM – UNIVERSITÀ DI BOLOGNA
DOTTORATO IN BIOINGEGNERIA
CICLO XXIV
Settore Scientifico Disciplinare: ING-INF/06

Variability analysis of discrete event series and wavefront patterns in surface electrocardiogram: contributions to psychophysiological and clinical research

PhD Candidate:
Luigi Yuri Di Marco

Supervisor:
Chiar.mo Prof. Angelo Cappello

Co-supervisor:
Prof. Lorenzo Chiari

Reviewers:
Chiar.mo Prof. Mauro Ursino
Philip Langley, PhD

Final Examination Year 2012

Summary

Thesis Overview

Background

The surface electrocardiogram (ECG) is the recording of voltage variations on the body surface, generated by the action potentials of the excitable cardiac cells. The heartbeat in the ECG displays a series of wavefronts whose morphology and timing convey information which is used for the identification of electrical abnormalities and the diagnosis of abnormal cardiac rhythms.

Electrical abnormalities (arrhythmias) may be grouped in two main categories: those which make the heart pump too slowly (*bradycardia*), and those with make the heart pump too quickly (*tachycardia*). The electrical impulse may also be interrupted causing conduction blockages, or generated outside the natural pacemaker, the sinoatrial node, generating ectopic beats. In some cases, the electrical impulse can also break down into separate wavefronts which circulate quasi-randomly over the cardiac muscle (myocardium), a phenomenon known as fibrillation.

However, the clinical use of the ECG extends beyond arrhythmias identification. It can reveal metabolic abnormalities of the myocardium, the most medically relevant being ischemia, a condition in which part of the cardiac tissue is not adequately supplied with oxygen, due to insufficient blood flow, often caused by disease of the coronary arteries. Other metabolic abnormalities which cause characteristic changes in the ECG include impaired serum concentration of electrolytes (potassium, calcium, magnesium). Therapeutic drugs can also alter the appearance of the ECG. Lastly, the ECG can reveal abnormalities of the geometry of the heart, such as the enlargement of a portion of the myocardium (hypertrophy), or the presence of a region of dead and scarred cells (infarction).

Complementary to the analysis of ECG morphology, is that of temporal changes of ECG characteristics, such as the inter-beat interval (IBI). Fluctuations in heart rate reflect autonomic modulation and have prognostic significance in pathological states. The analysis of heart rate variability (HRV) has been proposed in the assessment of the autonomic function, in risk quantification in a wide variety of cardiac and non-cardiac disorders such as stroke, multiple sclerosis, end stage renal disease, neonatal distress, diabetes mellitus, myocardial infarction (MI), and congestive heart failure. In particular, HRV analysis has been applied to post MI risk stratification assessment. Recent studies have also suggested that HRV can be used to measure physiological changes in a number of psychiatric illnesses such as major depression, generalized anxiety disorder, schizophrenia, panic disorder and post-traumatic stress disorder.

Moreover, in recent years, the interest for HRV analysis has extended from clinical practice and research to cognitive psychophysiology. Several studies have related short-term HRV to memory performance, mental workload and sustained attention.

The development and advancement of signal processing technologies over the past decades has made it possible to automate operations such as heartbeat detection and classification, time markers (fiducial points) placement in the ECG, intervals and amplitude measurements, relieving physicians and healthcare operators in general from time-consuming and tedious work, improving efficiency and reliability by reducing inter-operator variability, and increasing repeatability of measurements.

However, in spite of being a relatively old field, many key challenges remain in ECG signal processing today, such as reliable measurements of critical intervals, reliable artifact detection in ambulatory monitoring, in-band signal filtering (source separation), and non-linear, non-stationary dynamics management.

Aim

The aim of this PhD thesis was to analyze the variability of surface ECG derived rhythms at two different time scales: the discrete-event time scale, typical of beat-by-beat extracted features, and the "continuous" time scale of separated (in-band filtered) sources in the ECG, in selected scenarios relevant to psychophysiological and clinical research, respectively.

In the first case, the discrete event series (DES) of IBI was considered. HRV analysis was carried out in the time, frequency, and joint time-frequency domain, complemented by non-linear dynamics analysis, with the goal of assessing psychophysiological workload in response to working memory engaging tasks. This work was part of the project: "Cognitive Adaptive Man-Machine Interface" (CAMMI) supported by ARTEMIS JTI initiative of the European Union, EU-JTI grant No. 100008.

In the second case, the atrial activation signal (AA) from atrial fibrillation (AF) recordings was considered. The signal was estimated from body surface potential maps (BSPM). The goal was to analyze the temporal variability of spatial organization (complexity) and spectral distribution of AF, to propose an automatic implementation of the analysis, and to assess the applicability to reduced lead-sets, to potentially support clinical decision making in AF ablation therapy.

Results

Variability analysis of discrete event series

Psycho-physiological workload (PPW) in response to a memory search task (Sternberg 1966) in healthy young subjects was assessed by means of regularity and joint time-frequency analyses of non stationary heart rate variability.

In fourteen healthy young subjects PPW was assessed by means of standard HRV indices complemented with joint time-frequency and regularity analyses of the inter-beat interval (IBI) series. A superior ability of regularity index (SampEn) in discriminating performance (task execution) from rest; and instantaneous energy variability ($\mathrm{IEV}_{\mathrm{LF+HF}}$) in discriminating difficult tasks from other sessions (rest and easy tasks) was shown, suggesting a potential use of the proposed indices in discriminating PPW levels in response to varying task difficulty.

Variability analysis of wavefront patterns

A novel source-cancellation method based on morphology clustering of the ventricular depolarization interval (QRS-T segment) was proposed for the estimation of the atrial activation wavefront in AF. The proposed method showed significant improvement in ventricular activity cancellation with respect to established single-lead approaches in BSPM recordings, and reliable estimation of AF dominant frequency (DF). In a study on 14 persistent AF recordings of BSPM, it was compared to established blind source separation methods showing no significant differences in DF estimation, while preserving the characteristic spatial resolution of single-lead approaches.

The analysis of variability was extended beyond DF estimation. Combined analysis of spatial complexity, temporal and spectral variability of atrial activation during AF was presented for BSPM recordings, based on a fully automated procedure, built on wavelet-transform based ECG delineation and principal component analysis (PCA).

In 21 patients with persistent AF, it was shown that higher spectral concentration (SC) was associated with reduced temporal variability of spectral distribution. This finding suggests that with higher values of SC, a shorter observation time is required to collect spectral distribution, from which the dominant atrial fibrillatory rate (a recognized index of average atrial refractoriness) can be calculated. This could be time and cost effective in clinical decision-making in AF treatment. Moreover, it was shown that the results were not affected by the reduction of the number of leads, down to as few as 10 body surface potential maps (BSPM). This may suggest that a simplified setup could also be considered, further reducing the cost of the BSPM acquisition protocol or that the methods could be applied equally to standard 12-lead ECG.

Online signal processing: automatic assessment of signal quality

An algorithm for the automatic assessment of ambulatory ECG recording quality, based on single-condition decision rule (SCDR) classification, was presented. Its performance in binary classification (‘acceptable’ vs. ‘unacceptable’ recording quality for diagnostic interpretation) was assessed on a standard database of 998 records and compared to established supervised-learning classifiers (k-nearest neighbor, probabilistic neural network). After preliminary processing (pacemaker filtering, beat detection), fundamental features for signal quality assessment (baseline drift, flat line, QRS-artifact, spurious spikes, amplitude stepwise changes, noise) were extracted from joint time-frequency analysis, and used for classification.

The proposed method showed high accuracy (Sc) in automatic classification of short 12-leads ambulatory ECG recordings (Sc=92.36%, for balanced training set of 200 records (TS_1); 93.40%, for unbalanced training set of 498 records (TS_2)), higher than the best-performing supervised-learning classifier (85.34%, for TS_1; 92.20%, for TS_2), in spite of its simple logic. The ability to provide additional information (rejection reason) to the classification output, suggests the proposed method may be a useful tool in automatic quality assessment of 12-leads ambulatory ECG recordings.

Online signal processing: automatic electrocardiogram delineation

A wavelet-based ECG delineation algorithm was presented, designed for online 32-bit integer linear algebra processing, with shift/add operations replacing multiplications and divisions. The QRS detector achieved excellent performance on the standard MIT-BIH Arrhythmia database (Se=99.77%, P^+=99.86%, 109010 annotated beats) and on the European ST-T Database, (Se=99.81%, P^+=99.56%, 788050 annotated beats).

The proposed algorithm also exhibited very good accuracy in P, QRS, T delineation on the standard QT Database, where the mean error between automatic and manual annotations was lower than 1.5 samples for all the characteristic points, and the associated average standard deviations were comparable to the ones reported from previous methods. Reliability and accuracy were close to the highest among the ones obtained in other studies, in spite of a simplified structure built on integer linear algebra which makes the proposed algorithm a suitable candidate for online QRS detection and ECG delineation under strict power constraints and limited computational resources, such as in wearable devices for long-term non-diagnostic ambulatory monitoring.

Outline

This thesis focuses on the analysis of variability of discrete event time series and wavefront patterns in the surface electrocardiogram. The presentation of the work is structured in three parts (Part I: Chapters 1-3; Part II: Chapters 4-7; Part III: Chapters 8-10) as illustrated in Figure O.1.

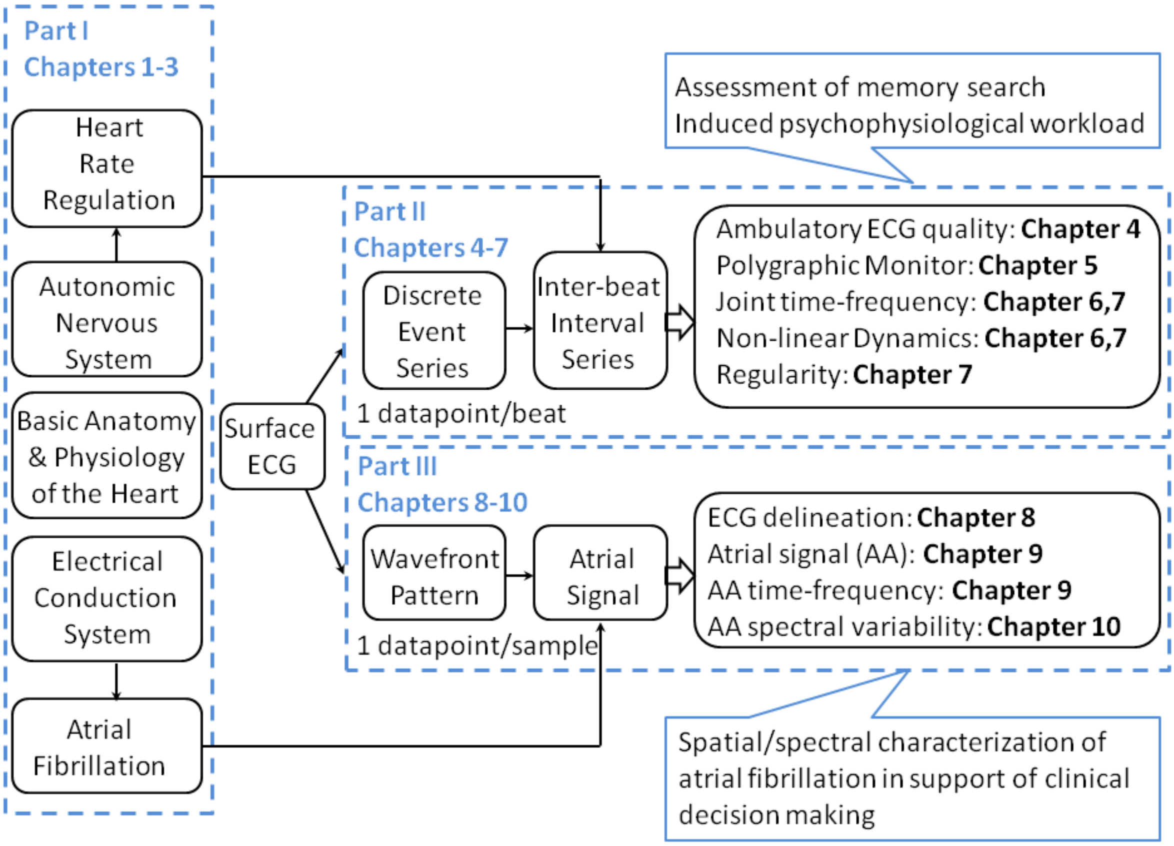

Figure O.1 Block diagram illustrating thesis outline.

Part I provides a general overview of the anatomy, physiology and electrophysiology of the heart (Chapter 1); and introduces the background and rationale of surface electrocardiogram derived rhythms (Chapters 2-3). Emphasis is given in Chapter 2 to the inter-beat interval (discrete event) and the relevance of its variability in psychophysiological and clinical research; and in Chapter 3 to the atrial activation signal (continuous wavefront) and the clinical interest of the dominant frequency in atrial fibrillation.

Part II presents the analysis of inter-beat interval (or inversely, heart rate) variability in mental workload assessment, in a memory search task. As ECG artifacts represent a major concern in ambulatory settings, the topic was addressed by a specific study on automatic quality assessment of ambulatory ECG recordings, presented in Chapter 4. Experimental setup for data acquisition is presented in Chapter 5, together with the software architecture of a real-time monitor specifically designed for data acquisition, visualization, processing and storage. In Chapters 6-7 the analysis of heart rate variability is presented. Established methods are compared (Chapter 6) on experimental data, and a novel approach based on nonlinear dynamics indices and joint time-frequency distribution of inter-beat interval variability is presented (Chapter 7).

Part III presents the analysis of the atrial activation signal (continuous wavefront) in atrial fibrillation, with emphasis on original contributions. In Chapter 8 a novel method for online electrocardiogram delineation based on wavelet-transforms and 32-bit integer linear algebra is presented. In Chapter 9 a novel method for the estimation of the atrial signal and the dominant fibrillatory rate based on surface electrocardiogram is presented. In Chapter 10 the analysis of temporal variability of spatial complexity and spectral distribution in body surface potential maps is presented, based on a novel approach built on the automatic delineation method introduced in Chapter 8. Emphasis is given to the novel finding of linear correlation between spectral concentration and temporal regularity of spectral distribution.

Part I

This part presents a general overview of the anatomy, physiology and electrophysiology of the heart (Chapter 1); and introduces the background and rationale of surface electrocardiogram derived rhythms (Chapters 2-3). Emphasis is given in Chapter 2 to the inter-beat interval (discrete event) and the relevance of its variability in psychophysiological and clinical research; and in Chapter 3 to the atrial activation signal (continuous wavefront) and the clinical interest of the dominant frequency in atrial fibrillation.

Chapter 1: Anatomy and physiology background

1.1 Anatomy and Physiology of the heart

The heart is composed of three major types of cardiac muscle: atrial muscle, ventricular muscle and specialized excitatory and conductive muscle fibers. The atrial and ventricular muscles are striated and contract in a similar way as the skeletal muscle, except the duration of contraction, which is much longer. Conversely, the specialized excitatory and conductive fibers contract only feebly because they contain few contractile fibrils.

Cardiac muscle fibers consist of individual cells arranged in a latticework, connected in series by *intercalated disks*. Electrical conductance through the intercalated disks is very high forming permeable communicating junctions (gap junctions) that allow almost free diffusion of ions. Thus, the cardiac muscle can be viewed as a *syncytium* of many cells such that when an action potential is generated in one cell it propagates to all the others. The heart is actually composed of two syncytiums: the *atrial syncytium* that constitutes the walls of the two atria, and the *ventricular syncytium* that constitutes the walls of the two ventricles. This division allows the atria to contract a short time ahead of the ventricles, thus improving ventricular filling and heart pumping effectiveness.

Figure 1.1 shows the anatomy of the heart. Venous blood enters the right atrium of the heart through the superior and inferior *vena cava*. The right atrium has a relatively thin muscular wall and easily expands as blood fills it. Because of its high compliance, the right atrium pressure is normally very low (0-3 mmHg). Blood passes from the right atrium to the right ventricle through the tricuspid valve. The free wall of the right ventricle is thinner than the left ventricle, and anatomically it wraps itself around part of the larger and thicker left ventricle. The right ventricular wall, however, is thicker than the right atrium, so that when it contracts, it can develop considerably higher pressure (approximately 25 mmHg). As the right ventricle contracts, blood flows across an open semilunar pulmonary valve, and enters the pulmonary artery that conveys blood to the lungs where exchange of oxygen and carbon dioxide occurs. Oxygenated blood returns to the heart from the lungs through four pulmonary veins that enter the left atrium. This chamber is similar to the right atrium in that it is highly compliant, although the blood pressure in the left atrium is higher (6-10 mmHg). Blood flows from the left atrium across the mitral valve into the left ventricle. The left ventricular wall is very thick so that it can generate high pressures when it contracts (normally approximately 120 mmHg at rest). When the left ventricle contracts, blood is pumped through the semilunar aortic valve into the aorta, which then delivers blood to the arterial systemic circulation.

The tricuspid and mitral valves have fibrous strands (*chordae tendineae*) on their leaflets that attach to papillary muscles located on the respective ventricular walls. The papillary muscles contract during ventricular contraction and generate tension on the valve leaflets via the *chordae tendineae* to prevent the valves from bulging back into the atria reducing pumping effectiveness. The pulmonary and aortic semilunar valves do not have analogous attachments.

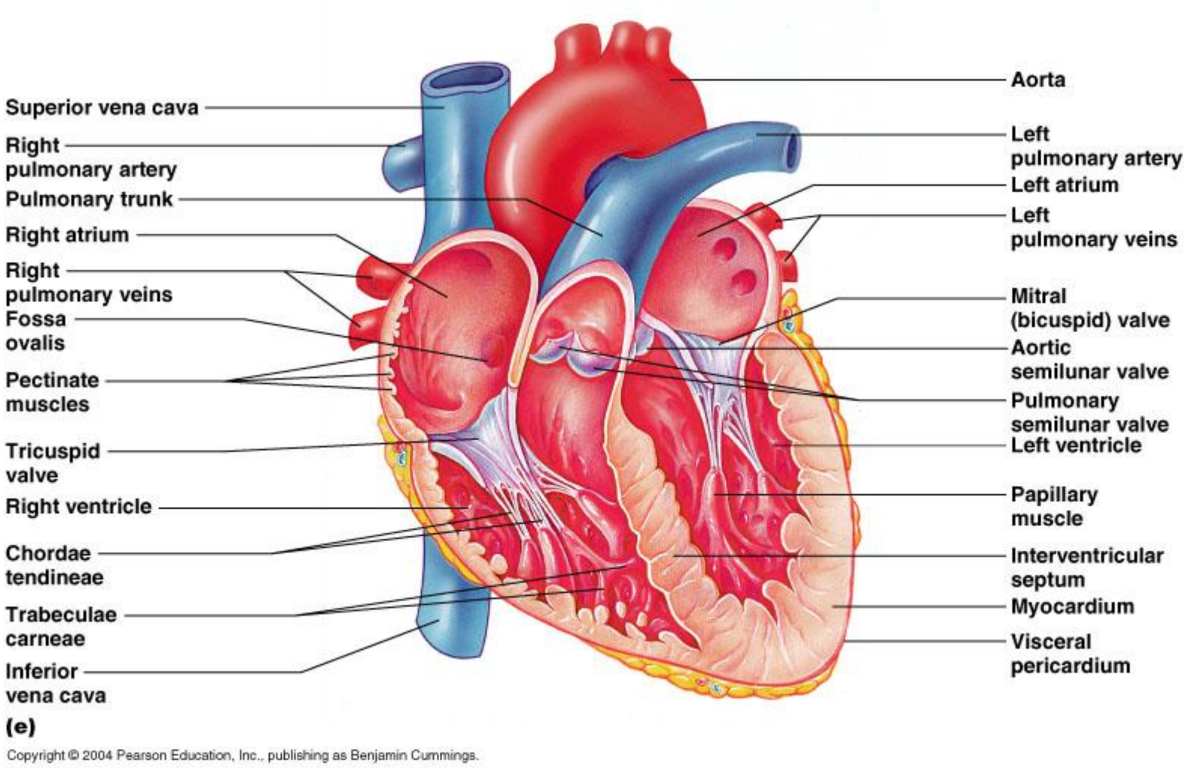

Figure 1.1 Anatomy of the heart. (From: www.biologycorner.com)

1.2 Electrical system of the heart

The specialized excitatory and conductive system of the heart that controls cardiac contractions is shown in Figure 1.2. The sinus node (also called *sinoatrial* or SA node) is a small strip of specialized muscle cells of few square millimeters, located in the superior posterolateral wall of the right atrium, lateral to the opening of the superior *vena cava*. The SA node is the site where the rhythmical impulse is generated. The sinus nodal fibers connect directly with the atrial muscle fibers, so that any action potential initiated in the sinus node spreads immediately into the atrial muscle wall. The conduction speed is approximately 0.3 m/s in most atrial muscle, although it increases to approximately 1 m/s in the anterior, middle and posterior *intermodal pathways* that are characterized by specialized conduction fibers.

The conductive system is organized so that the electrical impulse does not travel from the atria into the ventricles too rapidly. This delay of approximately 90 ms is operated by the *atrioventricular* (AV) node, located in the posterior wall of the right atrium adjacent to the opening of the coronary sinus. It allows the atria to empty the blood content into the ventricles before ventricular contraction begins.

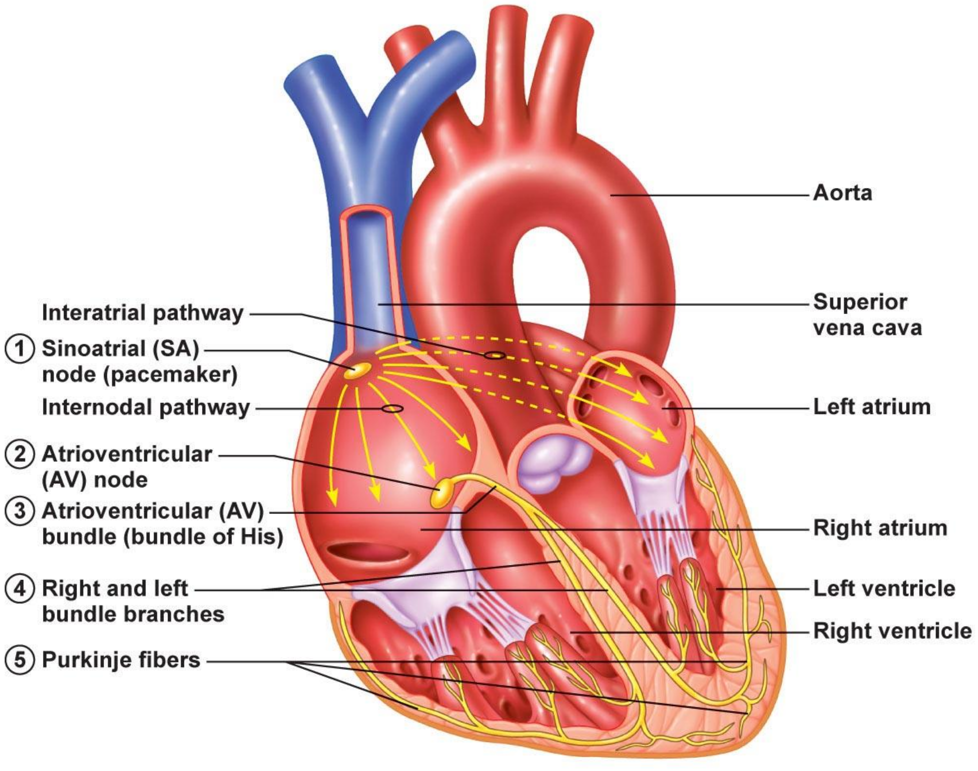

Figure 1.2 Electrical conduction system of the heart. (From: C.L. Stanfield, "Principles of human physiology" 2011)

The impulse then propagates to the *AV bundle*, encountering another delay of approximately 40 ms. The total delay (approximately 130 ms) adds up to the propagation time between SA and AV node, that is approximately 30 ms, before the impulse reaches the ventricles. The AV bundle merges into the left and right branches of the *Purkinje fibers* which conduct the electrical impulse to all parts of the ventricles. These are very large fibers, even larger than the ventricular muscle fibers, and transmit the impulse at 1.5 – 4.0 m/s, namely up to 6 times higher than in the ventricular muscle fibers. This allows almost immediate transmission of the impulse throughout the entire remainder of the ventricular muscle. The *Purkinje fibers* also have very few myofibrils, which means they only feebly contract during the course of impulse transmission.

A special characteristic of the *AV bundle* is the inability, in normal conditions, of action potentials to travel backwards in the bundle from the ventricles to the atria. This prevents re-entry of cardiac impulses, as the AV bundle is the only way the impulse can propagate from the atria to the ventricles, as the atrial muscle is separated from the ventricular muscle by a continuous fibrous barrier, which acts as insulator.

1.2.1 Action Potential

Pacemaker nodal cells

Cells within the *sinoatrial* (SA) node are the primary pacemaker of the heart. These cells generate regular, spontaneous action potentials in a cyclic self-sustained mechanism.

The action potential of the SA nodal cells may be divided into three phases, as shown in Figure 1.3. *Phase 4* is the spontaneous depolarization that triggers the action potential once the membrane reaches a threshold-voltage of approximately -40 mV. *Phase 0* is the depolarization phase of the action potential, followed by *phase 3* of repolarization. Once the cell is completely repolarized at about -60 mV, the cycle is spontaneously repeated. The changes in membrane potential are brought about by ions flow, principally Ca++ and potassium (K+), and to a lesser extent Na+, across the membrane through ion channels that open and close at different times during the action potential. When a channel is opened, there is increased electrical conductance. Conversely, closure of ion channels causes ion conductance to decrease. As ions flow through open channels, they generate electrical currents that change the membrane potential.

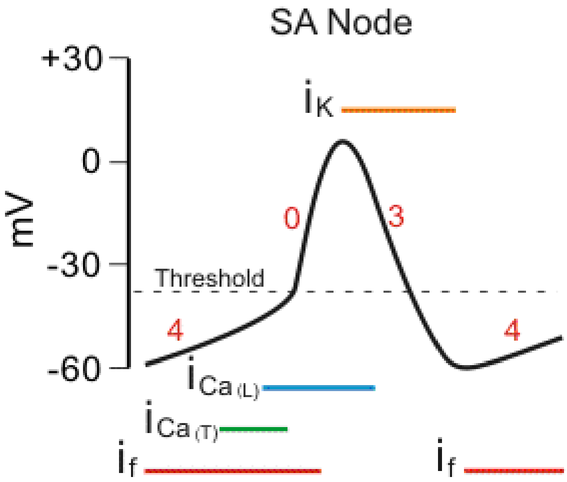

Figure 1.3 Action potential of the sinoatrial node cells of the heart. (From: “Cardiovascular physiology concepts”, www.cvphysiology.com)

At the end of repolarization, when the membrane potential is very low (about -60 mV), slow ion channels open allowing inward oriented (depolarizing) Na+ currents (I_f). As the membrane potential reaches about -50 mV, a T-type Ca++ channel opens. The inward directed Ca++ currents further depolarize the cell. As the membrane continues to depolarize to about -40 mV, a second Ca++ channel opens. These are the so-called long-lasting, or L-type Ca++ channels. Opening of these channels causes more Ca++ to enter the cell and to further depolarize the cell until an action potential threshold of approximately -40 mV is reached. *Phase 0* depolarization is primarily caused by increased Ca++ conductance through the L-type Ca++ channels that began to open toward the end of *phase 4*. Na+ and Ca++

currents through the T-type Ca++ channels decline during this phase as their respective channels close. Because the movement of Ca++ through these channels into the cell is not rapid, the rate of depolarization (slope of *phase 0*) is much slower than found in other cardiac cells (e.g. Purkinje cells). Repolarization occurs (*phase 3*) as K+ channels open, thereby increasing the outward oriented K+ current. At the same time, the L-type Ca++ channels become inactivated and close, which decreases calcium conductance and the inward depolarizing Ca++ currents.

The action potential pattern described for SA cells is similar to that of atrioventricular (AV) cells, determined primarily by changes in slow Ca++ and K+ currents.

Non-pacemaker cardiomyocites

Atrial myocytes, ventricular myocytes and Purkinje cells exhibit different behavior in action potential generation, with respect to the SA and AV cells (pacemaker cells). Unlike pacemaker nodal cells, non-pacemaker ones have a distinguishable resting membrane potential (*phase 4*) that remains near the equilibrium potential for K+, as shown in Figure 1.4.

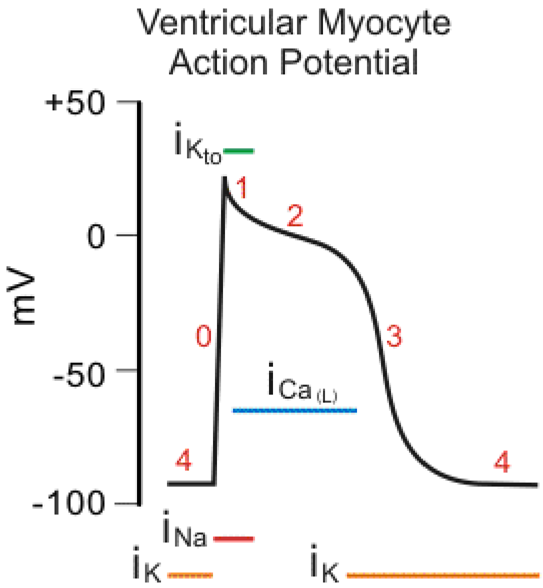

Figure 1.4 Non-pacemaker cardiomyocite action potential. (From: “Cardiovascular physiology concepts”, www.cvphysiology.com)

The resting membrane potential is very low (about -90 mV) due to K+ outward directed currents which increase electro-negativity of the cell. At this stage, fast Na+ channels and (L-type) slow Ca++ channels are closed. When these cells are rapidly depolarized to a threshold voltage of about -70 mV, there is a rapid depolarization (*phase 0*) that is caused by a transient increase in fast Na+ channel conductance. This rapidly increases the inward directed Na+ currents (I_{Na}). On the other hand, K+ conductance and currents fall as potassium channels close. *Phase 1* represents an initial repolarization that is caused by the opening of a special type of transient K+ channel (K_{to}), which causes a transient, hyperpolarizing outward oriented K+ current (I_{Kto}). However, because of the large increase in slow inward calcium current occurring at the same time and the transient nature of I_{Kto}, the repolarization is delayed and there is a plateau phase in the action potential (*phase 2*). This calcium inflow is governed by long-lasting (L-type) calcium channels that open when the membrane potential depolarizes to about -40 mV. This plateau phase differentiates cardiac cells from neural and skeletal muscular cells where the action potential is much shorter. Repolarization (*phase 3*) occurs when potassium conductance and I_K increase, along with the inactivation of Ca++ channels.

Once an action potential is initiated, there is a period of time comprising *phases 0, 1, 2,* and part of *phase 3* in which a new action potential may not be initiated. This phenomenon is known as absolute refractory period (ARP) of the cell. During this period, stimulation of the cell by an adjacent cell undergoing depolarization does not trigger a new action potential.

1.2.2 Rhythmic excitation of the SA node

The SA node is characterized by intrinsic automaticity, a spontaneous pacemaker activity occurring at a rate of 100-110 action potentials per minute, in normal conditions. However, the firing rate of the SA node is subject to intrinsic and extrinsic controls. Intrinsic control is mediated by the stretch-sensor nature of the pacemaker cells of the SA node. Increased venous return increases *preload* (right atrial pressure), which causes the right atrial wall to expand, stretching the SA cells. The SA cells respond by increasing their firing rate, which in turn increases the heart rate and consequently the cardiac output. This mechanism contrasts blood pooling in the atrial chamber.

On the other hand, the extrinsic mechanism is controlled by the autonomic nervous system. The SA node is innervated by sympathetic and parasympathetic fibers. The parasympathetic innervations, by the left and right branches of the *vagus* nerve, is predominant. The parasympathetic tone reduces the resting heart rate to 60-80 beats/min. Vagal activation, which releases *acetylcholine* (ACh) onto the SA node, decreases pacemaker rate by increasing the conductance of K+ channels and decreasing that of Ca++ and Na+ channels. These ionic conductance changes decrease the slope of phase 4 of the action potential shown in Figure 1.3, thereby increasing the time required to reach the threshold potential. Vagal activity also hyperpolarizes the pacemaker cell during Phase 4, which results in a longer time to reach the threshold potential.

Parasympathetic stimulation also decreases the excitability of the AV junctional fibers between atrial musculature and the AV node, thereby slowing transmission of the cardiac impulse into the ventricles.

On the other hand, sympathetic stimulation increases the rate of SA nodal discharge, the speed of conduction of the electrical impulse, as well as the excitability of all regions of the heart. In addition, sympathetic stimulation is also capable of increasing the strength of contraction of the heart muscle. To increase heart rate, the autonomic nervous system increases sympathetic outflow to the SA node, with concurrent inhibition of vagal tone. Inhibition of vagal tone is necessary for the sympathetic nerves to increase heart rate because vagal influences inhibit the action of sympathetic nerve activity. Sympathetic activation, which releases NE, increases pacemaker rate by decreasing K+ conductance and increasing that of Ca++ and Na+. These changes increase the slope of phase 4 (shown in Figure 1.3) so that the pacemaker potential more rapidly reaches the threshold for action potential generation.

The SA pacemaker activity is also altered by hormones. Circulating EP causes tachycardia by a mechanism similar to NE released by sympathetic nerves. Also, changes in the serum concentration of ions, particularly potassium, can cause changes in SA nodal firing rate. *Hyperkalemia* induces *bradycardia* or can even stop SA nodal firing. *Hypokalemia* increases the rate of phase 4 depolarization and causes tachycardia. Cellular hypoxia, usually due to ischemia, is another cause of alteration of SA discharge rate. With increasing severity it induces bradycardia which can degenerate into a complete stop of the SA pacemaker activity.

Various antiarrhythmic drugs also affect SA nodal rhythm. Calcium-channel blockers, for example, cause bradycardia by inhibiting the slow inward Ca++ currents during phase 4 and phase 0 (shown in Figure 1.3). Drugs affecting autonomic control or autonomic receptors (e.g., beta-blockers, *muscarinic* antagonists) directly or indirectly alter pacemaker activity. Digitalis causes bradycardia by increasing parasympathetic (vagal) activity on the SA node.

1.2.3 The electrocardiogram

The electrical currents generated by the depolarization and repolarization process of cardiac cells spread throughout the body. This electrical activity can be measured by an array of electrodes placed on the body surface. The recorded tracing is called electrocardiogram (ECG, or EKG). A typical normal ECG tracing is shown in Figure 1.5.

The different waves that comprise the ECG represent the sequence of depolarization and repolarization of the atria and ventricles. The ECG shown in the figure is recorded at a speed of 25 mm/sec, and the voltages are calibrated so that 1 mV = 10 mm in the vertical direction. Therefore, each small 1-mm square represents 40 ms in time and 0.1 mV in voltage. Because the recording speed is standardized, the heart rate may be calculated from the intervals between different waves.

The P wave represents the depolarization that spreads from the SA node throughout the atria, and is usually 80-100 ms in duration. The brief *isoelectric* period after the P wave represents the time in which the impulse travels through the AV node (where the conduction velocity is greatly reduced) and the bundle of His. Atrial rate can be calculated by determining the time interval between P waves. The period of time from the onset of the P wave to the beginning of the QRS complex is termed PR interval, which normally ranges from 120 ms to 200 ms in duration. This interval represents the time between the onset of atrial depolarization and the onset of ventricular depolarization.

The QRS complex represents ventricular depolarization. Ventricular rate can be calculated by determining the time interval between QRS complexes. The duration of the QRS complex is normally 60 to 100 ms. This relatively short duration indicates that ventricular depolarization normally occurs very rapidly. If the QRS complex is prolonged 100 ms, conduction is impaired within the ventricles. This can occur with bundle branch blocks or whenever a ventricular *focus* (abnormal or “ectopic” pacemaker site) takes over the role of pacemaker. Such an ectopic *focus* nearly always results in impulses being conducted over slower pathways within the heart, thereby increasing the time for depolarization and the duration of the QRS complex. The shape of the QRS changes depending on which recording electrodes are used. The shape will also change when there is abnormal conduction of electrical impulses within the ventricles.

The ST segment is the isoelectric period following the QRS complex. It is the time at which the entire ventricle is depolarized, roughly corresponding to the plateau phase of the ventricular action potential (Figure 1.4). The ST segment is important in the diagnosis of ventricular ischemia or hypoxia because under those conditions, the ST segment can become either depressed or elevated.

The T wave represents ventricular repolarization. It is longer in duration than depolarization since the repolarization wave propagates at lower speed than the depolarization wave). Sometimes a small wave may be seen following the T wave (not shown in Figure 1.5) with the same polarity. This wave represents the last remnants of ventricular repolarization.

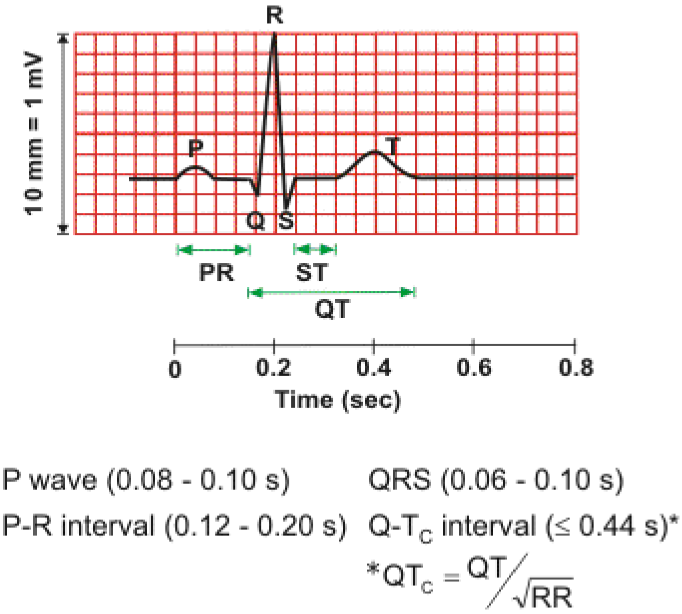

Figure 1.5 Typical electrocardiogram from normal sinus rhythm. (From: “Cardiovascular physiology concepts”, www.cvphysiology.com)

There is no distinctly visible wave representing atrial repolarization in the ECG because it occurs during ventricular depolarization. Because the wave of atrial repolarization is relatively small in amplitude, it is masked by the much larger ventricular-generated QRS complex.

ECG tracings recorded simultaneously from different electrodes placed on the body produce different characteristic waveforms.

1.2.3.1 ECG lead configurations

The ECG is recorded by means of electrodes placed on the body surface. In clinical practice, where the ECG is used for diagnostic purposes, a fundamental requirement is to define a universal protocol which standardizes the number of leads and their placement on the body. The twelve-leads ECG is the worldwide accepted standard for the purpose. It consists of ten electrodes: six precordial electrodes (V1,…, V6) and four limb electrodes. Correct precordial leads placement is illustrated in Figure 1.6, showing the anterior view on the frontal plane of the torso. The four limb leads, placed on the left wrist, right wrist, left leg and right leg, as shown in Figure 1.7, represent the original leads setting proposed by Dutch physiologist Willem Einthoven in the early 20th century.

The standard twelve-leads ECG protocol was defined for resting acquisitions, that is, for recording conditions in which the subject would lie supine, quietly and refraining from uttering, to minimize the presence of artifacts on the ECG recording. However, in ECG monitoring, sources of artifact such as electrode motion and skeletal muscle activity (EMG) are present and remarkable. Excessive artifacts have made it impractical to use the standard twelve-lead ECG with distal limb leads (standard-limb) when monitoring. The Mason-Likar modification of the standard twelve-lead ECG is commonly used for ECG monitoring. The Mason-Likar system uses all the conventional precordial electrode sites, but the limb electrodes are connected to sites on the anterior part of the torso instead of to distal limb sites. Repositioning the recording electrodes to only torso sites achieves the goal of reducing artifacts but requires the same number of electrodes (ten) as does the standard system. An alternative to the Mason-Likar system is to use only 3 to 5 electrodes (Welinder *et al.*, 2004).

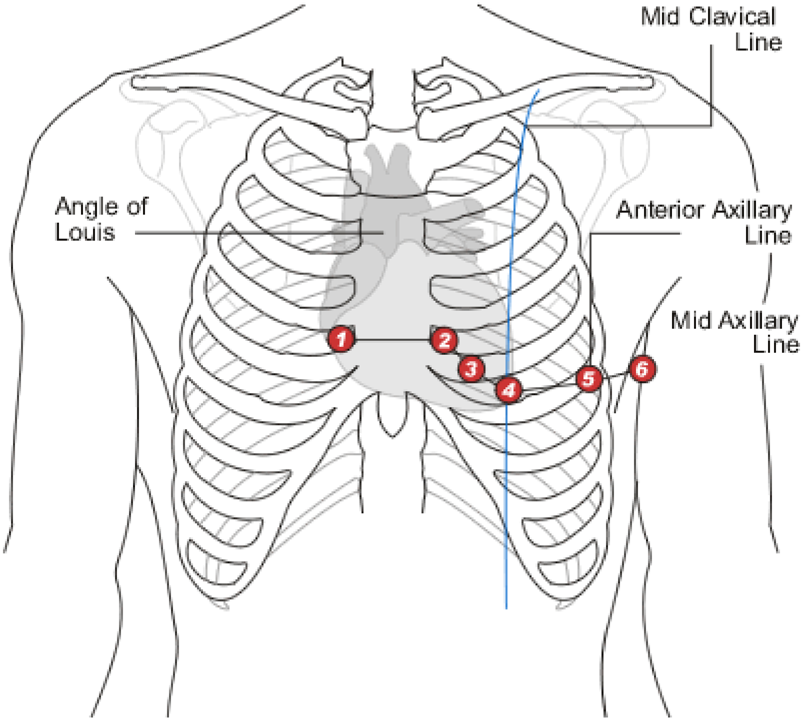

Figure 1.6 ECG electrodes placement: chest electrodes. (From: The University of Nottingham, Division of Nursing. www.nottingham.ac.uk)

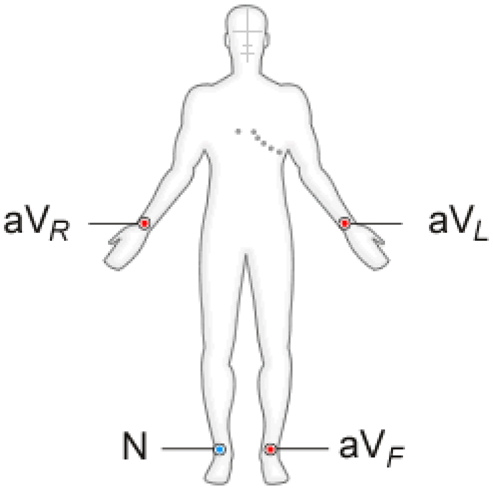

Figure 1.7 ECG electrodes placement: limb electrodes. (From: The University of Nottingham, Division of Nursing. www.nottingham.ac.uk)

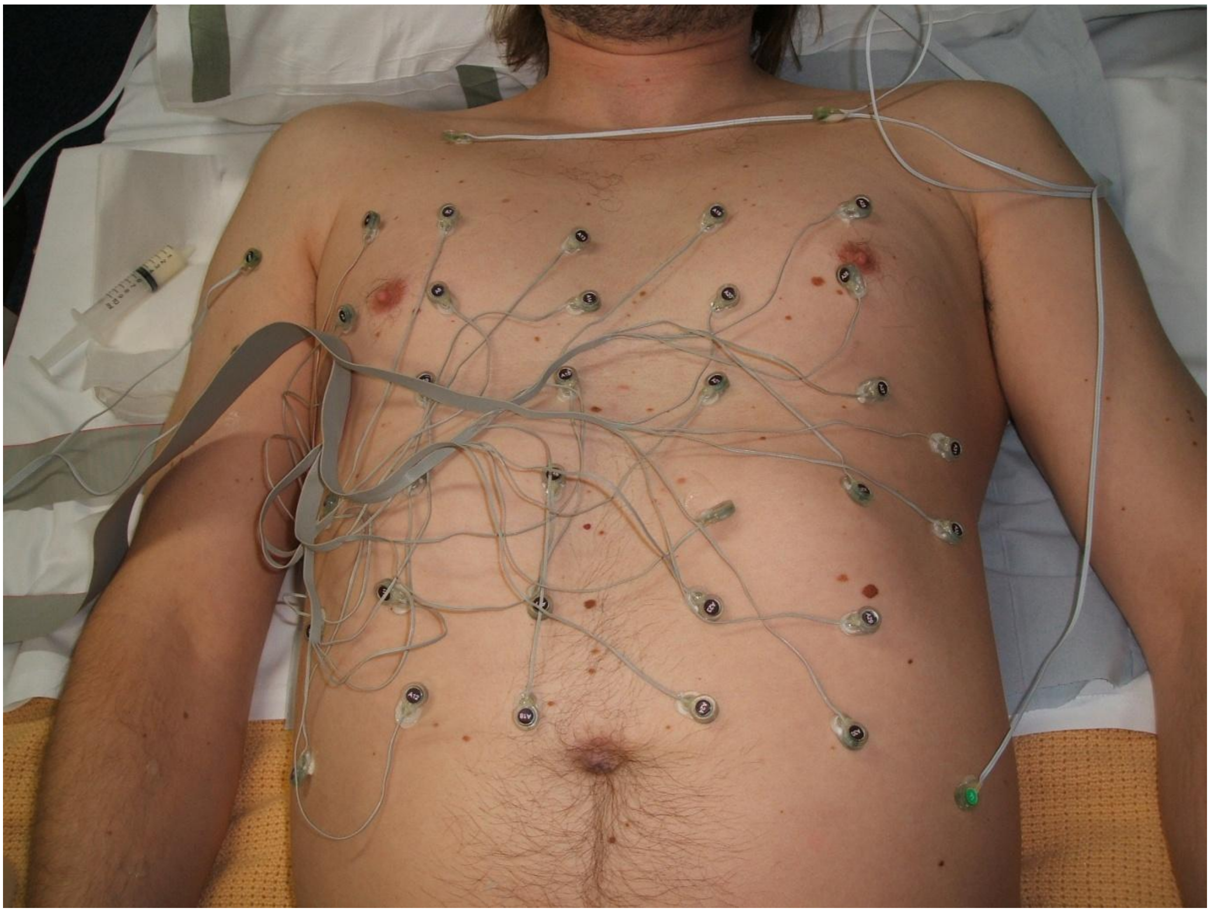

Figure 1.8 Body surface potential map. (Courtesy of Regional Medical Physics Department, Freeman Hospital, Newcastle upon Tyne, UK)

In general, the number of electrodes attached to the body surface depends on the type of clinical information desired. It is usually sufficient to use a few electrodes when only heart rhythm is being studied, whereas ten electrodes are typically used when information on waveform morphology is required. Much denser spatial sampling of the body surface can be achieved by employing a recording technique known as "body surface potential mapping" (BSPM), in which an array of tens to hundreds of electrodes is attached to the torso (Figure 1.8). The signals recorded with such an electrode array can be used to produce a sequence of "electrical images" which offer a more detailed view of the spatiotemporal potential distribution over the body surface, with respect to the twelve-leads ECG. For example, an electrical image may capture the presence of local large gradients in potential which would be missed when too sparse spatial sampling is used (Sörnmo and Laguna, 2005).

1.3 The autonomic nervous system

The *autonomic nervous system* (ANS) controls most visceral functions of the body. It contributes to the control of arterial pressure, gastrointestinal motility and secretion, urinary bladder emptying, sweating and body temperature.

One characteristic of the ANS is the rapidity and intensity with which it can change visceral functions: it can increase the heart rate twofold in 3 to 5 seconds, and it can double the arterial pressure in 10 to 15 seconds.

The ANS is activated mainly by centers located in the spinal cord, brain stem and hypothalamus (Figure 1.9). Also, portions of the cerebral cortex, especially of the limbic cortex, can transmit impulses to the lower centers and influence ANS control.

The ANS also operates by means of visceral reflexes. That is, subconscious sensory signals from a visceral organ can enter the autonomic ganglia, the brainstem, or hypothalamus and return subconscious reflex responses directly back to the visceral organ to control its activities. The efferent autonomic signals are transmitted to the various organs of the body through two major subdivisions: the sympathetic and the parasympathetic nervous system. Figure 1.9 shows the general organization of the ANS. The sympathetic nerve fibers originate in the spinal cord, between segments T1 and L2, and pass first into the sympathetic chain and then to the target tissue and organs. The sympathetic pathway from the spinal cord to any target tissue or organ is composed of two neurons: a preganglionic neuron and a postganglionic neuron. Immediately after the spinal nerve leaves the spinal canal, the preganglionic sympathetic fibers leave the nerve and pass through a white *ramus* into one of the ganglia of the sympathetic chain. Then the course of the fibers can either synapse with postganglionic neurons in the ganglion that it enters, or progress in the chain and synapse in one of the other ganglia in the chain, or it can pass through the chain and through one of the sympathetic nerves radiating outward, finally synapsing in a peripheral sympathetic ganglion. The postganglionic neuron thus originates either in one of the sympathetic chain ganglia or in one of the peripheral sympathetic ganglia.

The general organization of the parasympathetic nervous system is shown in Figure 1.9. Parasympathetic fibers leave the central nervous system through cranial nerves III, VII, IX and X, and additional parasympathetic leave the lowermost part of the spinal cord through the second and third sacral spinal nerves and occasionally through the first and fourth sacral nerves. About 75% of all parasympathetic fibers are in the *vagus* nerves (cranial nerve X), passing to the entire thoracic and abdominal regions of the body. The *vagus* nerves, also referred to as *vagi*, supply parasympathetic nerves to the heart, lungs, esophagus, stomach, entire small intestine, proximal half of the colon, liver, gallbladder, pancreas and upper portions of the ureters. Parasympathetic fibers in the third cranial nerve innervate the papillary sphincters and ciliary muscles of the eye. Fibers from the seventh cranial nerve pass to the lacrimal, nasal, and submandibular glands. And fibers of the ninth cranial nerve innervate the parotid gland. The sacral parasympathetic fibers distribute to the descending colon, rectum, urinary bladder, lower portions of the ureters, and external genitalia. The parasympathetic system, like the sympathetic, has both preganglionic and postganglionic neurons. However, in general, parasympathetic preganglionic fibers pass uninterrupted all the way to the target organ. In the wall of the organ are located the postganglionic neurons. The preganglionic fibers synapse with these, and very short postganglionic fibers leave the neurons to innervate the tissues of the organ.

The sympathetic and parasympathetic fibers secrete mainly one of two synaptic transmitter substances: ACh and *norepinephrine* (NE). Fibers of the first type are called cholinergic, fibers of the second type adrenergic. All preganglionic neurons are cholinergic, in both the sympathetic and parasympathetic systems. On the other hand, most of the postganglionic neurons of the sympathetic system are adrenergic, while most of the parasympathetic postganglionic neurons are cholinergic.

ACh activates mainly two types of receptors called *muscarinic* and *nicotinic*. Muscarinic receptors are located on all effectors cells stimulated by the postganglionic neurons of the parasympathetic nervous system as well as on those stimulated by the postganglionic cholinergic neurons of the sympathetic system. Nicotinic receptors are located at the synapses between the preganglionic and postganglionic neurons of both the sympathetic and parasympathetic systems.

There are also two types of adrenergic receptors: *alpha* receptors and *beta* receptors. The *beta* receptors are in turn divided into *beta-1* and *beta-2*, and alpha receptors into *alpha-1* and *alpha-2*, although the *alpha* receptors subdivision is less distinct. NE and *epinephrine* (EP) are secreted into the blood by the adrenal medulla. NE excites *alpha* receptors to a greater extent than *beta* receptors. Conversely, EP excites both types approximately equally.

Certain *alpha* functions are excitatory while others are inhibitory, as for *beta* functions. As a consequence, the sympathetic system cause excitatory effects in some organs and inhibitory effects in others. This behavior is also observed in the parasympathetic system.

When the sympathetic stimulation excites a particular organ, parasympathetic stimulation sometimes inhibits it, demonstrating that the two systems occasionally act reciprocally to each other. But most organs are dominantly controlled by one of the two systems.

Sympathetic stimulation of the heart generally increases the overall activity of the myocardium. This is accomplished by increasing both the rate (positive *chronotropy*) and the force of contraction (positive *inotropy*). Parasympathetic stimulation causes mainly the opposite effects. However, parasympathetic innervation of the heart is mainly concentrated in the SA and AV nodes, whereas the sympathetic is distributed across the cardiac muscle.

Most systemic blood vessels, especially those in the abdominal viscera and the skin of the limbs, are constricted by sympathetic stimulation. Parasympathetic stimulation has almost no effect on most blood vessels.

The arterial blood pressure is determined by two factors: propulsion of blood by the heart and resistance to flow through the vessels. Sympathetic stimulation increases both propulsion and resistance, which generally causes a marked acute increase in arterial pressure but very often very little change in long term pressure unless the sympathetic system stimulates the kidneys to retain salt and water at the same time. Conversely, moderate parasympathetic stimulation decreases the pumping by the heart but has virtually no effect on peripheral resistance. The usual effect is a slight decrease in blood pressure, although very strong stimulation can cause a transient drop of blood pressure.

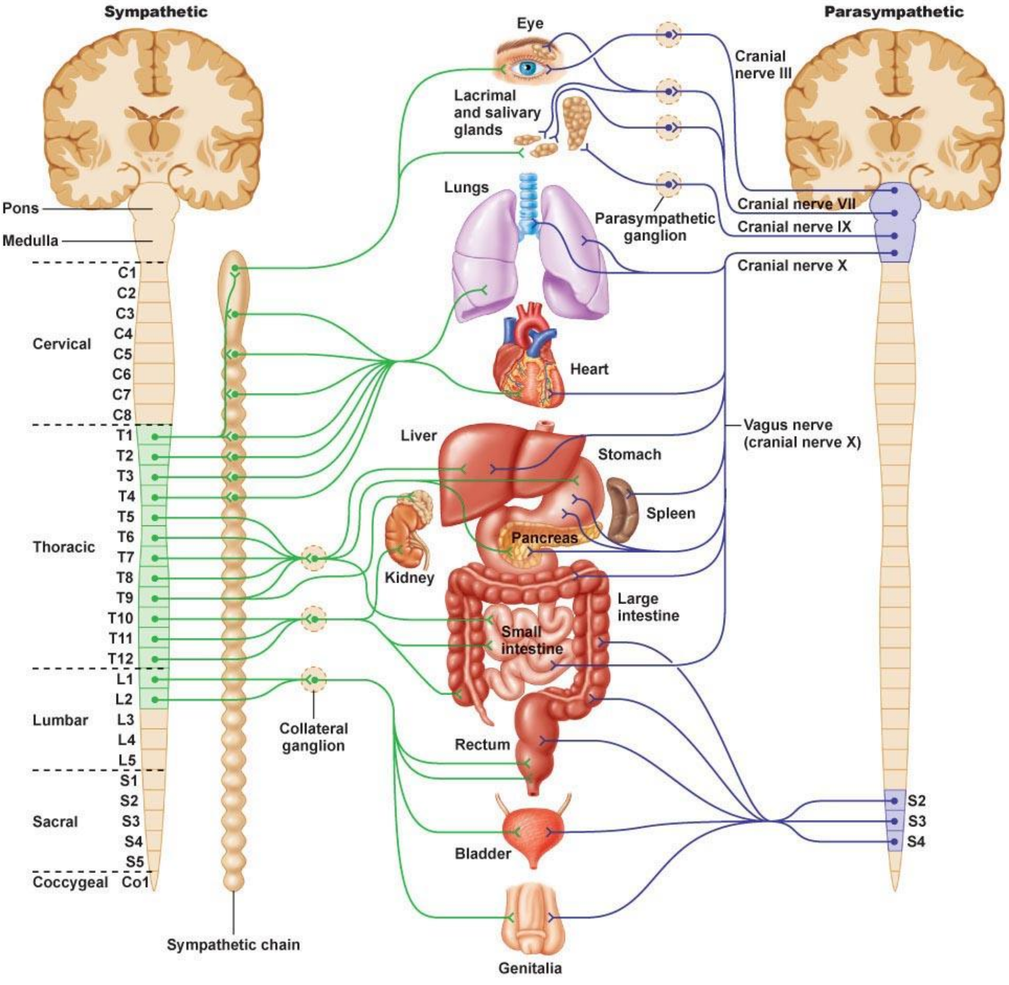

© 2011 Pearson Education, Inc.

Figure 1.9 The autonomic nervous system. ANS = autonomic nervous system; ALS = anterolateral system; NTS = nucleus tractus solitarius (From: Stanfield CL, “Principles of human physiology” 2011)

Stimulation of the sympathetic nerves to the adrenal medullae causes large quantities of EP and NE to be released into the circulating blood. The two hormones have almost the same effects on the different organs as those caused by direct sympathetic stimulation, except that the effects last 5 to 10 times longer, due to the slow removal process of these hormones which requires 1 to 3 minutes. The effects of circulating NE include constriction of nearly all the blood vessels of the body, inhibition of the gastrointestinal tract, pupil dilation and increased activity of the heart. As a result of circulating NE, the total peripheral resistance is strongly increased together with the arterial blood pressure. EP causes almost the same effects except it has greater effect in stimulating *beta* receptors and cardiac activity, while causing only weak constriction of blood vessels in the muscles.

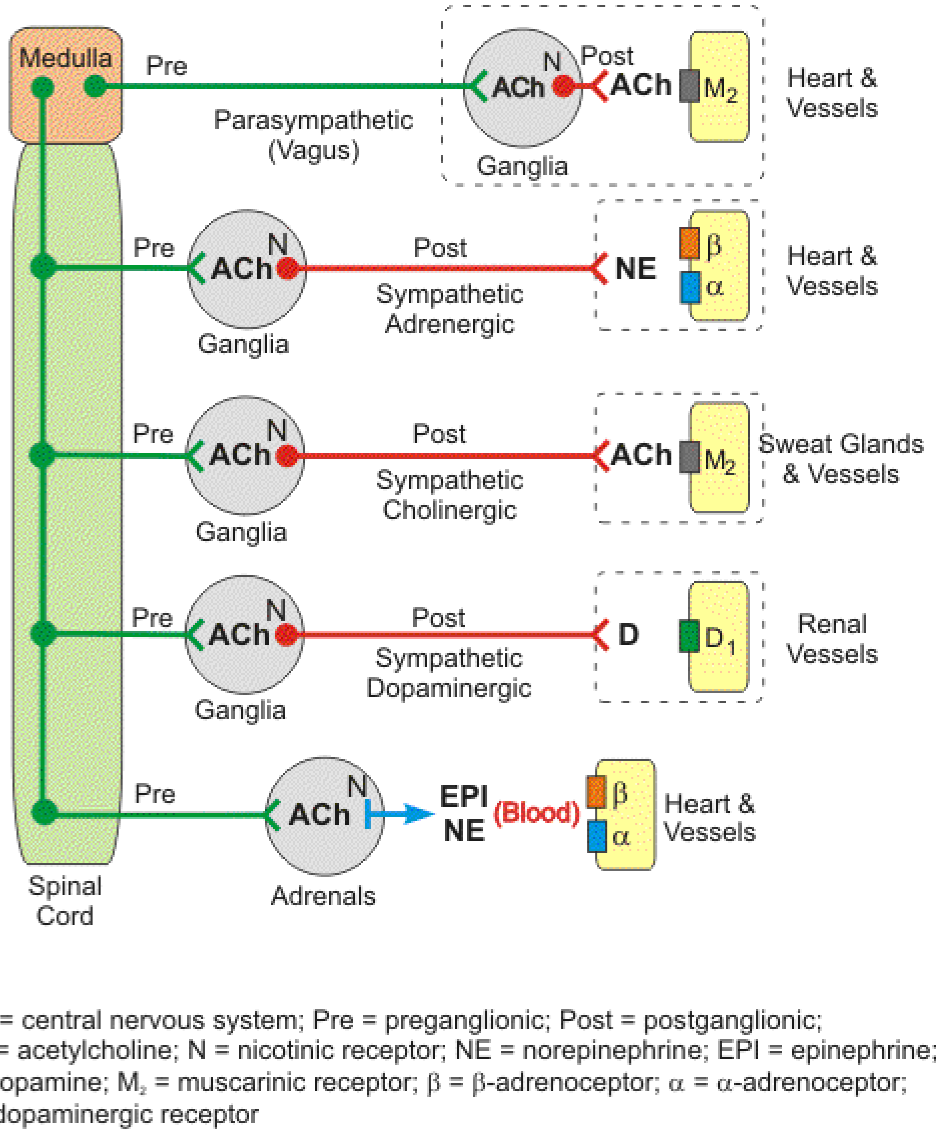

CNS = central nervous system; Pre = preganglionic; Post = postganglionic;
ACh = acetylcholine; N = nicotinic receptor; NE = norepinephrine; EPI = epinephrine;
D = dopamine; M_2 = muscarinic receptor; β = β-adrenoceptor; α = α-adrenoceptor;
D_1 = dopaminergic receptor

Figure 1.10 General organization of the autonomic nervous system. (From: Klabunde RE, "Cardiovascular Pharmacology concepts", www.cvpharmacology.com)

Normally, the sympathetic and parasympathetic systems are continually active, and the basal rates of activity are known as sympathetic tone and parasympathetic tone, respectively. Figure 1.10 shows the general structure of pre- and post-ganglionic neurons of the sympathetic and parasympathetic efferent pathways of the ANS.

1.3.1 The baroreceptor reflex

Arterial blood pressure is normally regulated within a narrow range, with a mean value typically ranging from 85 to 100 mmHg in adults. Arterial pressure *homeostasis* is crucial to ensure adequate blood flow to organs throughout the body. This is accomplished by negative feedback systems incorporating pressure sensors (baroreceptors) that sense the arterial pressure. The most important arterial baroreceptors are located in the carotid sinus, at the bifurcation of external and internal carotids, and in the aortic arch (Figure 1.11). These receptors respond to stretching of the arterial wall so that if arterial pressure suddenly rises, the walls of these vessels passively expand, causing the receptors to increase their firing rate. Conversely, if arterial blood pressure falls, decreased stretch of the arterial wall leads to a decreased firing rate of the receptors. The carotid sinus baroreceptors are innervated by the sinus nerve of Hering, a branch of the glossopharyngeal nerve (IX cranial nerve). The glossopharyngeal nerve synapses in the *nucleus tractus solitarius* (NTS) located in the medulla of the brainstem.

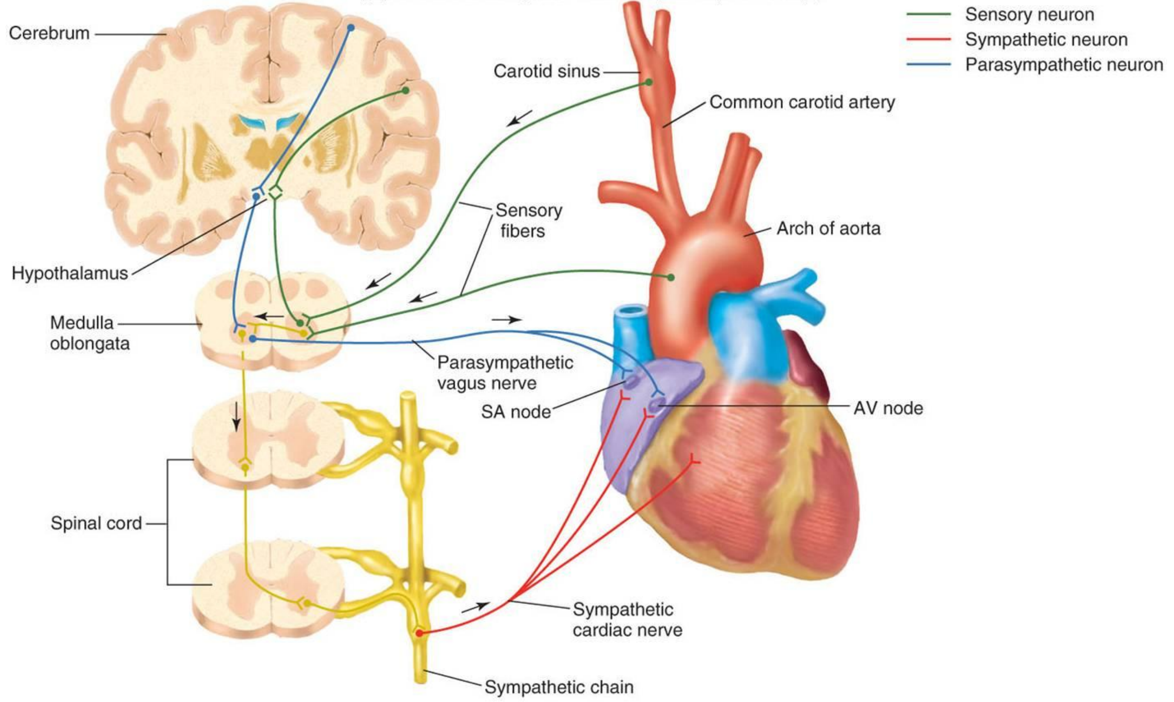

Figure 1.11 Role of the autonomic nervous system in the baroreceptor reflex. (From: http://phgy210.wikispaces.com, Copyright © The McGraw-Hill Companies, Inc.)

The aortic arch baroreceptors are innervated by the aortic nerve, which then combines with the *vagus* nerve (X cranial nerve) traveling to the NTS. The NTS modulates the activity of sympathetic and parasympathetic (vagal) neurons in the medulla, which in turn regulate the autonomic control of the heart and blood vessels.

Of these two arterial baroreceptors sites, the carotid sinus is quantitatively the most important for regulating arterial pressure. The carotid sinus receptors respond to pressures ranging from 60-180 mmHg (Figure 1.11). Receptors within the aortic arch have a higher threshold pressure and are less sensitive than the carotid sinus receptors. Baroreceptors are also sensitive to the mean pressure value. That is, at a given mean arterial pressure, decreasing the pulse pressure (systolic minus diastolic pressure) decreases the baroreceptor firing rate.

Maximal carotid sinus sensitivity occurs near the normal mean arterial pressure so that even small changes in arterial pressure around the "set point" dramatically alter receptor firing rate in a feedback mechanism which attempts to restore the set point. A decrease in arterial pressure (mean, pulse or both) results in decreased baroreceptor firing. The "cardiovascular center" within the medulla responds by increasing the sympathetic outflow and decreasing the parasympathetic (vagal) outflow. Under normal physiological conditions, baroreceptor firing exerts a tonic inhibitory influence on the sympathetic outflow from the medulla. Therefore, acute hypotension results in a dramatic reduction of sympathetic inhibition within the medulla, so that sympathetic tone increases. These autonomic changes cause vasoconstriction (increased peripheral vascular resistance), tachycardia and increase in the force of cardiac contraction. The latter two changes increase the cardiac output, while the increases in cardiac output and peripheral resistance contribute to the restoration of the systemic arterial pressure.

Baroreceptors, however, adapt to chronic changes in arterial pressure. For example, if arterial pressure suddenly falls when a person stands, the baroreceptor firing rate will decrease; however, after a period of time, the firing returns to near normal levels as the receptors adapt to the lower pressure. Therefore, the long-term regulation of arterial pressure requires activation of other mechanisms (primarily hormonal and renal) to maintain normal arterial blood pressure (Klabunde, 2011).

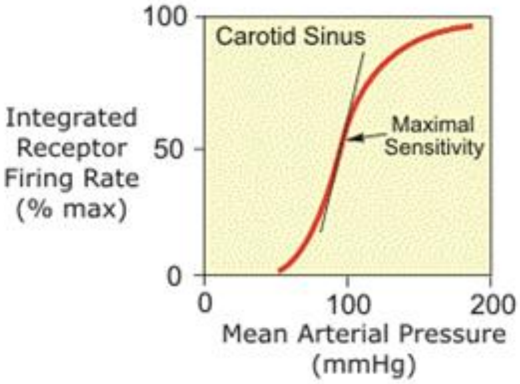

Figure 1.12 Carotid sinus fibers firing rate as a function of mean arterial blood pressure. (From: R.E. Klabunde, “Cardiovascular Physiology Concepts”. www.cvphysiology.com)

1.3.2 The Bainbridge reflex

The Bainbridge reflex describes an increase in heart rate due to an increase in right atrial or central venous pressure via stretch receptors (mechanoreceptors) located in the right atrial wall and junctions of the *venae cavae*.

When the right atrial pressure increases, the heart rate also increases in an attempt to maintain homeostasis of blood filling of the cardiac chambers. A small part of this increase is caused by a direct effect of the increased atrial volume which causes the atrial wall to stretch, which in turn causes the pacemaker cells of the SA node to increase their firing rate. Direct stretch can increase the heart rate as much as 15%.`An additional 40-60% increase is caused by a nervous reflex known as Bainbridge reflex, named after British physician Francis Arthur Bainbridge who first described it in 1914. Mechanoreceptors are stimulated by the increase in atrial pressure caused by increased venous return. They elicit the Bainbridge reflex by transmitting afferent signals through the vagus nerves to the medulla of the brain. A parasympathetic inhibitory response is generated which increases sympathetic outflow causing the heart rate and contractility to increase. Thus, the Bainbridge reflex helps prevent blood pooling in the atria. The changes in the heart rate, however, are dependent on the underlying rate prior to stimulation; thus, relatively fast heart rates are less sensitive to further increases (Guyton and Hall, 2001; Modak, 2008).

The Bainbridge reflex and the baroreceptor reflex act in a reciprocal way: the increase in heart rate caused by the Bainbridge reflex is followed by an increase in arterial pressure, which stimulates the baroreceptors of the carotid sinus and aortic arch, which in turn trigger the baroreflex mechanism to decrease heart rate.

1.3.3 The respiratory sinus arrhythmia

The respiration-related modulation of heart rate, characterized by tachycardia during inspiration and bradycardia during expiration, is known as *respiratory sinus arrhythmia* (RSA).

During inspiration, the thoracic pressure decreases causing an increase of venous return due to hydrostatic gradient. Increased atrial filling causes the atrial wall to stretch, triggering the Bainbridge reflex. As a result the heart rate increases. However, increased cardiac filling also elicits an increase in the stroke volume (Frank-Starling mechanism) and blood pressure. This activates the baroreflex that opposes the increase in heart rate (*tachycardia*) caused by the Bainbridge reflex. Thus, the baroreceptor reflex limits the respiratory sinus arrhythmia.

During expiration the opposite phenomenon occurs: the venous return is decreased and the decreased right atrial pressure inhibits the Bainbridge reflex, the force of cardiac contraction and stroke volume are reduced due to reduced filling, and the baroreflex mechanism causes the heart rate to be reduced (*bradycardia*).

The intensity (amplitude) of respiratory sinus arrhythmia can be seen as the balance of the Bainbridge reflex and the baroreceptor reflex (Stauss, *Physionet.org*).

References

Guyton AC, Hall JE. Textbook of medical physiology. Saunders 10th Edition 2001. p. 191

Klabunde RE. Cardiovascular Physiology Concepts. *Lippincott Williams & Wilkins 2nd Edition* 2011. [www.cvphysiology.com]

Klabunde RE. Cardiovascular Pharmacology Concepts. [www.cvphysiology.com]

Modak RK, Anesthesiology keywords review. *Lippincott Williams & Wilkins* 2008. pp. 197–198.

Sörnmo L, Laguna P. Bioelectrical signal processing in cardiac and neurological applications. *Elsevier Academic Press* 2005. pp. 411–12

Stauss HM. Physiologic Mechanisms of Heart Rate Variability (HRV) Parts 1 & 2. *www.physionet.org* [online]

Welinder A, Sörnmo L, Feild DQ, Feldman CL, Pettersson J, Wagner GS, Pahlm O. Comparison of signal quality between EASI and Mason-Likar 12-Lead Electrocardiograms during physical activity. *Am J Crit Care* 2004; 13(3):228–234.

Chapter 2: Heart rate variability

2.1 Heart rate variability background

During normal sinus rhythm, the heart rate varies from beat to beat. Heart rate variability (HRV) results from the dynamic interplay between the multiple physiologic mechanisms that regulate the instantaneous heart rate (IHR), or conversely, the instantaneous inter-beat interval (IBI). Short-term IHR oscillations reflect changes in the relative balance between the sympathetic and parasympathetic branches of the ANS, known as the sympathovagal balance.

Measurement of HRV first requires detection of each heart beat. For the purpose of assessing autonomic regulatory effects on HR, the most accurate time marker (*fiducial point*) is the onset of atrial depolarization, namely the P wave onset. Unfortunately, the amplitude of the P wave is generally low, which makes it often difficult to detect, especially in noisy signals. Conversely, the R wave is easy to detect and label with a fiducial point. The exact location of this marker is usually defined to be either the highest (or lowest) point, the QRS onset, or the QRS center of mass. Furthermore, the competing effects of the ANS branches lead to subtle changes in the features within the heartbeat (Clifford *et al.* 2006). For instance, an increased sympathetic stimulation of the SA node (during physical exercise, for example) will lead to an increased local heart rate, and an associated shortening of the PR interval, QT interval, QRS width, and T wave. Since the magnitude of the beat-to-beat modulation of the PR interval is correlated with, and much less significant than that of the RR interval (due to modulation of AV nodal conduction), and the R peak is well defined and easy to locate, the RR-interval (of normal sinus rhythm beats) is generally preferred. However, the sensitivity of the spectral HRV metrics to sampling frequencies below 1 KHz indicates that even small differences may have a significant effect for such metrics under certain circumstances (Clifford *et al.* 2006).

An RR-interval series (*tachogram*) recorded over a time window of at least 5 minutes is typically characterized by a power spectral density distribution exhibiting two dominant peaks: one in the low frequency (LF) range (0.04–0.15 Hz) and one in the high frequency (HF) region (0.15–0.4 Hz). In general, the activity in the HF band is thought to reflect parasympathetic activity at the SA node. Since respiration is a parasympathetically mediated activity (through the vagal nerve), a peak corresponding to the rate of respiration can often be observed in this frequency band, caused by RSA. However, not all the parasympathetic activity is due to respiration. Furthermore, the respiratory rate may drop below the (generally accepted) lower bound of the HF region and therefore confound measures in the LF region. The LF region is generally thought to reflect sympathetically mediated activity, mainly related to blood pressure homeostasis, through the baroreceptors reflex. Activity in bands lower than the LF region are less well understood but seem to be related to thermoregulation, neurohormonal regulation, and circadian variations such as postural and behavioral changes.

Many metrics for evaluating HRV have been described in the literature, together with their varying successes for discerning particular clinical problems. In general, HRV metrics can be broken down into either statistical time-based metrics or frequency-based metrics that evaluate power, or ratios of power, in certain spectral bands. Furthermore, most metrics are calculated either on a short time scale (often about 5 minutes) or over very long periods of time (usually 24 hours).

2.2 Clinical relevance of HRV

There is growing evidence for the role of the ANS in a wide range of somatic and mental diseases. The two major branches of the ANS, namely the sympathetic system, associated with energy mobilization, and the parasympathetic system, associated with vegetative and restorative functions, are in dynamic balance. When this changes into a static imbalance, for example, under environmental pressures, the organism becomes vulnerable to pathology.

Modern conceptions of organism function based on complexity theory hold that organism stability, adaptability, and health are maintained through variability in the dynamic relationship among system elements (Thayer and Sternberg, 2006). Patterns of organized variability are preserved to cope with constantly changing environmental demands. Consequentially, optimal system functioning requires flexible regulation of local energy expenditure. In contrast, rigid regularity is associated with mortality, morbidity, and ill health. A corollary of this view is that autonomic imbalance, in which one branch of the ANS dominates over the other, is associated with a lack of dynamic flexibility and health. Empirically, there is a large body of evidence to suggest that autonomic imbalance, in which typically the sympathetic system is hyperactive and the parasympathetic system is hypoactive, is associated with various pathological conditions (Brook and Julius, 2000). In particular, when the sympathetic branch dominates for long periods of time, the energy demands on the system become excessive and ultimately cannot be met.

When both cardiac vagal (the primary parasympathetic nerve) and sympathetic inputs are blocked pharmacologically (for example, with *atropine* plus *propranolol*, the so-called double blockade), intrinsic HR is higher than the normal value at rest. This fact supports the idea that the heart is under tonic inhibitory control by parasympathetic influences. Thus, resting cardiac autonomic balance favors energy conservation by means of parasympathetic dominance over sympathetic influences. In addition, the HR time series is characterized by considerable beat-to-beat variability (HRV), which also implicates vagal dominance, as the sympathetic influence on the heart is too slow to produce rapid beat-to-beat changes. Low HRV is associated with increased risk of all-cause mortality, and has been proposed as a marker for disease.

Several structural and functional alterations of the cardiovascular system that are frequently found in hypertensive individuals may increase their cardiovascular risk beyond that induced by the blood pressure (BP) elevation alone. Electrocardiographic evidence of left ventricular hypertrophy (LVH) and strain are associated with increased morbidity and mortality. HRV is significantly reduced in patients with LVH secondary to hypertension or aortic valve disease (Acharya *et al.*, 2006), in particular a reduction in baroreflex sensitivity is observed in cardiac LVH.

In one of the first studies (Kleiger *et al.*, 1987) to investigate the relationship between indices of HRV and mortality, it was shown in almost 900 post-myocardial infarction (MI) patients that HRV was a significant independent predictor of mortality in this high risk group. Numerous studies (Acharya *et al.*, 2006; Carney *et al.*, 2004; Carney *et al.*, 2005) have since supported the notion that decreased vagal activity, as indexed by HRV, predicts mortality in high risk as well as low risk populations.

Low HRV has also been shown to be associated with diabetes mellitus, and decreased HRV has been shown to precede evidence of disease provided by standard clinical tests (Pfeifer *et al.*, 1982; Singh *et al.*, 2000; Villareal *et al.*, 2002; Thayer and Sternberg, 2006).

Autonomic function tests conducted on patients with chronic renal failure, reveal a predominant impairment of the parasympathetic nervous system (Zoccali *et al.*, 1982), while spectral analysis exhibits a strong reduction in the HR power spectrum at all frequency ranges (Axelrod *et al.*, 1987).

Studies have shown that smokers have increased sympathetic and reduced vagal activity as measured by HRV analysis (Acharya *et al.*, 2006). HRV also appears to decrease with the acute ingestion of alcohol, suggesting parasympathetic withdrawal. (Malpas *et al.*, 1991) have demonstrated vagal neuropathy in men with chronic alcohol dependence using 24 h HRV analysis.

Recent work has suggested that HRV can be used to measure physiological changes in a number of psychiatric illnesses such as major depression, generalized anxiety disorder, schizophrenia, panic disorder (PD), and posttraumatic stress disorder (PTSD). Exposure to extreme traumatic events may lead to persistent behavioral and physiological abnormalities, which are recognized as the clinical syndrome of post-traumatic stress disorder (PTSD), characterized by vivid intrusive re-experiencing of the traumatic event ‘flashbacks’, and extreme anxiety and avoidance upon exposure to stimuli resembling the event. This syndrome is accompanied by changes under two distinct conditions: a basal condition of partial hyper-arousal, associated with increased heart rate and blood pressure, and a state of further stimulation on exposure to stress-related cues (Cohen *et al.*, 2000).

Panic disorder (PD), a syndrome characterized by spontaneous panic attacks involving intense anxiety and fear of losing control, together with autonomic symptoms such as palpitations, hyperventilation, tremor and dizziness, has also been studied by means of HRV. Evidence has been found of sympathetic dysregulation in PD, characterized by significantly increased LF and marginally increased HR (Friedman and Thayer, 1998).

2.3 HRV in psychophysiological research

HRV has been used to assess interventions that might impact sympathetic–parasympathetic balance in conditions not associated with cardiac disease or autonomic neuropathy (Fu *et al.*, 2006; Paul-Labrador *et al.*, 2006). Numerous studies have reported evidence that HRV is sensitive to changes in mental effort (Mulder and Mulder, 1981; Aasman *et al.*, 1987; Jorna, 1992; Veltman and Gaillard, 1993). With an increase in mental effort, there is a decrease in power around 0.10 Hz, in what some authors referred to as the mid-frequency band, 0.07–0.14 Hz (Jorna, 1992). This is now commonly known as the low frequency band, 0.04–0.15 Hz (Task Force of the European Society of Cardiology, 1996). The underlying mechanism may be due to increased sympathetic activation or the subjects' pattern of breathing (Althaus *et al.*, 1998). In other studies, apart from a strong inverse relationship between mental effort and HRV power, mean RR interval appears to be the most sensitive measure (Capa *et al.*, 2008; De Rivecourt *et al.*, 2008; Henelius *et al.*, 2009; Weippert *et al.*, 2009). While HRV has useful applications both clinically and as an autonomic measure in physiological research, the inter-subject variability of HRV measures is rather high (Gerritsen *et al.*, 2003; Pinna *et al.*, 2007). Thus, it is difficult to generalize the results from any one given study to others with subjects of different demographic characteristics. Additionally, the within-subject reliability of HRV measures remains unclear (Mukherjee *et al.*, 2011). The degree of reproducibility of HRV measurements from short-term recordings in healthy people is inconsistent and can at best be considered moderate (Pinna *et al.*, 2007; Sandercock *et al.*, 2005), except under highly controlled resting conditions (Melanson, 2000). Studies of reliability of HRV parameters during mental effort tasks is lacking in the literature.

2.4 Measures of HRV

2.4.1 Time domain measures of HRV

For the purpose of assessing autonomic regulatory effects on HR, the most appropriate approach would ideally detect the occurrence of sinus nodal events or P waves. In practice, this is technically difficult in surface ECG, so HRV measurement is usually based on the sequence of RR intervals. This practice neglects the potential presence of fluctuations in PR interval due to modulation of AV nodal conduction. Premature ventricular contractions (PVC) and premature atrial contractions (PAC) represent additional confounders in assessing autonomic regulation of HR. Removal of the effects of PVCs and PACs requires careful attention.

A straightforward and useful metric of HRV, termed the SDNN, is the standard deviation of all normal RR intervals (those measured between consecutive sinus beats). The SDNN may be easily calculated from a 24-hour Holter monitor. SDNN is typically measured over 24 hours and reported in units of milliseconds. Results derived from shorter (or longer) periods should not be compared to values for the accepted normal range, which are based on 24-hour records. This is because HRV is not a *weak-sense* stationary process, i.e., a process in which the mean and variance are independent of record length. Two variants of the SDNN, created by dividing the 24-hour monitoring period into 5-minute segments, are the SDNN index and the SDANN index (both with units in ms). The SDNN index is the mean of all the 5-minute standard deviations of NN (normal RR) intervals during the 24-hour period (i.e., the mean of 288 NN standard deviations), while the SDANN index is the standard deviation of all the 5-minute NN interval means (i.e., the standard deviation of 288 NN means).

The HRV indices discussed so far are called time domain measures because they are based on the time-series of normal RR intervals. Other time domain indices are the RMSSD and the pNN50. The RMSSD, or the root-mean-square successive difference, calculates the square root of the mean of the squared differences between successive NN intervals over 24 hours. The pNN50 calculates the percentage of differences between successive NN intervals over 24 hours that are greater than 50 ms. Both of these indices measure short-term variation in the NN interval because they are entirely based on comparisons between successive beats.

Of note, all the HRV indices described above, except pNN50, have units of time and thus, strictly speaking, are measures of variability in RR interval (inter-beat interval), not HR. HR and RR interval are reciprocals of each other, or to be exact, HR = 60,000/RR, where HR is expressed in units of beats per minute (bpm), and RR in units of time. Fluctuations in RR interval and HR are closely related, but not in a linear way, since the reciprocal is not a linear operation. Time domain measurements are traditionally calculated from the RR (or NN) interval sequence, even though instantaneous HR may be more closely tied to autonomic tone and, therefore, have greater physiological significance than RR interval.

2.4.5 Frequency domain measures of HRV

Additional insight into the nature of HR fluctuations may be gained by analyzing the fluctuations in the frequency domain. HRV may be broken into the frequency components that compose the overall variability. The RR series (also referred to as inter-beat interval (IBI) series) is preliminarily evenly resampled, typically at a sampling rate of 4 Hz or higher, to allow further processing based on traditional non-parametric estimation of power spectral density (PSD) based on Welch *periodogram* (Welch, 1967). Alternatively, PSD may be estimated by means of Lomb-Scargle's periodogram (LSP) (Lomb, 1976; Scargle, 1982) which does not require resampling. However, this method is based on the least-square fitting of sine waves to the data, with the underlying assumption that noise is normally distributed (Schimmel, 2001), which is questionable in RR series analysis of variability. Moreover, the accuracy of the estimates of the higher frequencies in LSP is a function of the number of RR intervals that exist with a value corresponding to the spectral region of interest (Clifford *et al.,* 2006). For instance, tachograms with no RR intervals shorter than 1.25s (IHR < 48 bpm) can still be analyzed, but there is no power contribution at 0.4 Hz, indicating the undesirable effect of data-dependent frequency resolution.

PVCs and PACs have a particularly insidious effect on the power spectral density (PSD) distribution. If they are not corrected on the time series, the effect of a sudden brief change in RR interval (or HR) is to add substantial power density at all frequencies, often masking the true variability that is being assessed. On the other hand, if the RR intervals corresponding to the ectopic beats are simply deleted, then individual frequency components become altered because the deletion of time advances the phase, by a different amount at each frequency. This has the effect of reducing the calculated power density at some frequency components and augmenting it at others. A simple solution to this problem is to replace the RR intervals affected by an ectopic beat with the same number of RR intervals of value equal to the mean of those replaced (Bilchick and Berger, 2006).

The PSD is usually integrated within specific frequency bands, since fluctuations within each band are mediated by specific physiologic mechanisms (illustrated in sections 2.1 through 2.3). The low frequency (LF) band (0.04–0.15 Hz) is related to both sympathetic and parasympathetic modulation, and the high frequency (HF) band (0.15–0.40 Hz) is governed almost exclusively by parasympathetic effects (Akselrod *et al.*, 1981). The ratio of LF to HF power is often used as a metric of sympathetic—parasympathetic balance.

2.4.6 Nonlinear measures of HRV

Although time and frequency domain measures of HRV quantify variability on various time scales, nonlinear HRV measures attempt to quantify the structure or complexity of the RR interval time series. For example, a random series of RR intervals, a normal series of RR intervals and a totally periodic series of RR intervals might have the exact same SDNN, but their underlying “organization” would be completely different. A large number of nonlinear measures of HRV have been studied, the most commonly used include the power law slope, indices from the Poincaré plot, fractal dimension, detrended fluctuation analysis, largest Lyapunov exponent, sample entropy.

Power law slope

In normal sinus rhythm, spectral power, measured over 24 hours, shows a progressive, exponential increase in amplitude with decreasing frequency. This relationship can also be plotted as the log of power (Y axis) versus the log of frequency (X axis), which transforms the exponential curve to a line whose slope can be estimated. In a log-log plot, the power law slope between 10^{-2} and 10^{-4} Hz is linear with a negative slope, and reflects the degree to which the structure of the RR interval time series is self-similar over a scale of minutes to hours. Decreased power law slope has been shown to be a marker for increased risk of mortality after myocardial infarction (Kleiger *et al.*, 2005).

Poincaré plot

The Poincaré plot is the most commonly used non-linear estimator of HRV function (Mukherjee *et al.*, 2011). In this two-dimensional representation, each RR interval is plotted against the previous one. After fitting an ellipse and plotting two axes (perpendicular to each other) to the points, one can calculate the standard deviation of the distance of the points from each axis. The SD1 (minor axis) value reflects short-term variability while SD2 (major axis) reflects long-term variability.

HRV in risk stratification analysis generally requires that the RR interval time series be plotted for an entire 24 hours Holter recording. However, plots of shorter periods, e.g. hours, can reveal details which are obscured in a 24-hour plot which involves a considerable amount of datapoints (Kleiger *et al.*, 2005).

Recent studies have suggested that Poincaré plots may also be valid markers for mental stress analysis in psychophysiological research (Mukherjee *et al.*, 2011). It is of considerable interest and benefit to see if these results are reproducible in short-term HRV, which is critical for studying cardiovascular autonomic changes in healthy subjects. Shorter time series analysis techniques are desirable because many human psychophysiological studies under controlled lab conditions are limited in how long they can be optimally maintained (Mukherjee *et al.*, 2011).

Fractal dimension

Fractal dimension (FD) is a geometric approach to measure self-similarity in a time series and is suited to measure complex fluctuations with statistical properties observed in the RR series. FD was significantly reduced in schizophrenia patients compared to controls (Bar *et al.*, 2007) and was relatively independent of heart rate. In patients with stroke involving multiple cerebral vascular territories, FD was a useful measure to distinguish between different lesion severity and from controls (D'Addio *et al.*, 2009).

Detrended fluctuation analysis

Detrended fluctuation analysis (DFA) is another measure to quantify the fractal scaling properties of the short-term RR series. The root-mean-square fluctuation of an integrated and detrended time-series is measured at different scales. The fluctuations are characterized by a scaling exponent which is the slope of the line relating to log of the fluctuation on a log scale. DFA is significantly diminished in participants with major depressive disorder when compared to controls (Schulz *et al.*, 2010).

Scaling exponent α_1, computed from DFA on a scale of 3–11 beats (Kleiger *et al.*, 2005), is a measure of the degree to which the RR interval pattern is random at one extreme, or correlated at the other. A totally random RR interval pattern has a value for α_1 of 0.5, whereas a totally correlated pattern of RR intervals, i.e., one that is totally periodic, has a value of 1.5. α_1 is usually repeatedly measured within a period of 1000 RR intervals and then averaged. Normal values are about 1.05. Decreased values for α_1 are strong predictors of outcome after MI. Another measure, α_2 can be computed in a similar way on a scale of 12–20 RR intervals. α_2, however, has not proved to be especially useful in risk stratification (Kleiger *et al.*, 2005).

Largest Lyapunov exponent

Lyapunov exponent is a simple non-linear measure of how fast two initially nearby points on a trajectory will diverge from each other as the system evolves, and a positive Lyapunov exponent is a strong indicator of chaos. Even though an m dimensional system has multiple Lyapunov exponents, the largest Lyapunov exponent (LLE) is sufficient to represent the whole system (Mukherjee *et al.*, 2011). Recent studies have shown LLE is good indicator of anxiety and mental stress and is sensitive to the effect of cardioinhibitory tricyclic antidepressants (Yeragani *et al.*, 2004; Yeragani and Rao, 2003).

Sample entropy

Entropy measures express the degree of randomness in the cardiovascular system. In healthy people, the tachogram would show high entropy. In the case of low entropy systems, the tachogram would be ordered and repetitive, showing low variability. Sample entropy (SampEn) is a regularity statistic that quantifies the unpredictability of fluctuations in the RR series. Entropy decreases in various medical conditions like schizophrenia (Bar *et al.*, 2007), major depressive disorder (Schulz *et al.*, 2010), cardiovascular diseases, and autonomic neuropathy (Khandoker *et al.*, 2010). Lempel–Ziv complexity (LZ) is another entropy metric used to measure the inherent complexity of discrete time physiologic signals. A more dynamic and robust system has a higher complexity measure (Mukherjee *et al.*, 2011).

References

Aasman J, Mulder G, Mulder LJ. Operator effort and the measurement of heart-rate variability. *Hum Factors* 1987; 29:161–70.

Acharya UR, Joseph KP, Kannathal N, Lim CM, Suri JS. Heart rate variability: a review. *Med Bio Eng Comput* 2006; 44:1031–1051.

Akselrod S, Gordon D, Ubel FA, Shannon DC, Berger AC, Cohen RJ. Power spectrum analysis of heart rate fluctuation: A quantitative probe of beat-to-beat cardiovascular control. *Science* 1981; 213:220-222.

Althaus M, Mulder LJ, Mulder G, Van Roon AM, Minderaa RB. Influence of respiratory activity on the cardiac response pattern to mental effort. *Psychophysiology* 1998; 35:420–30.

Axelrod S, Lishner M, Oz O, Bernheim J, Ravid M. Spectral analysis of fluctuations in heart rate: an objective evaluation of autonomic nervous control in chronic renal failure. *Nephron* 1987; 45:202–206.

Bar KJ, Boettger MK, Koschke M, Schulz S, Chokka P, Yeragani VK, *et al.* Non-linear complexity measures of heart rate variability in acute schizophrenia. *Clin Neurophysiol* 2007; 118:2009–15.

Bilchick KC, Berger RD. Heart Rate Variability. *J Cardiovasc Electrophysiol* 2006; 17:691–694.

Brook RD, JULIUS S. Autonomic imbalance, hypertension, and cardiovascular risk. *Am J Hypertens* 2000; 13: 112S–122S.

Capa RL, Audiffren M, Ragot S. The interactive effect of achievement motivation and task difficulty on mental effort. *Int J Psychophysiol* 2008; 70:144–50.

Carney RM, Blumenthal JA, Stein PK, Watkins L, Catellier D, Berkman LF, Czajkowski SM, O'Connor C, Stone PH, Freedland KE. Depression, heart rate variability, and acute myocardial infarction. *Circulation* 2001; 104:2024.

Carney RM, Blumenthal JA, Freedland KE, Stein PK, Howells WB, Berkman LF, Watkins LL, Czajkowski SM, Hayano J, Domitrovich PP, Jaffe AS. Low heart rate variability and the effect of depression on post—myocardial infarction mortality. *Arch Intern Med* 2005; 165:1486–1491.

Clifford GD, Azuaje F, McSharry PE (Eds.). Advanced methods and tools for ECG data analysis. *Artech House* 2006; pp. 71–79.

Cohen H, Benjamin J, Geva AB, Matar MA, Kaplan Z, Kotler M. Autonomic dysregulation in panic disorder and in post-traumatic stress disorder: application of power spectrum analysis of heart rate variability at rest and in response to recollection of trauma or panic attacks. *Psychiatry Res.* 2000; 96(1):1–13.

D'Addio G, Corbi G, Accardo A, Russo G, Ferrara N, Mazzoleni MC, *et al.* Fractal behaviour of heart rate variability reflects severity in stroke patients. *Stud Health Technol Inform* 2009; 150:794–798.

De Rivecourt M, Kuperus MN, Post WJ, Mulder LJ. Cardiovascular and eye activity measures as indices for momentary changes in mental effort during simulated flight. *Ergonomics* 2008; 51:1295–319.

Friedman BH, Thayer JF. Autonomic balance revisited: panic anxiety and heart rate variability. *J Psychosom Res.* 1998; 44(1):133–151.

Fu CH, Yang CC, Lin CL, Kuo TB. Effects of long-term vegetarian diets on cardiovascular autonomic functions in healthy postmenopausal women. *Am J Cardiol* 2006; 97:380–383.

Gerritsen J, Tenvoorde B, Dekker J, Kingma R, Kostense P, Bouter L, *et al.* Measures of cardiovascular autonomic nervous function: agreement, reproducibility, and reference values in middle age and elderly subjects. *Diabetologia* 2003; 46:330–338.

Henelius A, Hirvonen K, Holm A, Korpela J, Muller K. Mental workload classification using heart rate metrics. *Conf Proc IEEE Eng Med Biol Soc* 2009; 2009:1836–1839.

Jorna PG. Spectral analysis of heart rate and psychological state: a review of its validity as a workload index. *Biol Psychol* 1992; 34:237–57.

Khandoker AH, Jelinek HF, Moritani T, Palaniswami M. Association of cardiac autonomic neuropathy with alteration of sympatho-vagal balance through heart rate variability analysis. *Med Eng Phys* 2010; 32:161–7.

Kleiger RE, Miller JP, Bigger Jr JT, Moss AJ. Decreased heart rate variability and its association with increased mortality after acute myocardial infarction. *Am J Cardiol* 1987; 59:256–62.

Kleiger RE, Stein PK, Bigger JT Jr. Heart Rate Variability: Measurement and Clinical Utility. *Ann Noninvasive Electrocardiol* 2005; 10(1):88–101.

Lomb NR. Least-squares frequency analysis of unequally spaced data. *Astrophys Space Sci* 1976; 39:447–462.

Malpas SC, Whiteside EA, Maling TJ. Heart rate variability and cardiac autonomic function in men with chronic alcohol dependence. *Br Heart J* 1991; 65:84–88.

Melanson EL. Resting heart rate variability in men varying in habitual physical activity. *Med Sci Sports Exerc* 2000; 32:1894–901.

Mukherjee S, Yadav R, Yung I, Zajdel DP, Oken BS. Sensitivity to mental effort and test-retest reliability of heart rate variability measures in healthy seniors. *Clin Neurophysiol* 2011; 122(10):2059–66.

Mulder G, Mulder LJ. Information processing and cardiovascular control. *Psychophysiology* 1981; 18:392–402.

Paul-Labrador M, Polk D, Dwyer JH, Velasquez I, Nidich S, Rainforth M, *et al.* Effects of a randomized controlled trial of transcendental meditation on components of the metabolic syndrome in subjects with coronary heart disease. *Arch Intern Med* 2006; 166:1218–1224.

Pfeifer MA, Cook D, Brodsky J, Tice D, Reenan A, Swedine S *et al.* Quantitative evaluation of cardiac parasympathetic activity in normal and diabetic man. *Diabetes* 1982; 3:339–45.

Pinna GD, Maestri R, Torunski A, Danilowicz-Szymanowicz L, Szwoch M, La Rovere MT, *et al.* Heart rate variability measures: a fresh look at reliability. *Clin Sci* (Lond) 2007; 113:131–140.

Sandercock GR, Bromley PD, Brodie DA. The reliability of short-term measurements of heart rate variability. *Int J Cardiol* 2005; 103:238–47.

Scargle JD. Studies in astronomical time series analysis. II. Statistical aspects of unevenly spaced data. *Astrophys J* 1982; 302:757–763.

Schimmel M. Emphasizing Difficulties in the Detection of Rhythms with Lomb-Scargle Periodograms. *Biol Rhythm Res* 2001; 32(3):341–345.

Schulz S, Koschke M, Bar KJ, Voss A. The altered complexity of cardiovascular regulation in depressed patients. *Physiol Meas* 2010;31:303–21.

Singh JP, Larson MG, O'Donell CJ, Wilson PF, Tsuji H, Lyod-Jones DM, Levy D. Association of hyperglycemia with reduced heart rate variability: the Framingham heart study. *Am J Cardiol* 2000; 86:309–312.

Task Force of the European Society of Cardiology and the North American Society of Pacing and Electrophysiology. Heart rate variability: standards of measurement, physiological interpretation and clinical use. *Circulation* 1996; 93:1043–1065.

Thayer JF, Sternberg E. Beyond heart rate variability: vagal regulation of allostatic systems. Ann N Y Acad Sci. 2006; 1088:361-72.

Veltman JA, Gaillard AW. Indices of mental workload in a complex task environment. *Neuropsychobiology* 1993; 28:72–75.

Villareal RP, Liu BC, Massumi A. Heart rate variability and cardiovascular mortality. *Curr Atheroscler Rep* 2002; 4(2):120–127.

Weippert M, Thielmann B, Stoll R, Pfister EA, Bockelmann I. Sympatho-vagal balance and cardiac response to mental challenge. *Biomed Tech* (Berl) 2009; 54:197–203.

Welch PD. The Use of Fast Fourier Transform for the Estimation of Power Spectra: A Method Based on Time Averaging Over Short, Modified Periodograms. *IEEE Trans. Audio Electroacoustics* 1967; 15:70-73.

Yeragani VK, Rao R. Effect of nortriptyline and paroxetine on measures of chaos of heart rate time series in patients with panic disorder. *J Psychosom Res* 2003; 55:505–7.

Yeragani VK, Mallavarapu M, Radhakrishna RK, Tancer M, Uhde T. Linear and nonlinear measures of blood pressure variability: increased chaos of blood pressure time series in patients with panic disorder. *Depress Anxiety* 2004; 19:85–95.

Zoccali C, Ciccarelli M, Maggiore Q. Defective reflex control of heart rate in dialysis patients: evidence for an afferent autonomic lesion. *Clin Sci* 1982; 63:285–292.

Chapter 3: Atrial fibrillation

3.1 Atrial fibrillation overview

Atrial fibrillation (AF) is the most common sustained arrhythmia in humans, causing an increasing number of complications and deaths (Schotten *et al.*, 2011). Electrocardiogram (ECG)-based surveys suggest that approximately 1% of the total population is affected (Kannel *et al.*, 1998). Overall, 20–25% of all ischemic strokes are caused by AF (Miyasaka *et al.*, 2005), and AF-related strokes are more severe than strokes of other origin. The importance of cardio-embolic stroke in AF patients is highlighted by the fact that adequate anticoagulation in patients with AF can prevent strokes and reduce mortality in patients at increased risk of stroke (Connolly *et al.*, 2009; Hart *et al.*, 1999). The number of patients with AF is likely to double or triple within the next two to three decades (Hobbs *et al.*, 2005).

Numerous clinical conditions are associated with an increased incidence of AF. Most of them contribute to a gradual and progressive process of atrial remodeling characterized by changes in ion channel function, Ca^{++} homeostasis, and atrial structure such as cellular *hypertrophy*, activation of *fibroblasts*, and tissue *fibrosis*. These alterations may both favor the occurrence of “triggers” for AF that initiate the arrhythmia and enhance the formation of a substrate for AF that promotes its perpetuation.

Little is known about the mechanisms or clinical conditions that initiate episodes of the arrhythmia. A considerable portion of patients with lone AF suffer from “focal AF” that is initiated by triggers that can be localized to preferential sites, mainly the pulmonary veins (PVs). Stretch-activated or catecholamine-dependent automaticity, as well as abnormal calcium handling, have been suggested as mechanisms causing AF in focal AF patients (Schotten *et al.*, 2011).

3.2 Atrial electrophysiology

The predominant shape of atrial myocytes’ action potential is triangular with a gradual repolarization phase as shown in Figure 3.1. If a plateau is present, it is less pronounced than in ventricular myocytes. As in ventricular myocytes, the main depolarizing currents are the rapidly activating and inactivating Na^+-current (I_{Na}) and the L-type Ca^{++} current (I_{CaL}), characterized by slower kinetics. The differences in action potential morphology between atria and ventricles are mainly caused by differences in ion channel current density and kinetics of repolarizing currents.

The membrane resistance of atrial myocytes at rest is relatively high, and thus less depolarizing current is required to reach the action potential threshold, making atrial myocytes inherently more excitable. Within the atria, considerable regional variation in action potential morphology exists. PV myocytes differ from left atrial myocytes, with a more depolarized resting membrane potential, lower upstroke velocity, and shorter action potential. In some areas, like the *crista terminalis* (the junction between the right atrium and the right auricle shown in Figure 3.2), the *epicardium* has shorter atrial action potential duration (APD) than the *endocardium*. These cells in the *crista terminalis* and Bachmann's bundle may form specialized rapidly conducting tracts within the atrium.

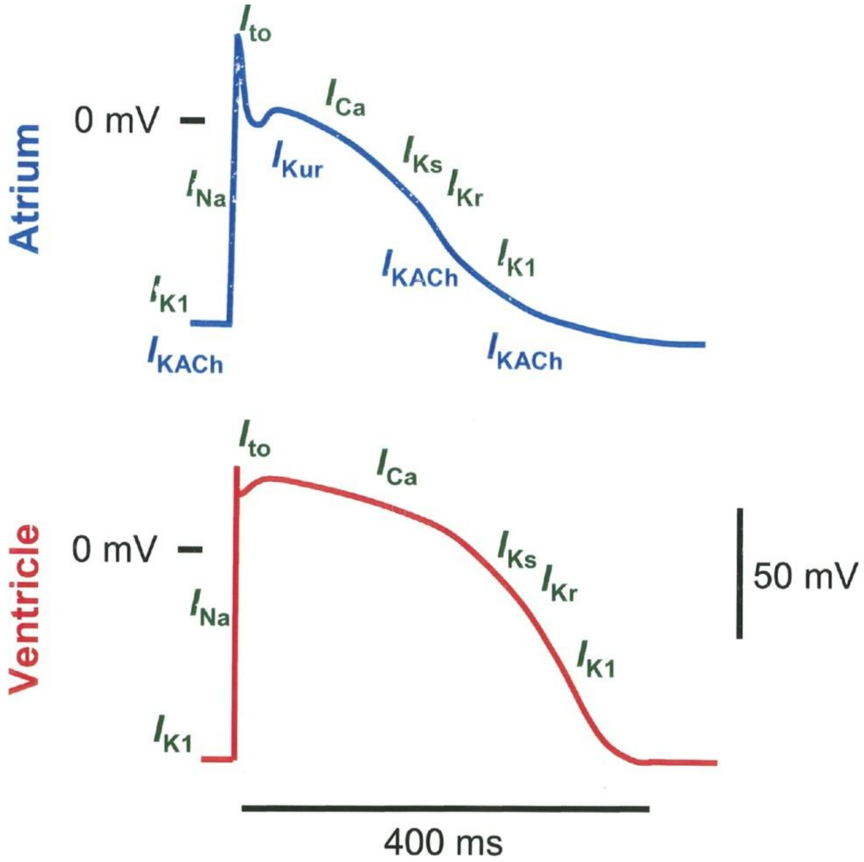

Figure 3.1 Regional Difference in Ionic Current Contribution to action potential (From: Ehrlich, JR et al. *J Am Coll Cardiol* 2008; 51:787-792)

3.2.1 Electrophysiological basis of PV ectopy

In humans, paroxysms of AF often originate in the myocardial sleeves of the PVs. However, the PVs in the adult heart consist mainly of myocytes morphologically very similar to normal atrial myocytes, and the contribution of scattered abnormal cell types with possible pacemaking properties remains to be established (Schotten *et al.*, 2011).

Apart from differences in cellular electrophysiology, the PV area also shows salient features in gross anatomy and fiber geometry. In patients, there may be a relation between PV structure and the presence of AF. In a recent study (Kholova and Kautzner, 2004) the superior PVs had longer and thicker sleeves in AF patients. Guerra and co-workers (Guerra *et al.*, 2003) specifically linked areas of PV wall thickening to high-frequency potentials and the origin of ectopic beats. Moreover, in a study by Hassink and co-workers (Hassink *et al.*, 2003) PVs in AF patients also showed more *fibrosis* and discontinuities.

In addition to the PVs, arrhythmic activity may also originate from “myocardial sleeves” in other atrial regions, such as myocardial extensions in the atrioventricular valves and coronary sinus.

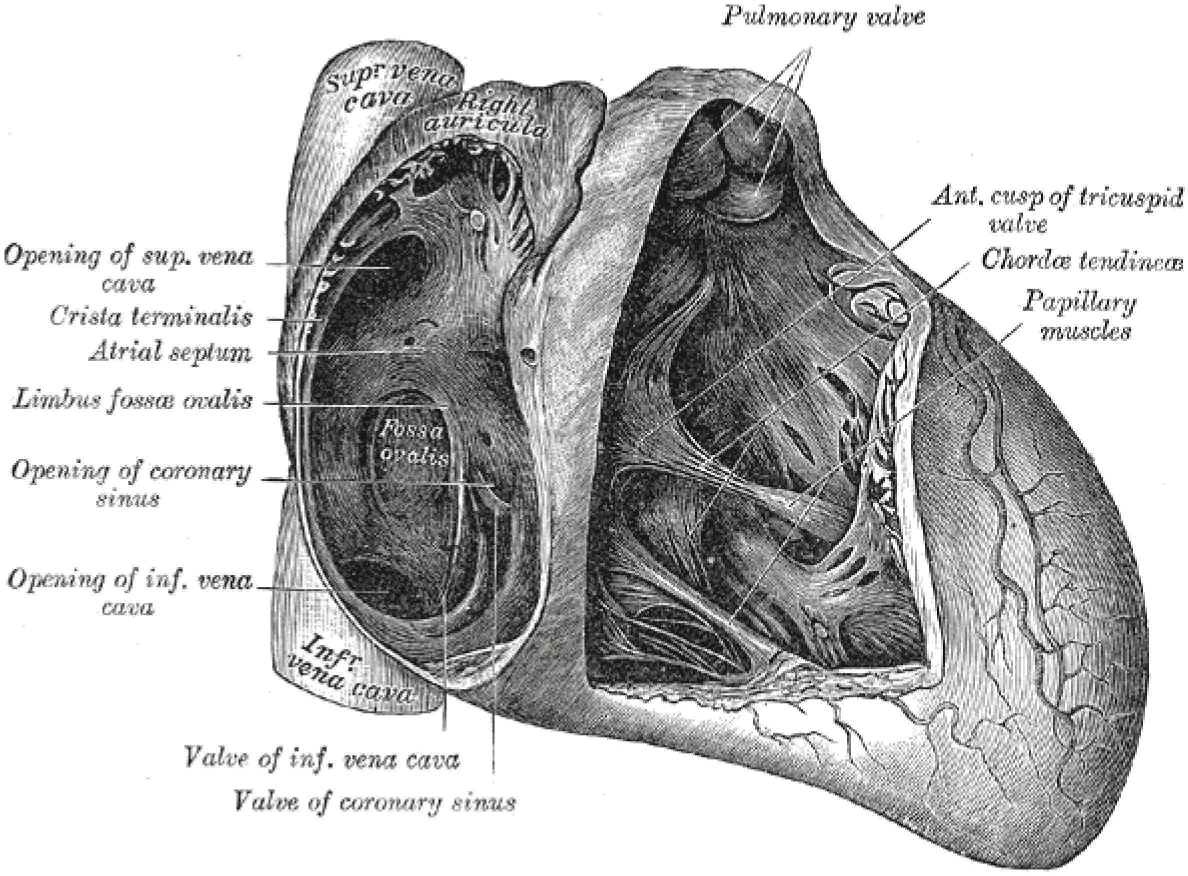

Figure 3.2 Frontal interior view of the heart (From: www.wikipedia.org, non copyrighted)

3.3 Excitation-contraction coupling

Excitation-contraction coupling is initiated by depolarization of the cell membrane by an action potential that triggers opening of voltage-dependent L-type Ca^{++} channels. Influx of Ca^{++} triggers the release of Ca^{++} from the *sarcoplasmic* reticulum in a process called Ca^{++}-induced Ca^{++} release. Ca^{++} binds to *troponin C* activating the *actin-myosin* filaments, and the myocyte starts to contract. Relaxation is initiated by a decline of the Ca++ concentration in the cytosol mainly by re-sequestration of Ca^{++} into the sarcoplasmic reticulum and extrusion to the extracellular space (Schotten *et al.*, 2011).

3.4 Elementary proarrhythmic mechanisms during atrial fibrillation

Elementary proarrhythmic mechanisms in AF may be categorized in enhanced automaticity and triggered activity (Schotten *et al.*, 2011). The first occurs when myocytes possessing pacemaker activity increase their rate of spontaneous discharge. Enhanced automaticity can be due to a lowered threshold of the action potential upstroke (*phase* 0), a less negative maximal diastolic potential, or an increase in the slope of spontaneous diastolic depolarization (*phase* 4). However, there is little evidence for the existence of enhanced automaticity as a proarrhythmic mechanism during AF.

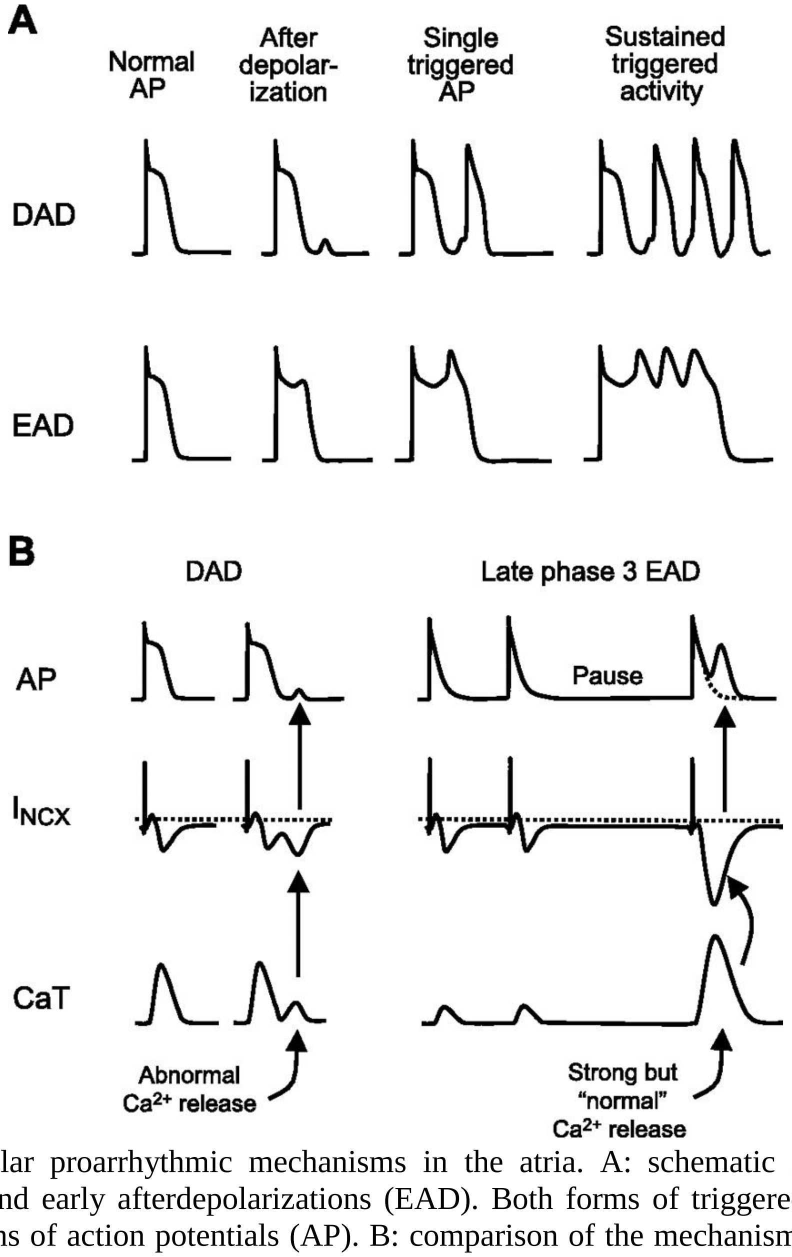

Figure 3.3 Cellular proarrhythmic mechanisms in the atria. A: schematic illustration of delayed (DAD) and early afterdepolarizations (EAD). Both forms of triggered activity can elicit single or runs of action potentials (AP). B: comparison of the mechanism of DAD and late phase 3 EAD (From: Schotten U *et al.*, *Physiol Rev* 2011; 91:265-325)

Triggered activity arises from membrane oscillations following normal action potentials (i.e., the trigger). If such membrane oscillations reach threshold of depolarizing currents, they can provoke new action potentials. Under certain circumstances, such triggered responses can in turn elicit new action potentials, resulting in self-sustaining runs of triggered activity

(Figure 3.3). Depending on when the membrane oscillation occurs, “early” and “delayed” *afterdepolarizations* are distinguished.

Delayed *afterdepolarizations* (DADs) are membrane potential oscillations occurring after full repolarization of the triggering action potential. DADs are favored by conditions producing Ca^{++} overload, like ischemia, β-adrenergic stimulation, low extracellular K concentration, and tachycardia (Coetzee and Opie, 1987; Katra and Laurita, 2005).

Early afterdepolarizations (EADs) are membrane oscillations occurring during phase 2 or 3 of the action potential. They occur in the presence of action potential prolongation. During the prolonged action potentials, “Ca^{++} window currents” may get activated producing a new action potential upstroke (Minget *et al.*, 1994). Another mechanism likely involved in EADs occurring during β–adrenergic stimulation is spontaneous release of Ca^{++} from the sarcoplasmic reticulum due to elevated cytosolic Ca^{++} concentrations (Volders *et al.*, 1997). In most cases, EADs occur in *bradycardia* while DADs are more likely to occur during *tachycardia* or rapid pacing.

3.5 Mechanisms of reentry

In the late 1950s, computer models of AF demonstrated that, based on simple assumptions regarding refractoriness and conduction velocity, reentrant wavelets might wander through an excitable medium in a seemingly chaotic pattern (Moe and Abildskov, 1959). According to Moe’s “multiple wavelet hypothesis,” fibrillation wavefronts continuously undergo wavefront-wave tail interactions resulting in wave break and generation of new wavefronts. On the other hand, block, collision, and fusion of wavefronts will tend to reduce their number. As long as the number of wavefronts does not decline below a critical level, multiple wavelets will be capable to sustain the arrhythmia (Moe, 1968; Moe *et al.*, 1964). Factors increasing the stability of the fibrillation process include shortening of the refractory period, increased heterogeneity of refractoriness, slowing of conduction, and an increase of the tissue mass. In contrast, prolongation of refractoriness, enhancement of conduction velocity, and reduction of the available substrate will reduce the number of wavefronts until the arrhythmia ceases.

For a long time, reentry of excitation wavefronts was considered the main mechanism of AF. However, the discovery of localized sources of paroxysmal AF originating from the PVs (Haissaguerre *et al.*, 1998) has renewed the interest in “focal” sources of AF. Both cellular proarrhythmic mechanisms, like automaticity or triggered activity, and reentrant mechanisms might underlie these phenomena. The relative contribution of these distinct mechanisms, however, is likely to vary between individual patients and cannot be fully determined at present (Schotten *et al.*, 2011). Moreover, it has recently been suggested that the multiple wavelet hypothesis would actually not exclude the coexistence of local sources of AF (Vaquero *et al.*, 2008), as in certain substrates, stable rotors may act as a source of multiple wavelets.

3.6 Atrial remodeling in AF

Ion channel remodeling and shortening of refractoriness occur in AF patients. Paroxysms of AF often tend to become longer with time, ultimately leading to persistent AF. Several clinical studies have shown that atrial APD in AF patients is shorter than in patients in sinus rhythm (Attuel *et al.*, 1982; Boutjdir *et al.*, 1986; Daoud *et al.*, 1996; Franz *et al.*, 1997; Yu *et al.*, 1999). In addition to atrial effective refractory period (AERP) shortening, AF patients show a loss of rate adaptation of the AERP (Attuel *et al.*, 1982; Boutjdir *et al.*, 1986; Franz *et al.*, 1997). Some studies have also reported an increased AERP dispersion (Michelucci *et al.*, 1982; Misier *et al.*, 1992).

Often, AF can be *cardioverted* by agents that prolong the atrial APD. This indicates that a prolongation of the AERP is antiarrhythmic but does not show to which extent the AERP shortening contributes to AF stability. The exact time course of electrical remodeling during AF in humans is unknown, but in animal models it is complete within at most a few days. The limited efficacy of ion channel blockers in the treatment of chronic AF indicates that other processes occurring more slowly than electrical remodeling contribute to the stability of AF in many patients (Schotten *et al.*, 2011).

Alterations in atrial tissue structure likely contribute to the high susceptibility to the arrhythmia in patients with AF. However, the majority of chronic AF patients is of advanced age or suffers from structural heart disease. Of the various aspects of atrial structural remodeling in these patients, the consequences of *fibrosis*, myocyte hypertrophy, and altered *connexin* (the protein structure forming the atrial gap junctions) distribution have been studied extensively.

Atrial *fibrosis* is thought to be one of the most important factors in the formation of a substrate for AF. Atrial *fibrosis* has been observed in biopsies from patients with AF as well as in patients with specific risk factors for AF, such as valvular disease, rheumatic heart disease, dilated and hypertrophic cardiomyopathy, and advanced age (Schotten *et al.*, 2011). Myocytes are organized in bundles, in which strands of myocytes can be separated from each other by fibrous tissue. Structural remodeling due to heart disease is often associated with *fibrosis* and an increased transverse fiber separation.

Another relevant factor for atrial conduction may be altered *connexin* expression. In the working myocardium, conduction velocity is higher in the longitudinal than in the transverse direction. In the transverse direction, a propagating wavefront has to cross more cell-to-cell boundaries within a given distance. Several studies have reported alterations in *connexin* expressions in patients with AF, but the observations are not consistent (Schotten *et al.* 2011).

Moreover, some aspects of the atrial architecture itself, apart from pathological structural changes, may play a role in creating a substrate for AF. Based on anatomical and histological studies of the atria, areas with strong preferential fiber orientation include the *crista terminalis*, the bundle of Bachmann, and the area in between the PVs. With the intrinsic anisotropy of these regions, structural remodeling may readily lead to dissociated conduction patterns. One of the challenges ahead is to link the various conduction patterns during AF to the underlying tissue architecture and pathological changes to elucidate the electro-pathological substrate for perpetuation of AF (Schotten *et al.*, 2011).

3.7 Assessment of the AF substrate by fibrillation electrogram analysis

As described earlier, alterations in myocyte electrophysiology and tissue structure can create a substrate for AF. Thus more specific treatment strategies require diagnostic tools that allow assessment of the nature and severity of the AF substrate in patients. A simple electrocardiographic measure, “coarse” versus “fine” AF, does not correlate well with atrial size (Bollmann *et al.*, 2001; Waggoner *et al.*, 1976), heart disease etiology (Morganroth *et al.*, 1979), or average AF cycle length (Pehrson *et al.*, 1998), although it may be indicative of *thromboembolic* risk (Yamamoto *et al.*, 2005). However, the dominant atrial cycle length determined from surface lead V1 by Fast Fourier Transform does reflect a spatial average of the AF cycle length in the right atrium (Holm *et al.*, 1998; Husser *et al.*, 2007b, Pehrson *et al.*, 1998). In patients with new-onset AF, the dominant atrial cycle length was higher with increasing age, increased with AF duration, and was lower in patients who cardioverted spontaneously within the subsequent 24 h (Husser *et al.*, 2007a). At present, the most extensive information on the AF substrate in humans has come from studies that have investigated atrial *electrograms* recorded in patients with AF. The distribution of dominant frequencies, fractionation of *electrograms*, and direct mapping of conduction patterns are the main analysis techniques used.

Dominant frequency analysis is a relatively simple and time-efficient method for determining the AF cycle length. Power spectral density is analyzed for recorded *electrogram* signals. The dominant frequency is the highest peak in the PSD spectrum (Ng and Goldberger, 2007). In principle, a relatively high dominant frequency may be caused by a rapid ectopic focus, dissociated conduction, a reentrant circuit or even an artifact. Dominant frequency analysis often correlates well with the AF cycle length, but it is sensitive to the signal quality, recording method (unipolar vs. bipolar), and electrogram fractionation (Ng *et al.*, 2007).

References

Bollmann A, Binias KH, Sonne K, Grothues F, Esperer HD, Nikutta P, Klein HU. Electrocardiographic characteristics in patients with nonrheumatic atrial fibrillation and their relation to echocardiographic parameters. *Pacing Clin Electrophysiol* 2001; 24:1507–1513.

Coetzee WA, Opie LH. Effects of components of ischemia and metabolic inhibition on delayed afterdepolarizations in guinea pig papillary muscle. *Circ Res* 1987; 61:157–165.

Daoud EG, Bogun F, Goyal R, Harvey M, Man KC, Strickberger SA, Morady F. Effect of atrial fibrillation on atrial refractoriness in humans. *Circulation* 1996; 94:1600–1606.

Franz MR, Karasik PL, Li C, Moubarak J, Chavez M. Electrical remodeling of the human atrium: similar effects in patients with chronic atrial fibrillation and atrial flutter. *J Am Coll Cardiol* 1997; 30:1785–1792.

Guerra PG, Thibault B, Dubuc M, Talajic M, Roy D, Crepeau J, Nattel S, Tardif JC. Identification of atrial tissue in pulmonary veins using intravascular ultrasound. *J Am Soc Echocardiogr* 2003; 16: 982–987.

Haissaguerre M, Jais P, Shah DC, Takahashi A, Hocini M, Quiniou G, Garrigue S, LeMouroux A, LeMetayer P, Clementy J. Spontaneous initiation of atrial fibrillation by ectopic beats originating in the pulmonary veins. *N Engl J Med* 1998; 339: 659–666.

Hassink RJ, Aretz HT, Ruskin J, Keane D. Morphology of atrial myocardium in human pulmonary veins: a postmortem analysis in patients with and without atrial fibrillation. *J Am Coll Cardiol* 2003; 42: 1108–1114.

Hobbs FD, Fitzmaurice DA, Mant J, Murray E, Jowett S, Bryan S, Raftery J, Davies M, Lip G. A randomised controlled trial and cost-effectiveness study of systematic screening (targeted and total population screening) versus routine practice for the detection of atrial fibrillation in people aged 65 and over. *The SAFE study Health Technol Assess* 2005; 9: iii-iv, ix-x, 1–74.

Holm M, Pehrson S, Ingemansson M, Sornmo L, Johansson R, Sandhall L, Sunemark M, Smideberg B, Olsson C, Olsson SB. Non-invasive assessment of the atrial cycle length during atrial fibrillation in man: introducing, validating and illustrating a new ECG method. *Cardiovasc Res* 1998; 38:69–81.

Husser D, Cannom DS, Bhandari AK, Stridh M, Sornmo L, Olsson SB, Bollmann A. Electrocardiographic characteristics of fibrillatory waves in new-onset atrial fibrillation. *Europace* 2007a; 9:638–642.

Husser D, Stridh M, Cannom DS, Bhandari AK, Girsky MJ, Kang S, Sornmo L, Bertil Olsson S, Bollmann A. Validation and clinical application of time-frequency analysis of atrial fibrillation electrocardiograms. J Cardiovasc Electrophysiol 2007b; 18:41–46.

Kannel WB, Wolf PA, Benjamin EJ, Levy D. Prevalence, incidence, prognosis, and predisposing conditions for atrial fibrillation: population-based estimates. *Am J Cardiol* 1998; 82:2N–9N.

Katra RP, Laurita KR. Cellular mechanism of calcium-mediated triggered activity in the heart. *Circ Res* 2005; 96:535–542.

Kholova I, Kautzner J. Morphology of atrial myocardial extensions into human caval veins: a postmortem study in patients with and without atrial fibrillation. *Circulation* 2004; 110: 483–488.

Markides V, Schilling RJ, Ho SY, Chow AW, Davies DW, Peters NS. Characterization of left atrial activation in the intact human heart. *Circulation* 2003; 107: 733–739.

Michelucci A, Padeletti L, Fradella GA. Atrial refractoriness and spontaneous or induced atrial fibrillation. *Acta Cardiol* 1982; 37:333–344.

Ming Z, Nordin C, Aronson RS. Role of L-type calcium channel window current in generating current-induced early afterdepolarizations. *J Cardiovasc Electrophysiol* 1994; 5:323–334.

Misier AR, Opthof T, van Hemel NM, Defauw JJ, de Bakker JM, Janse MJ, van Capelle FJ. Increased dispersion of "refractoriness" in patients with idiopathic paroxysmal atrial fibrillation. *J Am Coll Cardiol* 1992; 19:1531–1535.

Moe GK. A conceptual model of atrial fibrillation. *J Electrocardiol* 1968; 1:145–146.

Moe GK, Abildskov JA. Atrial fibrillation as a self-sustaining arrhythmia independent of focal discharge. *Am Heart J* 1959; 58:59–70.

Moe GK, Rheinboldt WC, Abildskov JA. A computer model of atrial fibrillation. *Am Heart J* 1964; 67:200–220.

Morganroth J, Horowitz LN, Josephson ME, Kastor JA. Relationship of atrial fibrillatory wave amplitude to left atrial size and etiology of heart disease. An old generalization re-examined. *Am Heart J* 1979; 97:184–186.

Ng J, Goldberger JJ. Understanding and interpreting dominant frequency analysis of AF electrograms. *J Cardiovasc Electrophysiol* 2007; 18:680–685.

Ng J, Kadish AH, Goldberger JJ. Technical considerations for dominant frequency analysis. *J Cardiovasc Electrophysiol* 2007; 18:757–764.

Pehrson S, Holm M, Meurling C, Ingemansson M, Smideberg B, Sornmo L, Olsson SB. Non-invasive assessment of magnitude and dispersion of atrial cycle length during chronic atrial fibrillation in man. *Eur Heart J* 1998; 19:1836–1844.

Schotten U, Verheule S, Kirchhof P, Goette A. Pathophysiological mechanisms of atrial fibrillation: a translational appraisal. *Physiol Rev* 2011; 91(1):265–325.

Vaquero M, Calvo D, Jalife J. Cardiac fibrillation: from ion channels to rotors in the human heart. *Heart Rhythm* 2008; 5:872–879.

Volders PG, Kulcsar A, Vos MA, Sipido KR, Wellens HJ, Lazzara R, Szabo B. Similarities between early and delayed afterdepolarizations induced by isoproterenol in canine ventricular myocytes. *Cardiovasc Res* 1997; 34:348–359.

Waggoner AD, Adyanthaya AV, Quinones MA, Alexander JK. Left atrial enlargement. Echocardiographic assessment of electrocardiographic criteria. *Circulation* 1976; 54:553–557.

Yamamoto S, Suwa M, Ito T, Murakami S, Umeda T, Tokaji Y, Sakai Y, Kitaura Y. Comparison of frequency of thromboembolic events and echocardiographic findings in patients with chronic nonvalvular atrial fibrillation and coarse versus fine electrocardiographic fibrillatory waves. *Am J Cardiol* 2005; 96:408–411.

Yu WC, Lee SH, Tai CT, Tsai CF, Hsieh MH, Chen CC, Ding YA, Chang MS, Chen SA. Reversal of atrial electrical remodeling following cardioversion of long-standing atrial fibrillation in man. *Cardiovasc Res* 1999; 42:470–476.

Part II

This part presents the analysis of inter-beat interval (or inversely, heart rate) variability in mental workload assessment, in a memory search task. As ECG artifacts represent a major concern in ambulatory settings, the topic was addressed by a specific study on automatic quality assessment of ambulatory ECG recordings, presented in Chapter 4 . Experimental setup for data acquisition is presented in Chapter 5, together with the software architecture of a real-time monitor specifically designed for data acquisition, visualization, processing and storage. In Chapters 6-7 the analysis of heart rate variability is presented. Established methods are compared (Chapter 6) on experimental data, and a novel approach based on performance indices and joint time-frequency distribution of inter-beat interval variability is presented (Chapter 7).

Scientific work:

Chapter 4:

Langley P, Di Marco LY, King S, Di Maria C, Duan W, Bojarnejad M, Wang K, Zheng D, Allen J, Murray A. An algorithm for assessment of ECG quality acquired via mobile telephone. *Comput Cardiol* 2011; 38:281−284

Chapter 6:

Di Marco LY, Sottile R, Chiari L. Time-Frequency analysis of cardio-respiratory response to mental task execution. *Comput Cardiol* 2010;37:753−756.

Chapter 4: Automatic assessment of ambulatory ECG recording quality

4.1 Introduction

The acquisition of the ECG in ambulatory settings, namely in conditions in which subjects are allowed to move and perform the ordinary activities of the daily life, presents additional challenges with respect to the clinical setting where subjects undergoing ECG recordings lie supine in comfortable and quiet conditions.

One major problem is the high level of in-band noise encountered (usually muscle- or movement-related). Another problem in ambulatory recordings, especially for long term monitoring, is the degradation in electrode contact over time, leading to a lower signal-to-noise ratio (Clifford *et al.*, 2006). Moreover, ambulatory recordings are generally performed away from the hospital environment, by operators that may not be specifically or adequately trained. As a consequence, key aspects such as electrodes placement (location and contact stability) and signal quality (compliance with ECG diagnostic interpretation requirements) are often overlooked.

In recent years, the evolution of mobile technologies has substantially enhanced the potential of small, lightweight, and power efficient handheld devices (Chaudhuri *et al.*, 2009; Klug *et al.*, 2010; Langley *et al.*, 2011; Romero, 2010). The computational resources available on mobile platforms have increased dramatically, allowing a considerable amount of signal processing to be implemented onboard. The post-processing generally required for typically noisy ambulatory recordings, can be integrated in the software application running on the mobile device.

Of great interest is the possibility to automatically process and determine the quality of the recorded ECG for the specific purpose of the application, whether it be a simple heart rate monitor or the diagnostic interpretation of the ECG signal.

4.2 Noise sources in ambulatory ECG

Noise and artifacts affecting the ECG can occur within the frequency band of interest and can manifest with similar morphologies as the ECG itself, making it a challenging task to separate the signal from the undesired contaminants. The most common undesired sources of ECG corruption include:

Power line interference: 50 Hz mains noise (or 60 Hz in some Countries) with an amplitude of up to 50% of full scale deflection (peak-to-peak ECG amplitude);

Electrode contact noise: loss of contact between the electrode and the skin manifesting as sharp changes with full scale saturation on the ECG (usually due to an electrode being nearly or completely pulled off);

Patient–electrode motion artifacts: movement of the electrode on the skin, leading to impedance variations between the electrode and skin, usually manifesting as rapid baseline jumps or complete saturation of the ECG for up to 0.5 s;

Electromyographic (EMG) noise: electrical activity due to muscle contractions in the frequency range between 0 and 10 KHz;

Baseline wander: usually from respiration at frequencies between 0.15 and 0.3 Hz, or electrode contact degradation.

Although each of these contaminants can be reduced by careful and experienced use of the devices and experimental setup, it is impossible to remove them completely. Therefore, it is important to quantify the nature of the noise in a particular data set and choose an appropriate algorithm for post-processing, with the goal of increasing the signal-to-noise ratio (Clifford *et al.*, 2006).

4.3 Methods

4.3.1 Database

In this study the training set A (SetA) database of Physionet's Challenge 2011 was used. The database consisted in 998 ambulatory recordings of 12-leads ECG (sampled at F_s=500 samples/s, with amplitude resolution of 5μV, 16-bit/sample), each of 10 s duration. The recordings were classified by trained personnel in two categories: 'acceptable' quality (773 recordings) and 'unacceptable' quality (225 recordings), based on subjective, undisclosed criteria.

Two training sets (TS_1, TS_2) were extracted from the dataset SetA, as shown in Table 4.1. The first was created by randomly selecting 100 'acceptable' and 100 'unacceptable' records (TS_1), so that there were an equal number of recordings in each classification category. The second was created by randomly selecting 50% of the 'acceptable' and 'unacceptable' records (TS_2), so that the training set maintained the balance between 'acceptable' and 'unacceptable' recordings of the complete data set.

Table 4.1 – Training and Test Sets

Set	# Acceptable Records	# Unacceptable Records	Total
TS_1	100	100	200
TS_2	386	112	498
XS_1	673	125	798
XS_2	387	113	500
SetA	773	225	998

Consequently, two test sets were defined (XS_1, XS_2) as the remaining records after extracting TS_1, TS_2 from SetA.

4.3.2 Algorithm overview

The algorithm comprised two stages: 1) noise and artifact quantification; and 2) classification based on a single condition decision rule. The first stage computed meaningful parameters in signal quality determination and included baseline drift, constant amplitude (flat line), QRS-band noise, high frequency noise (spurious spikes), non-ECG noise (white noise), amplitude step-wise changes and saturation, and low-amplitude signals. Detection of pacemaker spikes and QRS complexes are pre-requisites. The second stage assigned the binary decision 'Acceptable' or 'Unacceptable' according to pre-determined thresholds for noise and artifact measured in stage 1.

The block diagram of the algorithm's architecture is illustrated in Figure 4.1.

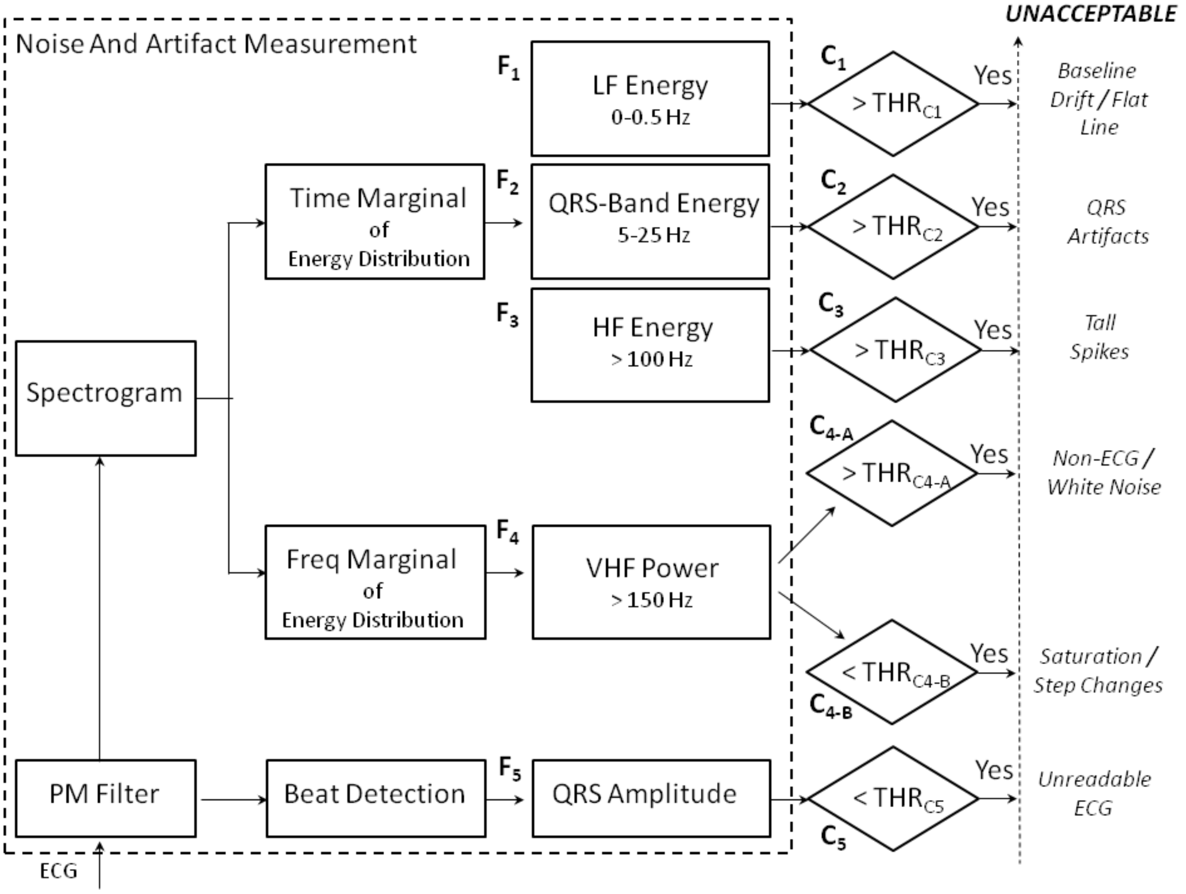

Figure 4.1 Block diagram of the algorithm. For each lead, the ECG is filtered for pace-maker removal and further processed for beat detection and spectral analysis. Features $F_1,\ldots, F_4$ are extracted from joint time-frequency analysis, feature F_5 from the detected QRS complexes. The classification stage comprises a series of single-condition decision rules (C_j) that compares the extracted features to condition specific thresholds (THR_{Cj}).

4.3.2.1 Noise and artifact measurement

This section describes the methods used to quantify the noise and artifact characteristics present in the ECG. For each individual lead, four features (F_1, F_2, F_3, F_4) were calculated from the joint-time frequency (JTF) analysis of the raw ECG signal, and one (F_5) from he detected QRS complexes.

JTF representation of the temporal-spectral distribution of the ECG energy was estimated by the non-parametric method based on Short-time Fourier transform (STFT) spectrogram (Fast-Fourier Transform (FFT) computed over 2048 samples sliding windows (approximately 4 s), with 80% overlap, yielding a frequency resolution of 0.24 Hz).

For a given frequency band of interest $\Delta F=[f_L, f_H]$, the time marginal of the energy distribution $E_{\Delta F}(t)$ is calculated as:

$$E_{\Delta F}(t) = \sum_{f=f_L}^{f_H} |S(f,t)|^2 \tag{4.1}$$

where $S(f, t)$ is the spectrogram estimated for the frequency value f, at the time instant t.

Similarly, for a given time interval $\Delta T=[t_1, t_2]$, the frequency marginal $P_{\Delta T}(f)$ of the energy distribution in the time interval is defined as:

$$P_{\Delta T}(f) = \sum_{t=t_1}^{t_2} |S(f,t)|^2 \tag{4.2}$$

The following features are calculated in each individual lead.

F1) Low-frequency time marginal energy (E_{LF}): defined as the peak value of $E_{\Delta F}(t)$ in the frequency band [0, 0.5] Hz:

$$E_{LF} = \max_t \{E_{\Delta F=[0,0.5]}(t)\} \tag{4.3}$$

High values of this parameter indicate the presence of prominent baseline drift or constant amplitude level (“flat line”) in the original ECG signal.

F2) QRS-band time marginal energy (E_{QRS}): defined as the peak value of $E_{\Delta F}(t)$ in the characteristic frequency band of the QRS complex (5-25 Hz):

$$E_{QRS} = \max_t \{E_{\Delta F=[5,25]}(t)\} \tag{4.4}$$

Very high values of this parameter indicate the presence of QRS-artifacts in the original ECG signal.

F3) High-frequency time marginal energy (E_{HF}): defined as the peak value of $E_{\Delta F}(t)$ in the frequency band above 100 Hz:

$$E_{HF} = \max_t \{E_{\Delta F=[100,F_s/2]}(t)\} \tag{4.5}$$

High values of this parameter indicate the presence of spurious spikes in the original ECG signal.

F4) Very high frequency (VHF) frequency marginal (power) (P_{VHF}): defined as the median value in the frequency band above 150 Hz of normalized $P_{\Delta T}(f)$, over the entire recording (ΔT=10 s):

$$P_{VHF} = \frac{\underset{f>150Hz}{median}\left\{P_{\Delta T=[0,10s]}(f)\right\}}{\underset{f}{max}\left\{P_{\Delta T=[0,10s]}(f)\right\}} \tag{4.6}$$

High values of this parameter indicate the presence of non-ECG noise (e.g. white noise), whereas extremely low values indicate the presence of isolated saturation with step-wise amplitude changes in the original ECG signal.

F5) QRS amplitude (QRS-A): defined as the median value of the peak-to-nadir amplitude difference of the QRS complexes detected.

4.3.2.2 Pacemaker filter and beat detection

As a pre-requisite for QRS amplitude assessment it was necessary to perform QRS detection and to detect and remove pace-maker artifact.

Pace-maker spike detection was accomplished using a sliding window (*w*) of 1s (50% overlap). The maximum absolute value of the first derivative $D1_l(w)$ was calculated for each window. The median value $M\{D1_l(w)\}$ was stored for each lead. The lead exhibiting the highest $M\{D1_l(w)\}$ was selected for isolated spikes detection. Spikes whose amplitude was greater than a fixed threshold of 100μV/sample, whose duration did not exceed 10 ms, and not surrounded by others within a window of 250 ms on each side, were considered as pace-maker artifact. Pace-maker artifact was removed so that for each detected spike, the 20 ms interval centered around the spike peak was assigned a constant value equal to the average amplitude within the window.

Beat detection was computed with the QRS detection algorithm proposed by Pan and Tompkins (Pan and Tompkins, 1985) on the lead whose windowed kurtosis (median kurtosis value over a sliding window of 2 s, 50% overlap) was the highest, and the ECG peak-to-nadir amplitude difference did not exceed a threshold of 5 mV. For each detected beat, the fiducial point was set to the dominant peak of the QRS complex.

Figure 4.2 shows examples of pacemaker filtering and beat detection. Pacemaker filtering (rejection) is crucial for QRS amplitude determination: if pacemaker spikes are not filtered out properly, the beat detection algorithm can be misled and pacemaker spikes considered as QRS complexes, thereby altering QRS amplitude calculation.

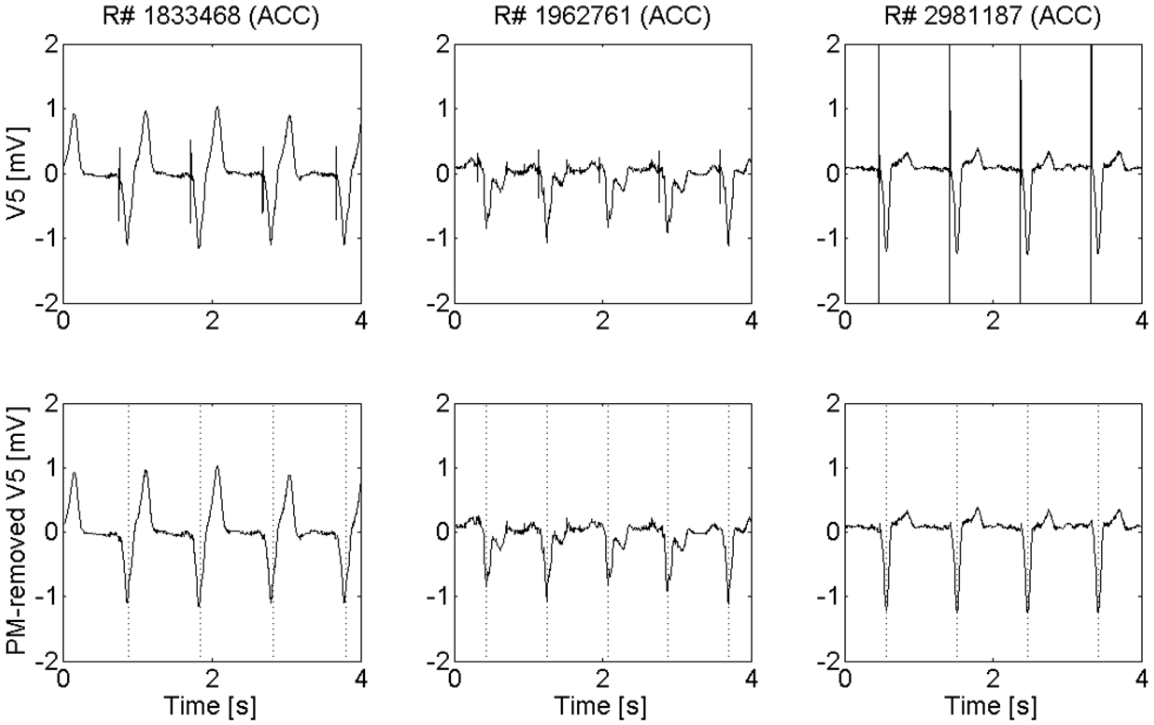

Figure 4.2 Examples of pace-maker filtering. Original ECG precordial lead V5 (top panels) and filtered signals after pacemaker (PM) rejection (bottom panels). Dotted vertical lines in bottom panels indicate QRS fiducial point of each detected beat (beat detection is performed after PM removal).

4.3.2.3 Classification based on single-condition decision rule

Unlike supervised learning classification algorithms a heuristic approach based on cascaded single-condition decision rules (SCDR) offers the potential advantage of providing additional information to the user, yielding not only a classification result (e.g. ‘acceptable’ vs. ‘unacceptable’) but also a “rejection reason” for recordings classified as ‘unacceptable’. The advantage of such a method would be the possibility for the user to take action in correcting the measurement problem (e.g. verifying electrode contact, stabilizing patient posture). The SCDR classification algorithm consisted of the cascaded verification of single conditions (C_j) as illustrated in figure 1. The condition rules (Figure 4.1) are tested for each single lead. A 12-by-6 condition matrix M_C is defined, to account for six conditions, tested for all twelve leads. The six conditions can be described as follows:

C_1: Is E_{LF} greater than a threshold THR_{C1}? If yes, set to logical “1” the corresponding bit in the condition matrix: $M_C(ld, 1) = 1$, where $ld = 1,\dots,12$ is the lead index. . This condition aims to detect the presence of baseline drift or constant amplitude (“flat line”) in the ECG signal.

C_2: Is E_{QRS} greater than a threshold THR_{C2}? If yes, set $M_C(ld, 2) = 1$. This condition aims to detect the presence of QRS artifacts in the ECG signal.

C_3: Is E_{HF} greater than a threshold THR_{C3}? If yes, set $M_C(ld, 3) = 1$. This condition aims to detect the presence of bursts of sharp, spurious spikes in the ECG signal.

$C_{4\text{-}A}$: Is P_{VHF} greater than a threshold $THR_{C4\text{-}A}$? If yes, set $M_C(ld, 4) = 1$. This condition aims to detect the presence of non-ECG noise (e.g. white noise) in the original ECG signal.

$C_{4\text{-}B}$: Is P_{VHF} smaller than a threshold $THR_{C4\text{-}B}$? If yes, set $M_C(ld, 5) = 1$. This condition aims to detect the presence of isolated saturation with step-wise amplitude changes in the original ECG signal.

C_5: Is $QRS\text{-}A$ smaller than a threshold THR_{C5}? If yes, set $M_C(ld, 6) = 1$. This condition aims to detect unreadable ECG.

4.3.2.4 Determination of thresholds for classification

Each condition rule required the specification of a threshold for determining the classification outcome.

For a given condition C, the number of true positives TP_C (and true positive rate $TPRc$) depends on the threshold value THR_C and the number of leads NL (=1,…12) the condition is satisfied for:

$$\begin{aligned} &TP_C = TP_C(NL, THR_C) \equiv (C(NL, THR_C) = True) \wedge (record\ annotated\ UNACC) \\ &TPRc \equiv \frac{\#TP_C}{\#UNACC} \cdot 100 \end{aligned} \tag{4.8}$$

Analogous definition can be given for false positives:

$$\begin{aligned} &FP_C = FP_C(NL, THR) \equiv (C(NL, THR) = True) \wedge (record\ annotated\ ACC) \\ &FPRc \equiv \frac{\#FP_C}{\#ACC} \cdot 100 \end{aligned} \tag{4.9}$$

The search for the optimal threshold THR and number of leads NL in which the condition must be satisfied in order to classify the recording as ‘unacceptable’ can be seen as a bi-dimensional optimization problem, where the goal is to maximize sensitivity (TPR_C), setting an upper bound of 1% for false positive rate (FPR_C):

$$(NL, THR)_{OPT} \equiv \arg\max \left\{ TPR_C(NL, THR) : FPR_C(NL, THR) \leq 1\% \right\} \tag{4.10}$$

The range for the two independent variables (THR_C, NL) is defined heuristically: NL=1,…,12; THR_C=min(F_j),…, max(F_j), where F_j is the feature under consideration for the given condition, and min(F_j), max(F_j) are calculated across all leads, across all records in training set.

4.3.2.5 Supervised learning training set

For each supervised-learning method, the classifier was trained on a subset of TSA containing $M/2$ recordings (M=200, 400) randomly drawn from the ‘Acceptable’ set, and $M/2$

recordings from the ‘Unacceptable’ set. The choice of balanced training was made to compensate the substantial difference in size of the two groups of records in TSA: 773 ‘Acceptable’ and only 225 ‘Unacceptable’ records. The disadvantage of this choice is a sub-optimal fit of the classifier on the full data set, while the advantage is a stricter test of the generalization ability of the classifier.

4.3.3 Supervised-learning classifiers

Two supervised-learning classification (SLC) methods suitable for binary classification problems were considered for comparison with the proposed algorithm: k-nearest neighbor (KNN) and probabilistic neural network (PNN).

For KNN, the Euclidean distance metrics was adopted, the number of nearest neighbors was set to one (K=1), and the “majority rule” was used for classification (i.e. a sample point was assigned to the class the majority of the K nearest neighbors were from).

PNN consisted in a 2-layer feed-forward neural network with a radial basis hidden layer and a competition layer yielding a N_Ox1 output vector (N_O=2 for binary classification), where the only element set to ‘1’ (the others set to ‘0’) indicated the class the input most probably belongs to.

For each classifier, the feature space size was given by the number of leads (twelve) multiplied by the number of individual lead features (five). For the two SLCs, principal component analysis (PCA) was applied to reduce the feature space dimension. To compute PCA, the features (i.e. input variables) were preliminarily standardized (zero-meaned and normalized to standard deviation) to compensate the magnitude difference between variables. The number of principal components (PCs) to be used for classification was chosen such that the cumulative variance would be grater or equal to 95%. Accuracy of the SLC algorithms for full and reduced (through PCA) feature space dimension were calculated and compared to the accuracy of the SCDR algorithm.

4.4 Results

4.4.1 Optimal thresholds

Table 4.2 summarizes the optimal thresholds that were identified for each condition. For each threshold (condition), TPR and FPR are calculated considering the given condition as the only one used for classification. As a corollary of (4.10), FPR ≤ 1% for all thresholds.

4.4.2 Classification accuracy

Table 4.3 compares the performance of the three methods (SCDR and two SLCs) on the test sets XS_1, XS_2 after being trained on TS_1, TS_2, respectively. The score (Sc) is the accuracy defined as the percentage of correct classifications. For the supervised learning classifiers

(KN, PNN), the performance after PCA-based reduction of the feature set is also reported. Only a slight reduction in accuracy is visible in spite of a considerable reduction of the input parameter space: from 12x5 to the number of principal components (#PCs) required to account for 95% of cumulative variance (#PCs was 13 for TS_1, 16 for TS_2).

Table 4.2 – Individual Conditions Performance for selected thresholds on training sets

Training Set	Feature	Condition	Threshold Value	#leads [(a)]	TPR [%]	FPR [%]
TS_1	F_1	C_1	5.0 V^2	1	71.0	1.0
	F_2	C_2	4.0 V^2	1	26.0	1.0
	F_3	C_3	0.1 V^2	1	26.0	1.0
	F_4	$C_{4\text{-}A}$	-23 dB	1	29.0	1.0
		$C_{4\text{-}B}$	-72 dB	1	61.0	1.0
	F_5	C_5	0.1 mV	1	65.0	1.0
TS_2	F_1	C_1	2.0 V^2	2	45.5	0.3
	F_2	C_2	1.0 V^2	2	16.1	0.3
	F_3	C_3	1.3 V^2	1	13.4	0.8
	F_4	$C_{4\text{-}A}$	-25 dB	1	35.7	0.8
		$C_{4\text{-}B}$	-76 dB	1	44.6	0.8
	F_5	C_5	0.1 mV	2	49.1	0.0

[(a)] Number of leads for which the condition must be satisfied, in order to classify the record as 'unacceptable' on the ground of that condition'

Table 4.3 – Comparison of Performance of SCDR vs. Supervised Learning Classifiers

Training / Test Set	Method	#FN	#FP	Score [%]
TS_1 / XS_1	SCDR	17	44	92.36
	KNN	27	90	85.34
	KNN-PCA[(a)]	29	97	84.21
	PNN	57	79	82.96
	PNN-PCA[(a)]	52	89	82.33
TS_2 / XS_2	SCDR	21	12	93.40
	KNN	29	10	92.20
	KNN-PCA[(b)]	30	19	90.20
	PNN	55	8	87.35
	PNN-PCA[(b)]	51	16	86.55

[(a)] #PCs=13 (accounting for 95% cumulative variance)

[(b)] #PCs=16 (accounting for 95% cumulative variance)

FN: false negative. FP: false positive. TS_1: training set 1; TS_2: training set 2. SCDR: single condition decision rule algorithm; KNN: K-nearest neighbor; KNN-PCA: KNN with principal component analysis; PNN: probabilistic neural network; PNN-PCA: PNN with principal component analysis.

4.4.3 Examples

In this section, examples of processing output are presented for the SCDR algorithm using the thresholds defined for TS_2.

In Figure 4.3 an example of good quality ECG signal is shown, together with the time marginal distribution (panels in central row) from which features F_1 (left), F_2 (middle), F_3 (right) are calculated (as peak value), respectively. It can be seen that all three features are well below the respective threshold (Table 4.2). QRS amplitude is satisfactory, being greater than the 0.1 mV threshold. The bottom panel shows the normalized (with respect to the peak value) frequency marginal in logarithmic scale.

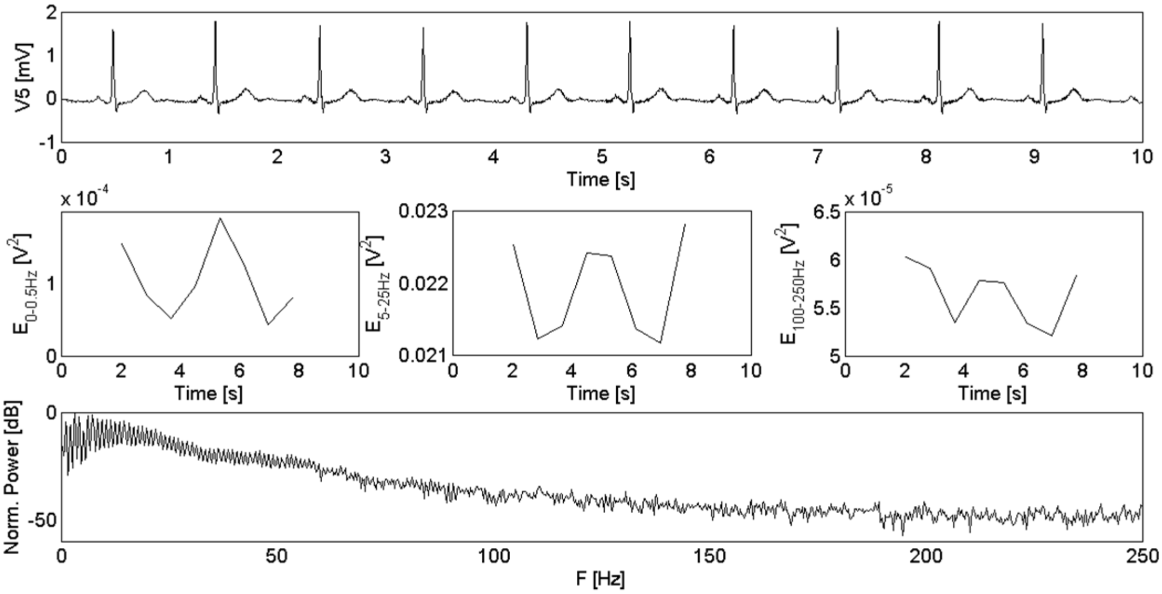

Figure 4.3 Raw ECG signal (top panel) from ‘acceptable’ record #1005639, time marginals (central row) from which F_1, F_2, F_3 (left to right) are calculated: LF energy in 0-0.5 Hz (left), QRS-band energy in 5-25 Hz (middle), HF energy in 100-250 Hz (right), and frequency marginal (bottom row) from which F_4 is calculated.

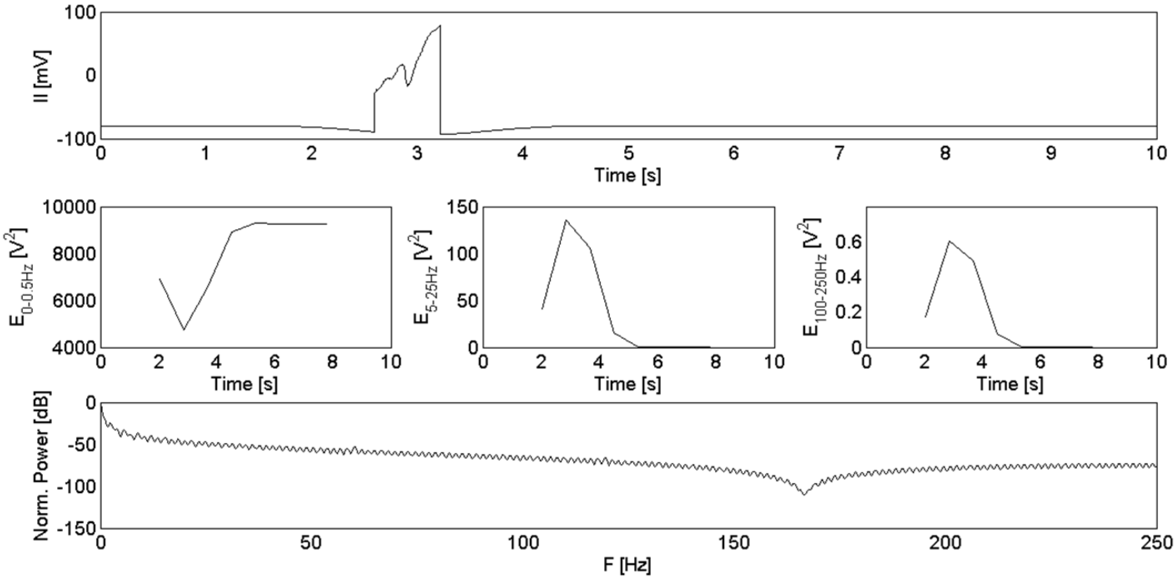

Figure 4.4 Raw ECG signal (top panel) from ‘unacceptable’ record #1030943, time marginals (central row) from which F_1, F_2, F_3 (left to right) are calculated: LF energy in 0-0.5 Hz (left), QRS-band energy in 5-25 Hz (middle), HF energy in 100-250 Hz (right), and frequency marginal (bottom row) from which F_4 is calculated.

In Figure 4.4 an example of ‘unacceptable’ ECG signal is shown. It can be seen that the peak value of LF energy, QRS-band energy (features F_1 and F_2, respectively) are above threshold (Table 4.2), indicating the concurrent presence of “flat line” and QRS artifact (presence of in-band noise in QRS band).

From the bottom panel - showing normalized frequency marginal (power) - it can be seen that VHF power (F_4) attenuation (tested in condition $C_{4\text{-}B}$) is above threshold, indicating the presence of saturation (step-wise amplitude changes). The record is correctly marked ‘unacceptable’.

Figure 4.5 shows an example of very noisy ECG signal. It can be seen that the time marginal energy (central row of panels) is below threshold (Table 4.2) for all three features F_1, F_2, F_3 (left to right panels). However, VHF power attenuation is above threshold (condition $C_{4\text{-}A}$ is met) indicating the presence of “non-ECG” noise (e.g. white noise).

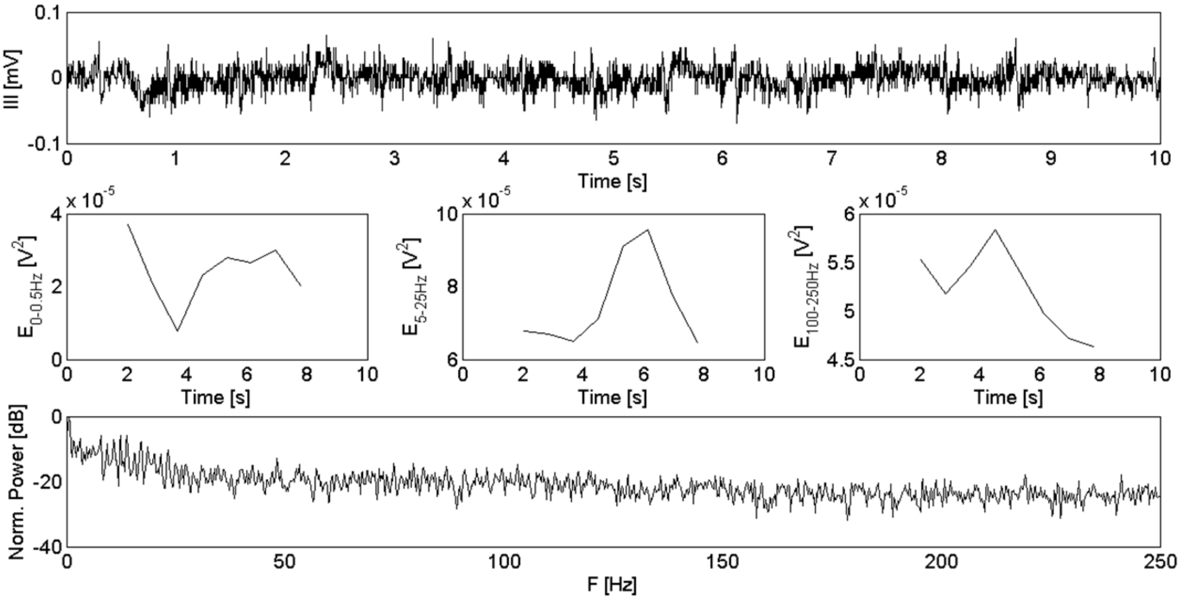

Figure 4.5 Raw ECG signal (top panel) from ‘unacceptable’ record #1101829, time marginals (central row) from which F_1, F_2, F_3 (left to right) are calculated: LF energy in 0-0.5 Hz (left), QRS-band energy in 5-25 Hz (middle), HF energy in 100-250 Hz (right), and frequency marginal (bottom row) from which F_4 is calculated. Condition $C_{4\text{-}A}$ is met.

The record is correctly marked ‘unacceptable’. It shall be noted that condition C_5 (low QRS amplitude) is also met for lead III shown in this figure; however, as shown in Table 4.2, condition C_5 must be satisfied at least in two leads for the record to be rejected on the basis of this condition).

Figure 4.6 shows an example of poor quality ECG signal. It can be seen that the time marginal energy (central row of panels) is above threshold (Table 4.2) for F_1 (left) and F_2 (middle) indicating the presence of baseline drift and QRS artifact (noise in QRS band). In the bottom panel, isolated peaks at 60 Hz and higher harmonics are visible, indicating the presence of mains interference.

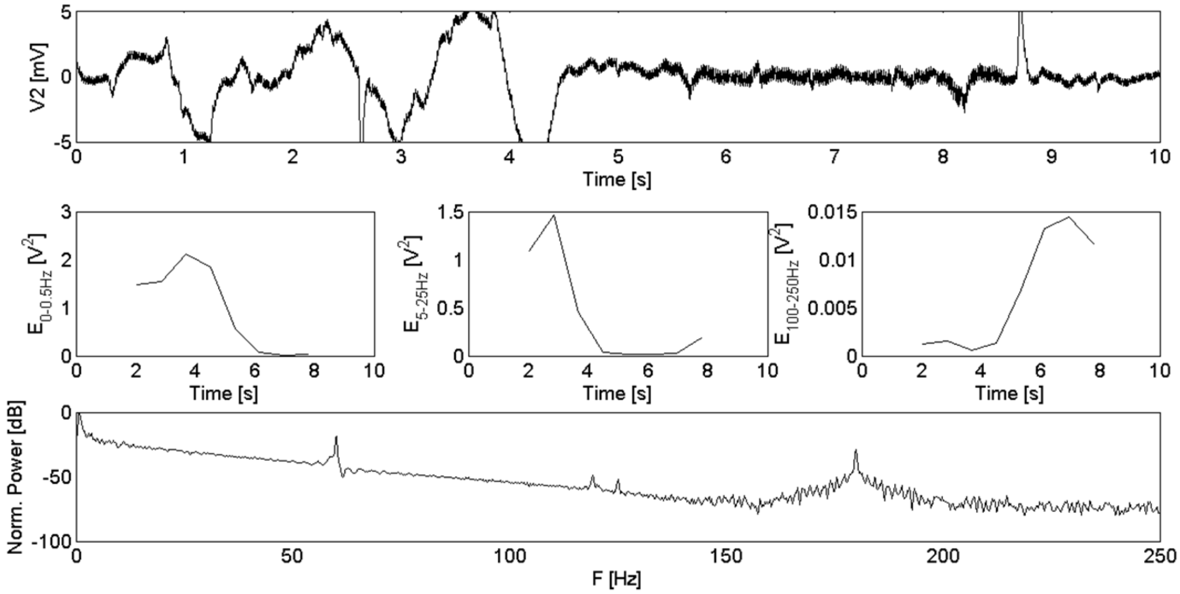

Figure 4.6 Raw ECG signal (top panel) from ‘unacceptable’ record #1105115, time marginals (central row) from which F_1, F_2, F_3 (left to right) are calculated: LF energy in 0-0.5 Hz (left), QRS-band energy in 5-25 Hz (middle), HF energy in 100-250 Hz (right), and frequency marginal (bottom row) from which F_4 is calculated.

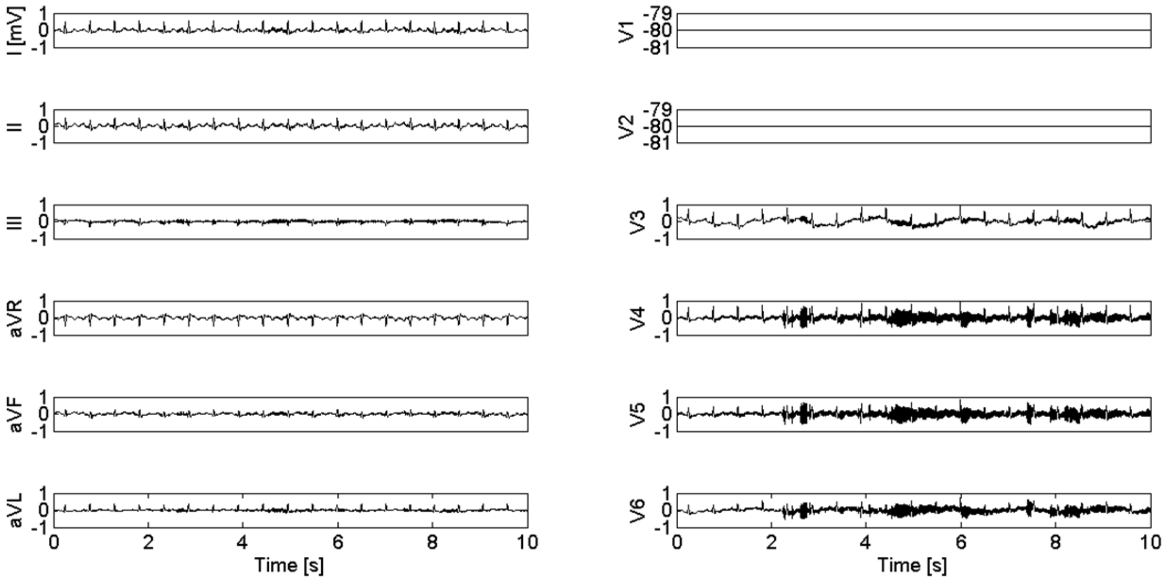

Figure 4.7 Example of “unacceptable” record (#1034914) correctly classified by the algorithm. Flat line (condition C_1) is present in V1, V2 (constant amplitude of -80 mV), “non-ECG” noise (condition $C_{4\text{-}A}$) in V4, V5).

Figure 4.7 shows an example of ‘unacceptable’ record correctly classified by the algorithm, which indicates flat line (condition C_1 met in V1, V2), “non-ECG” noise (condition $C_{4\text{-}A}$ met in V4, V5), and saturation (condition $C_{4\text{-}B}$ met in V1, V2).

Figure 4.8 shows an example of ‘acceptable’ record erroneously classified as ‘unacceptable’ (false positive) by the algorithm, which indicates flat line (condition C1 met in V4, V5) and saturation (condition $C_{4\text{-}B}$ met in V4).

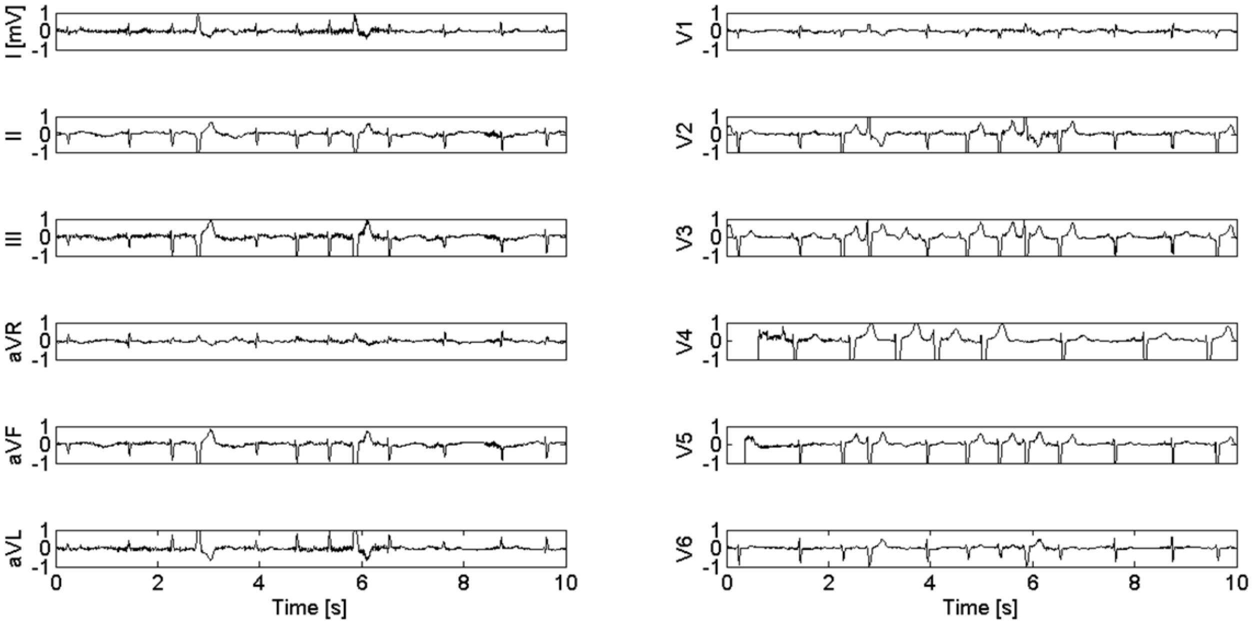

Figure 4.8 Example of “acceptable” record (#1548723) erroneously classified as “unacceptable” by the algorithm due to saturation (step-wise changes) (condition $C_{4\text{-}B}$ in V4).

4.5 Discussion

In this study an algorithm for automatic classification of ECG quality in short 12-leads ECG ambulatory recordings was presented. Based on preliminary processing (pacemaker filtering, beat detection and QRS amplitude detection), and extraction from JTF analysis of fundamental parameters for signal quality assessment (baseline drift, constant amplitude (flat line), noise in QRS band, spurious spikes, “non-ECG” noise (white noise), saturation (step-wise amplitude changes)), an adequate set of features was defined and used for classification.

Two supervised-learning classifiers (based on k-nearest neighbor and probabilistic neural network), and a single-condition decision rule classifier were implemented to classify ECG recording quality as either ‘acceptable’ or ‘unacceptable’ for diagnostic interpretation. Their performance was assessed on a standard database containing 998 ambulatory ECG recordings (Physionet Challenge 2011, Test Set A) from which two random training sets (balanced, and unbalanced) were extracted and the remaining records used as test set.

SCDR showed higher accuracy than KNN (which exhibited the best performance of the two SLCs) both in test set XS_1 (Sc(SCDR)=92.36% vs. Sc(KNN)=85.34%) and SX_2 (Sc(SCDR)=93.40% vs. Sc(KNN)=92.20%). As expected, the performance of SLCs increased with increasing training set size (at the cost of increased complexity of the classifier). On the other hand, reduction of the feature space dimension by PCA showed moderate SLC performance decrease in spite of a substantial reduction of space dimension (form 60 to 13 in TS_1, to 16 in TS_2). However, in spite of a larger feature space dimension, SCDR offers the advantage of combining higher performance to the ability to provide additional information to the classification output (i.e. reason for rejection). Due to the flexible structure of the algorithm, new features could also be added to improve detection of

ECG contaminants, as well as “quality warnings” (e..g. conditions C_1,..,C_5 close to being met (features close to threshold); mains interference detection by power peaks at characteristic frequencies (Figure 4.6)). On the other hand, SLC classifiers suffer from lack of physical interpretability of the model (weight coefficients of the radial basis layer in PNN; neighbor points in KNN).

SCRD is based on heuristic rules, exploiting established and simple processing methods. The joint time-frequency analysis is based on FFT computation which is widely available in high performance, low power-budget, digital signal processing (DSP) co-processors, as well as application programming interfaces (API).

Moreover, the JTF analysis used in this study offers the possibility to compute additional parameters to characterize the temporal evolution of the ECG signal. For instance, in addition to features indicating the energy of the given contaminant (baseline drift, step-wise amplitude changes etc.), it could also be detected “when” in time the given phenomenon occurs. This may be of interest for long recordings (such as in Holter monitoring) in which visual inspection of the data is prohibitive.

In conclusion, the single condition classifier proposed in this study, based on an intuitive and flexible scheme in which specific (and practical) conditions are tested individually, showed high accuracy in automatic classification of short 12-leads ambulatory ECG recordings, in spite of its simple logic. The ability to provide additional information (rejection reason) to the classification output, suggests the proposed method may be a useful tool in automatic quality assessment of 12-leads ambulatory ECG recordings.

References

Chaudhuri S, Pawar TD, Duttagupta S. Ambulation analysis in wearable ECG. Springer, 2009. pp. 5–7.

Clifford GD, Azuaje F, McSharry PE: *Advanced methods and tools for ECG data analysis* Ed. Artech House 2006; pp. 69–70.

Klug S, Krupka K, Dickhaus H, Katus HA, Hilbel T. Displaying computerized ECG recordings and vital signs on Windows Phone 7 smartphones. *Comput Cardiol* 2010;37:1067−1070

Langley P, Di Marco LY, King S, Di Maria C, Duan W, Bojarnejad M, Wang K, Zheng D, Allen J, Murray A. An algorithm for assessment of ECG quality acquired via mobile telephone. *Comput Cardiol* 2011; 38:281−284.

Pan J, Tompkins WJ. A real-time QRS detection algorithm. *IEEE Trans Biomed Eng* 1985;32(3): 230–236.

Romero I. PCA-based Noise Reduction in Ambulatory ECGs. *Comput Cardiol* 2010; 37:677-680.

Chapter 5: Design and implementation of a real-time polygraphic ambulatory monitor

5.1 Overview

This chapter presents the architecture of a real-time polygraphic ambulatory monitor designed for the acquisition and processing of cardiovascular and respiratory signals such as ECG, photoplethysmogram, respiratory effort, and skin conductance (galvanic skin response).

The architecture of the cardiovascular-respiratory (CVR) monitor is designed for the integration in a closed-loop system of adaptive man-machine interface (MMI), as shown in the block diagram of Figure 5.1.

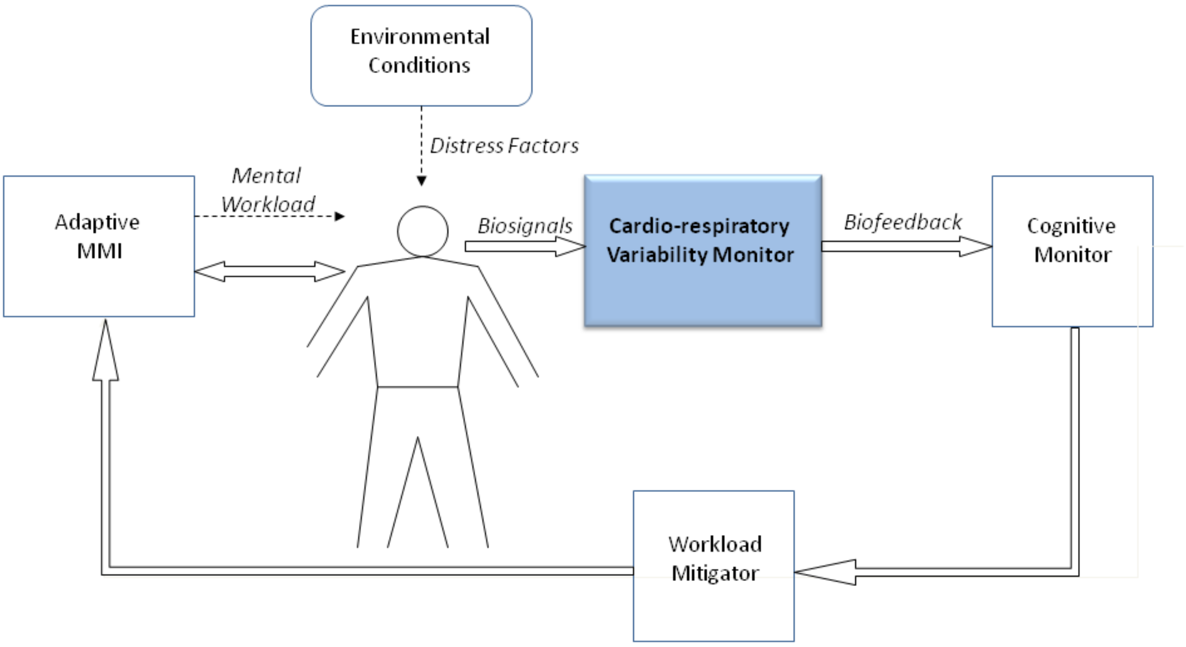

Figure 5.1 Adaptive MMI block diagram. The CVR monitor acquires and processes biosignals in real-time and feeds parameters (biofeedback) to the Cognitive Monitor, which classifies workload and sends its output to the Workload Mitigator, which selects the proper mitigation strategy for the adaptive MMI.

The CVR monitor generates a vector of synchronous parameters, with is updated at discrete time intervals. The output vector is fed (biofeedback) to the Cognitive Monitor, which integrates inputs from multiple devices (in the general case) and classifies the operator's mental workload. The output is fed to the Workload Mitigator sub-system which selects the proper mitigation strategy for the adaptive MMI.

The CVR monitor was developed as part of the "Cognitive adaptive man-machine interface" (CAMMI) project supported by ARTEMIS JTI initiative of the European Union, EU-JTI grant No. 100008.

5.2 Front-end device

For ambulatory monitoring of relevant physiological signals in a non-clinical setting, a commercial polygraphic front-end device was adopted. The multi-purpose ambulatory polygraph gMOBIlab+™ by g.tec® (g.tec medical engineering GmbH) was chosen among off-the-shelf solutions available on the market. The device acquires and transmits wirelessly the raw data in real-time, to a host computer (PC or laptop). Up to eight different physiological signals can be acquired simultaneously, at a sample rate of 256 samples/s, with 16-bit A/D conversion.

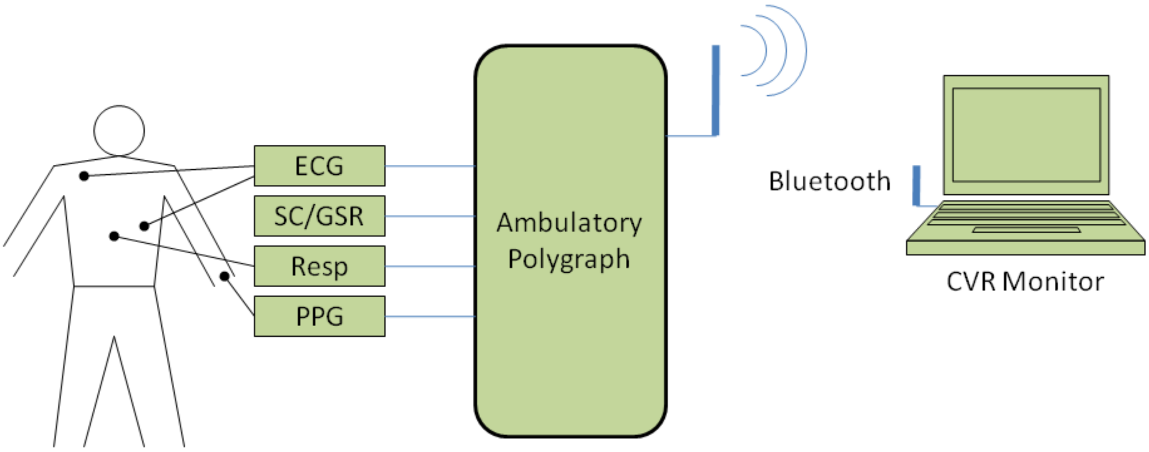

Figure 5.2 Scheme of signal acquisition in the ambulatory setting used in this work.

Preliminary tests on the full set of available signals, namely ECG, respiratory effort (by means of a strap-belt), finger and ear photoplethysmogram (PPG), galvanic skin response

(GSR), were carried out with the purpose of assessing signal quality in actual experimental settings. A schematic representation of the acquisition system is given in Figure 5.2. The front-end device is shown in Figure 5.3.

Figure 5.3 The front-end device: gMOBIlab+™ by g.tec® (g.tec medical engineering GmbH) with ECG/EMG patient cable. The device transfers the raw samples in real-time via Bluetooth to a host computer (PC or laptop).

5.3 Software architecture of the polygraphic monitor

The software architecture of the CVR monitor was designed in C++ Language (Microsoft Visual Studio 2008™), to run on a host PC or laptop, on a Windows XP Professional™ platform. A multithread structure was implemented for real-time acquisition and processing of the raw data stream. The acquisition thread fed the raw data to the processing thread by means of a buffered first-in-first-out queue.

The block diagram of the signal processing is illustrated in Figure 5.4.

The single lead ECG signal was processed for beat detection (QRS detection) by means of a modified version of the open source library developed by Hamilton (Hamilton, 2002) inspired by Pan and Tompkins (Pan and Tompkins, 1985), which was adapted to process the input data stream in real-time. The PPG signal was acquired at two different sites (earlobe and finger). It was processed for real-time pulse detection by means of a proprietary algorithm based on a maximum slope and adaptive threshold approach, as illustrated in Figure 5.5.

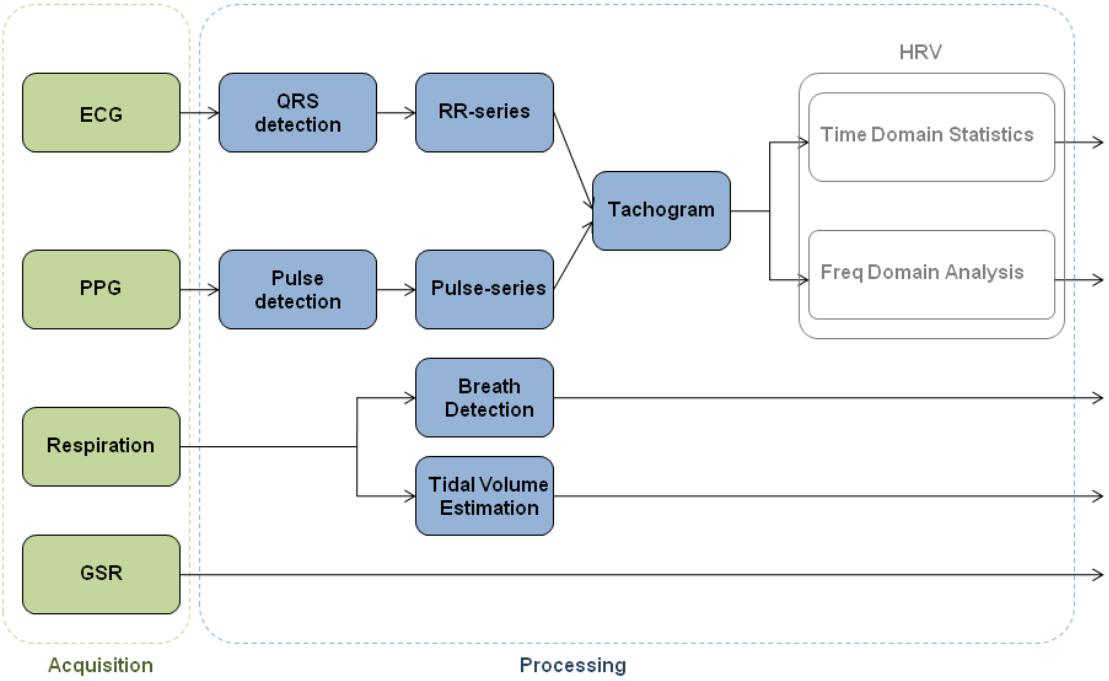

Figure 5.4 Scheme of signal processing flow in CVR monitor. ECG: electrocardiogram, PPG: photoplethysmogram, GSR: galvanic skin response.

The unevenly sampled tachogram of the RR-interval (pulse onset) time series of the ECG (PPG), was evenly resampled online by means of the algorithm proposed by Berger and coworkers (Berger *et al.*, 1986). Time domain statistical indices of HRV and frequency domain indices were computed according to the standards of measurement (Task Force of the European Society of Cardiology, 1996). In particular short term HRV was calculated over a sliding 5-min window. Indices SDNN, RMSSD, pNN50, mean RR, were computed in the time domain, and LF, HF, LF-HF ratio, in the frequency domain. HRV indices were updated every 10 s.

5.3.1 Real-time visualization

Figure 5.6 shows a screen shot of the CVR monitor's user-interface. In a dedicated rectangular screen area spanning approximately 8 s of data, the CVR monitor displayed the acquired signals (up to eight traces) in real-time, synchronously, at a custom sweep-speed of 32 mm/s. The traces were scaled vertically according to the respective amplitude resolution, to account for a physiological range. The vertical raster displayed the most recent data advancing left to right, and wrapped around at the end of the screen.

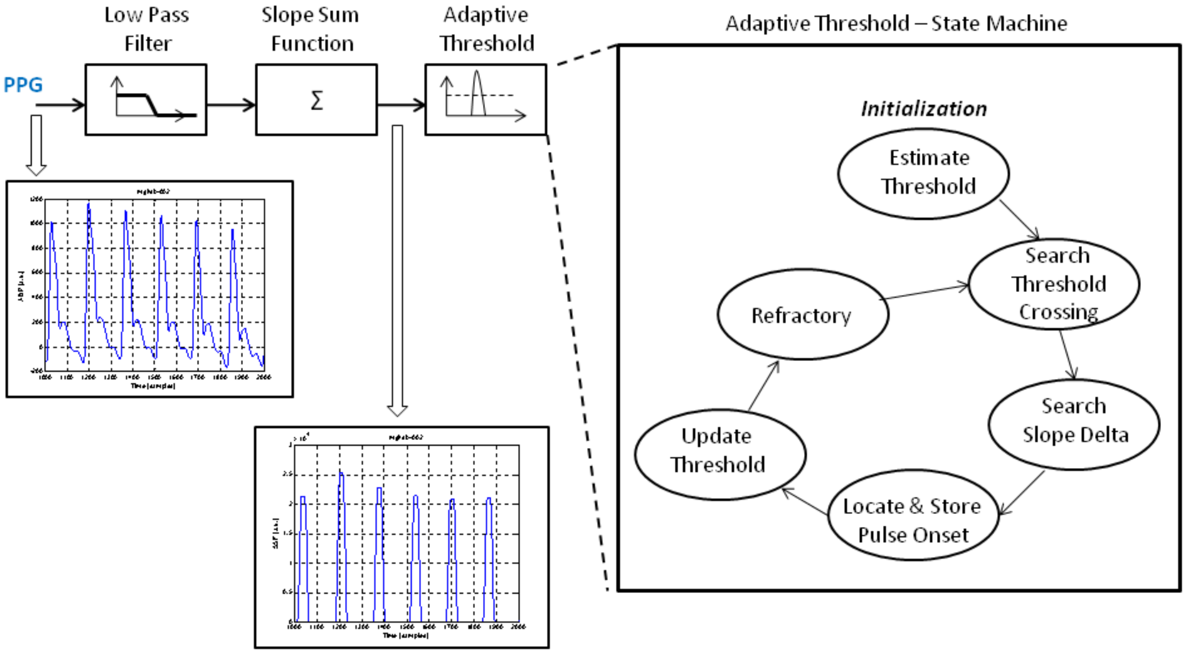

Figure 5.5 Photoplethysmogram (PPG) pulse detection algorithm: block diagram (left) with intermediate output samples (figure boxes), and state machine of adaptive threshold (right).

Below the traces area, a grid of read-only boxes displayed HRV indices, updated every 10 s, calculated over the most recent 5 min.

Beat (pulse) detection was computed and displayed for ECG (PPG). The beat detection library also computed beat classification, which was exploited for online detection of abnormal beats (e.g. premature supra-ventricular or ventricular contractions) and noisy signals causing misdetections (artifacts). Detected beats were marked in green (normal sinus rhythm) or red (abnormal beats).

5.3.2 Raw data export

The acquired raw data were stored to ASCII text files according to a custom defined protocol, in parallel to real-time processing. For those signals with fiducial points (i.e. R-wave time stamp in ECG, pulse-onset time stamp in PPG), the raw data were saved together with the (synchronized) time markers of the fiducial point.

This protocol allowed external access and processing of the raw data (e.g. MATLAB®, The Mathworks, Inc.) for algorithm validation purposes or further analysis, and preparation of scientific presentations.

5.3.3 Raw data replay

The raw data storage protocol also allowed re-playing of the data. The CVR monitor could run in “read from file” mode to re-acquire the data and process them. The scope separation semantics was implemented by multithreading. This feature was useful when the in the assessment of different real-time algorithms on the same data (or in debugging an existing algorithm).

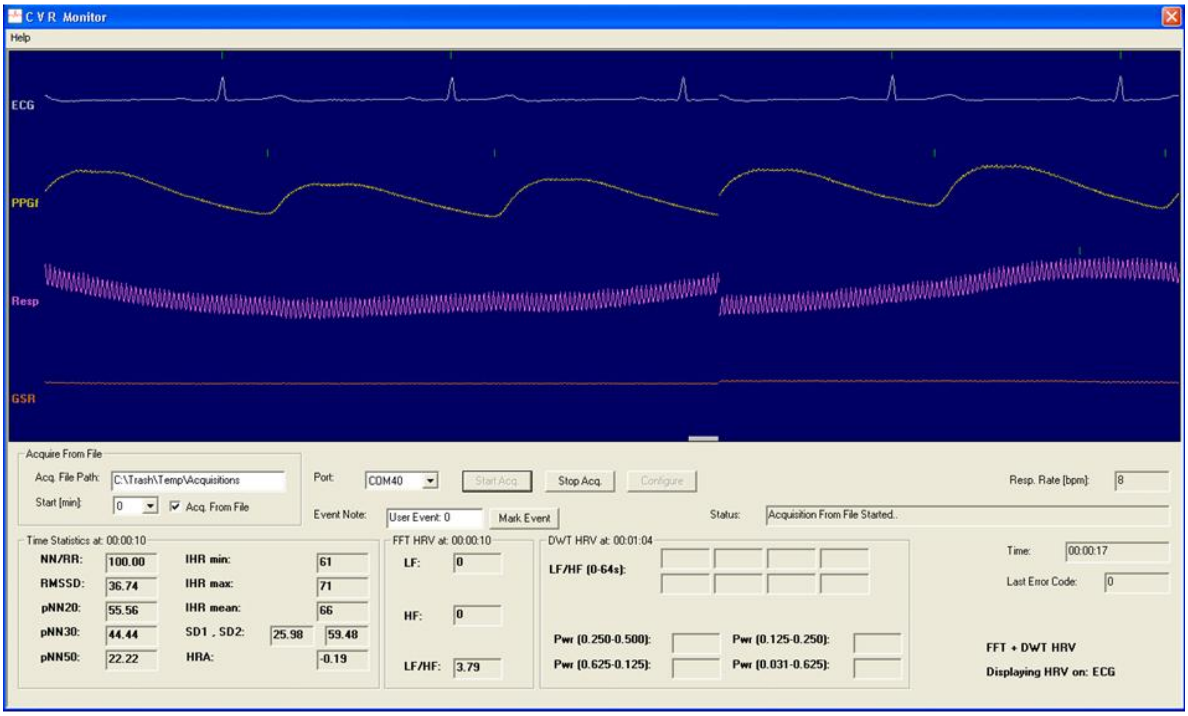

Acquire From File
Acq. File Path: C:\Trash\Temp\Acquisitions
Start [min]: 0
☑ Acq. From File
Port: COM40
Event Note: User Event: 0
Status: Acquisition From File Started..
Resp. Rate [bpm]: 8
Time: 00:00:17
Last Error Code: 0

Time Statistics at: 00:00:10
NN/RR: 100.00
RMSSD: 36.74
pNN20: 55.56
pNN30: 44.44
pNN50: 22.22
IHR min: 61
IHR max: 71
IHR mean: 66
SD1 , SD2: 25.98 59.48
HRA: -0.19

FFT HRV at: 00:00:10
LF: 0
HF: 0
LF/HF: 3.79

DWT HRV at: 00:01:04
LF/HF (0-64s):
Pwr (0.250-0.500):
Pwr (0.625-0.125):
Pwr (0.125-0.250):
Pwr (0.031-0.625):

Figure 5.6 Screen shot of CVR Monitor. ECG (silver), finger-PPG (yellow), Respiratory effort (pink), GSR (orange) traces are displayed. The parameter boxes show HRV indices (updated every 10 s, computed over the last 5 min). Marked power-line coupling (50 Hz) is visible on respiratory effort signal.

5.4 Integration in distributed architecture

The CVR monitor was designed for flexible integration into a closed-loop adaptive MMI architecture. Exploiting the features of multicast networking, which allow distributed processes to communicate in a platform-independent way, two different topologies were considered.

In the first topology (Figure 5.7) a single multicast channel for parameter vector transmission was implemented (Processed Data Multicast). Distributed processes (CVR monitor, Cognitive Monitor, Display, Data Storage) transmitted to or received from the multicast channel, independently of each other. A command channel was also available for processes synchronization. In this configuration, the CVR monitor was lumped in a single process.

In the second topology (Figure 5.8) the CVR monitor was distributed into separate processes, implementing acquisition (Acq DLL) and processing (Proc DLL) by means of the same libraries of the single process architecture shown in Figure 5.7. In this configuration the raw data was accessible to other processes.

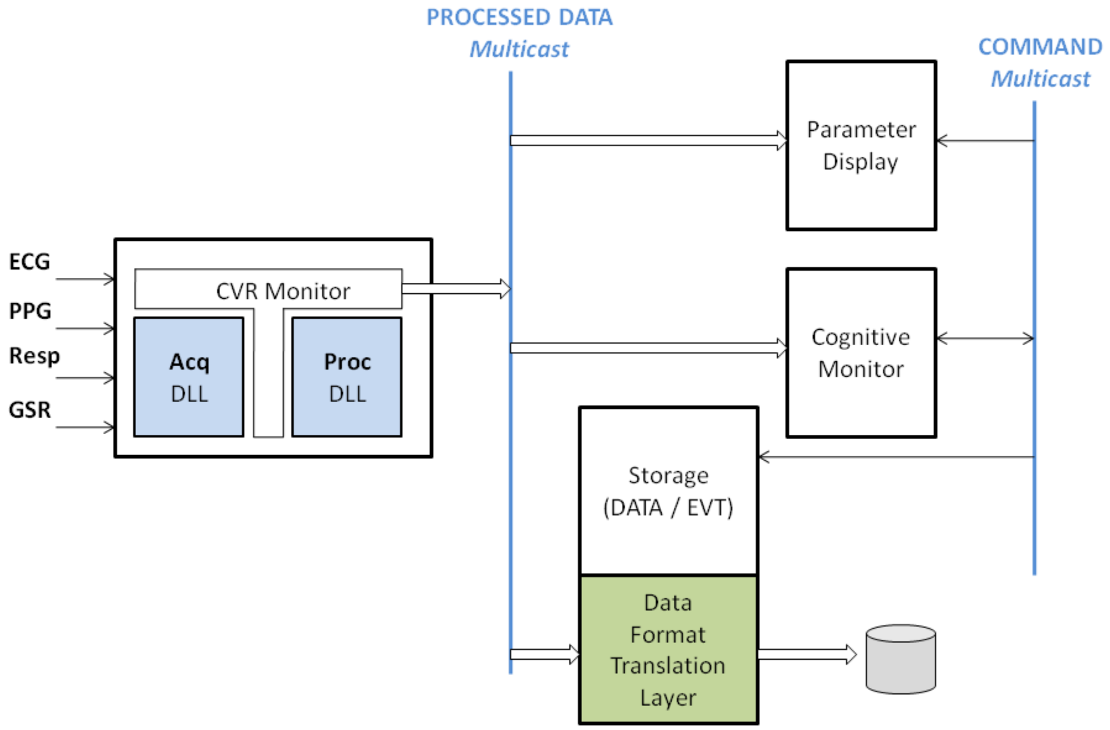

Figure 5.7 CVR monitor integration: distributed architecture over multicast network. The CVR monitor is lumped in a single process.

Figure 5.9 illustrates the formal protocol designed for multicast communication in the distributed processes architecture shown in Figure 5.8. The multicast packet consisted of a header which contained the channel identifier, the protocol version (for cross-version compatibility), the time stamp (for packet synchronization and sequencing) and an additional field indicating the number of samples (raw data multicast channel), the process identifier (processed data multicast channel), the command identifier (command multicast channel).

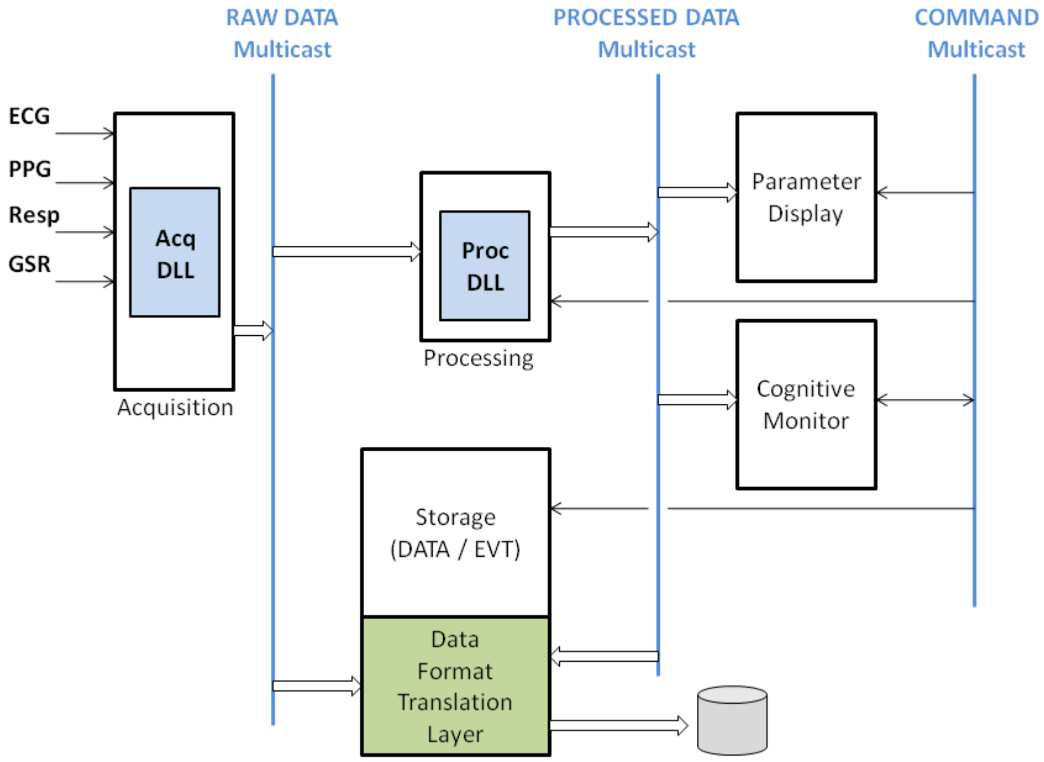

Figure 5.8 CVR monitor integration: distributed architecture over multicast network. The CVR monitor is distributed into separate processes (acquisition, processing), raw data are accessible to other processes.

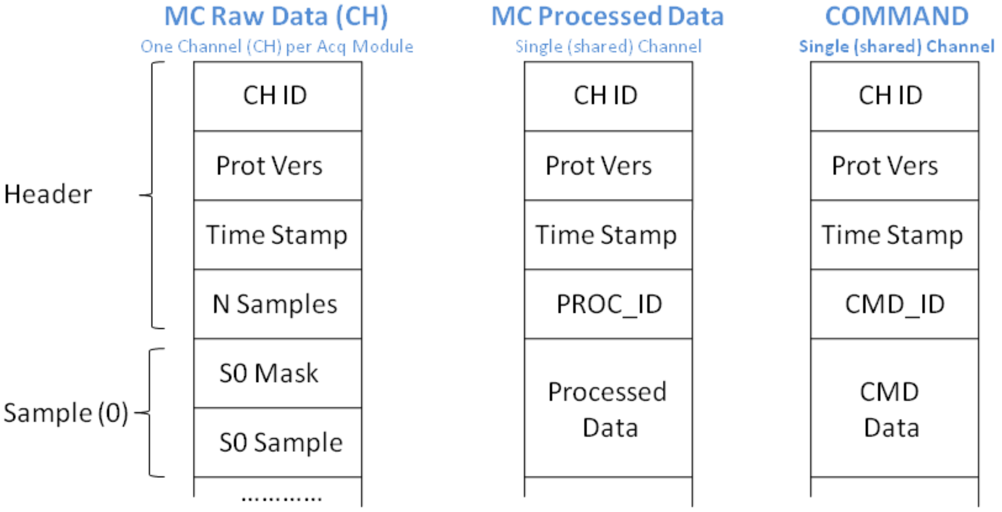

CH ID: Channel ID (validates data against unauthorized source and determines Sampling Rate, LSB)
Prot Vers: protocol version
Time Stamp: time marker of samples being piggybacked
S0 Mask: 8-bit mask (Lead Fail, Beat, Sync Start..)
S0 Sample: 16-bit sample (GTec)
PROC_ID: Processing Module ID (determines type/size of piggybacked data). E.g.: PROC_ID = PROC_HRV
CMD_ID: command ID (determines size of piggybacked data)

Figure 5.9 Multicast communication protocol designed for the distributed processes topology shown in Figure 5.8.

References

Berger RD, Akselrod S, Gordon D, Cohen RJ. An Efficient Algorithm for Spectral Analysis of Heart Rate Variability. *IEEE Trans Biomed Eng* 1986; 33(9):900–904.

Hamilton P: Open source ECG analysis. *Comput Cardiol* 2002; 29:101–104.

Pan J, Tompkins WJ. A real-time QRS detection algorithm. IEEE Trans Biomed Eng 1985;32(3): 230–236.

Press WH, Teukolsky SA, Vetterling WT, Flannery BP. Numerical Recipes 3rd Edition: The Art of Scientific Computing. Cambridge University Press 2007; pp.608–616, 652–666.

Task Force of the European Society of Cardiology and the North American Society of Pacing and Electrophysiology. Heart rate variability: standards of measurement, physiological interpretation and clinical use. *Circulation* 1996; 93:1043–1065.

Chapter 6: Time-frequency analysis of cardio-respiratory response to mental task execution

Abstract

Heart rate, heart rate variability (HRV), and respiratory effort have been proposed in numerous studies with the goal of correlating physiological parameters with mental workload.

Aim of this study was to analyze the cardio-respiratory response to a mental task (Sternberg Task) from a single lead ambulatory ECG recording, in healthy subjects. Under no assumptions on stationarity, HRV was analyzed in the time-frequency domain by means of the Hilbert-Huang Transform (HHT). A surrogate respiratory signal was also extracted from the ECG recording, by means of an established principal component analysis (PCA) based method, and its spectrum was analyzed.

A sharp decrease in low frequency (LF) components of HRV during the execution of the mental task with respect to the resting intervals was generally observed. In some subjects, an increase in the peak-power respiratory rate was also observed during task execution.

6.1 Introduction

Heart rate and heart rate variability (HRV) have been proposed in numerous studies (Nickel and Nachreiner, 2003; Takahashi, 2009) in neuroergonomics with the goal of detecting physiological parameters correlating with mental workload. Studies (Backs and Seljos, 1994; Kotani *et al.*, 2007) have also shown the role of the respiratory signal (breathing rate and depth) in characterizing the physiological response to mental workload.

To limit the obtrusiveness of measurements, the electrocardiogram (ECG) is recorded by means of a single lead ambulatory setup. Based on this assumption, aim of this study was to analyze the cardio-respiratory response to mental workload induced by Sternberg's high-speed memory scanning task (Sternberg, 1966), relying only on a single lead ECG recording.

In the analysis of mental workload, frequency domain parameters of HRV such as low frequency (LF: 0.04-0.15 Hz) power are generally used, though stationarity verification is often overlooked. In this study a time-frequency analysis of HRV requiring no assumptions on stationarity was adopted: the Hilbert-Huang Transform (HHT). Results were then compared with the power spectral density (PSD) estimate based on Welch periodogram.

A surrogate respiratory signal (SRS) was extracted from the ECG by means of the principal component analysis (PCA) based method proposed in (Langley *et al.*, 2010), and its spectrum was computed in the range 0-0.5 Hz for respiratory rate and power estimation.

6.2 Methods

6.2.1 Data acquisition

Fourteen healthy subjects, aged 29 ± 6, participated in this study. The experimental protocol was approved by the ethical committee of the Department of Electronics, Computer Science and Systems of the University of Bologna. All participants provided informed consent before undergoing the experiment.

The ECG was continuously recorded while subjects were sitting at the desk, performing four sessions of modified Sternberg memory-scanning task (Sternberg, 1966). Each session consisted in 90 trials. For each a memory set of digits was displayed on the screen for 1500 ms, followed by a screen blank of 500 ms after which a probe symbol would appear, prompting subjects to judge whether the symbol was part of the original set. Response timeout was set to 1500 ms.

Two difficulty levels were defined: easy, for memory sets of three items, difficult, for memory sets of eight items. Sessions were presented in the order: easy-difficult-difficult-easy, each one taking approximately 04:20 (mm:ss) and followed by a short rest. Recording duration was fixed (31:00) for all subjects, as well as the start time for the four sessions (03:00, 10:00, 17:00, 24:00).

The ECG was acquired from a modified lead two (MLII) single-lead setup. Data were acquired using g.Tec gMOBILab+ ™ . The ECG signal was sampled at 256 samples/s, 16 bits/sample, with an amplitude resolution of 0.19 µV. Reaction time and error rate were recorded for analysis.

6.2.2 Time-frequency HRV analysis

To assess HRV without introducing any assumptions on stationarity of the inter-beat interval series, HHT was used. Empirical mode decomposition (EMD) into intrinsic mode functions (IMF) was carried out according to (Huang *et al.*, 1998). The convergence criterion adopted for the j-th IMF was:

$$SD = \sum_{t=0}^{T} \frac{\left| h_{j(k-1)}(t) - h_{j(k)}(t) \right|^2}{h^2{}_{j(k-1)}(t)} \quad \leq \quad 0.1 \tag{6.1}$$

where T is the duration of the input time-series, hj(k) is the j-th IMF at the k-th iteration of the sifting process.

The evenly resampled inter-beat interval series (tachogram), can be expressed as:

$$x(t) = \sum_{j=0}^{n} h_j + r_n \tag{6.2}$$

where n is the number of empirical modes the input series is decomposed into, and rn is the residual, which can either be a mean trend or a constant.

After performing the Hilbert Transform on each IMF, the input series can be expressed as:

$$x(t) = \sum_{j=0}^{n} a_j(t) e^{i\int \omega_j(t)dt} \tag{6.3}$$

where a_j and ω_j are the instantaneous amplitude and frequency, respectively. The residual rn may be discarded (Huang *et al.*, 1998).

The expression in (6.3) may be interpreted as a generalized Fourier expansion, where amplitude and phase coefficients are time-varying.

The HHT amplitude spectrum was approximated in this study by evenly discretizing the instantaneous frequency and the time axes and by computing for each square of the grid the sum of the magnitude squared (energy spectrum) of all IMFs contributions. The discretization criterion can be summarized as:

$$E(i,j) = \sum_{k,\,\omega,\,t} \left| IMF_k(\omega,t) \right|^2 \tag{6.4}$$

where E(i,j) is the energy of the (i,j)-*th* element of the discretized time-frequency grid, IMF_k is the k-*th* IMF, and indices k, ω, t range in [1,n], $[f_j, f_j + \Delta F]$, $[t_i, t_i + \Delta T]$, respectively, while ΔT is the discrete time and ΔF the discrete frequency axis resolution.

The discrete approximation of the HHT marginal spectrum (HHT-MS) is derived from (6.4) by assigning the interval $[t_i, t_i + \Delta T]$ to a constant value.

6.2.3 Frequency domain HRV analysis

Traditional HRV spectral analysis was also carried out as per (Task Force of the European Society of Cardiology, 1996). Welch periodogram was used (arbitrarily) assuming wide sense stationarity of the input data. The inter-beat interval series was evenly resampled at 4 Hz. A 96 s sliding window with 50% overlap was used for computation of PSD of the tachogram. Only low (LF: 0.04-0.15 Hz) and high (HF: 0.15-0.40 Hz) frequency bands were considered for power computation.

6.2.4 Surrogate respiratory signal analysis

Beat detection on the raw ECG data was performed by means of the open-source algorithm proposed in (Hamilton, 2002).

The PCA-based method proposed in (Langley *et al.*, 2010) was then adopted for SRS extraction.

Preliminary low-pass filtering (6th order Butterworth, cut-off frequency of 35 Hz) on the ECG signal was performed to reduce the impact of muscular noise and power-line coupling which was empirically found to affect PCA results severely. Also accurate R-peak localization for each beat was performed. A window of 50 ms preceding the R peak and 60 ms following it was used, thus P and T wave were left out (only normal sinus rhythm beats were found in all recordings). SRS was extracted from the first principal component coefficient series (PC1) over a 96 s sliding window (as for HRV) by converting the beat index of each PC1 coefficient into the R-peak time of the corresponding beat. This unevenly sampled time series was evenly resampled at a sampling frequency of 4 Hz. Figure 6.1 shows an example of R-peak aligned beats for PCA computation and the extracted SRS.

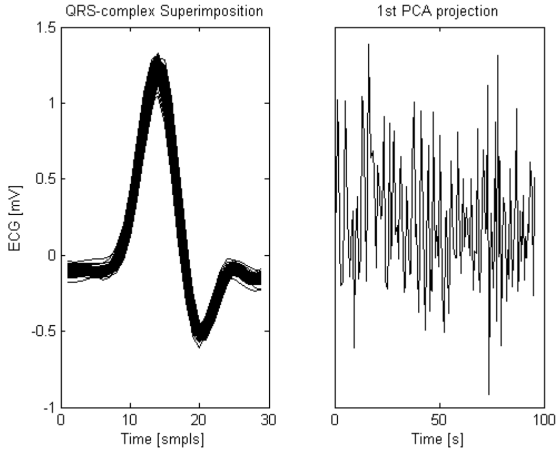

Figure 6.1 Superimposition of consecutive QRS complexes (left) and SRS extracted from PC1 coefficients (right).

6.3 Results

6.3.1 HRV

Regardless of the task difficulty level, a marked decrease of LF during task execution with respect to the resting intervals was observed in most subjects.

Figure 6.2 shows a typical PSD spectrum and the evolution of the corresponding LF, HF components of HRV. Figure 6.3 represents the HHT energy spectrum for the same subject.

In the Fourier representation, the existence of energy at a frequency ω means that a component persisted through the time span of the data, whereas in HHT the existence of energy at ω means only that, in the whole time span of the data, there is a higher likelihood for such wave to have appeared locally. In spite of this conceptual difference, normalized PSD-LF power and HHT-LF energy exhibit remarkably similar pattern over time, as shown in Figures 6.2 and 6.3.

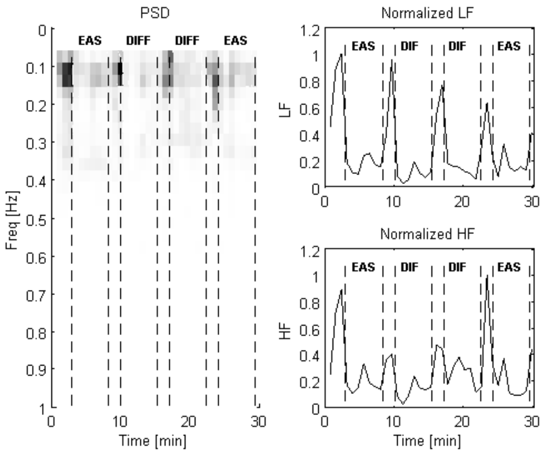

Figure 6.2 PSD computed over 96 s sliding window (left), and normalized LF, HF evolution (right). EAS=Easy task, DIFF=Difficult task.

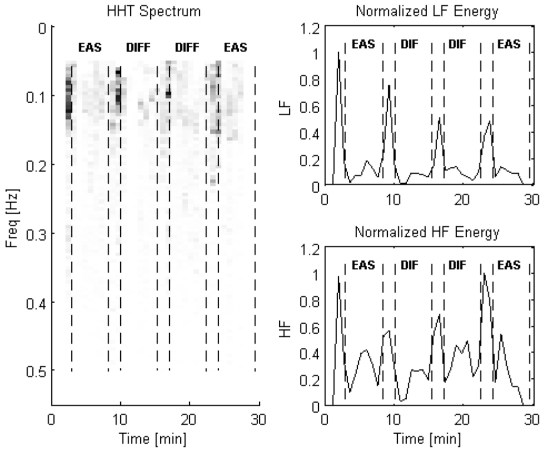

Figure 6.3 HHT energy spectrum computed over the entire recording (left), and normalized LF, HF energy evolution (right). EAS=Easy task, DIFF=Difficult task.

Table 6.1. PSD vs. HHT linear regression for LF and HF

	Normalized LF		Normalized HF	
Subject	r^2	RMSE	r^2	RMSE
S1	0.90	0.07	0.62	0.15
S2	0.69	0.13	0.46	0.14
S3	0.73	0.15	0.23	0.18
S4	0.44	0.17	0.48	0.16
S5	0.70	0.14	0.58	0.14
S6	0.38	0.17	0.54	0.17
S7	0.68	0.12	0.54	0.13
S8	0.79	0.10	0.82	0.10
S9	0.66	0.17	0.56	0.14
S10	0.42	0.17	0.62	0.10
S11	0.59	0.17	0.69	0.10
S12	0.37	0.18	0.91	0.05
S13	0.75	0.12	0.49	0.14
S14	0.74	0.12	0.15	0.18

Table 6.1 shows linear regression of PSD-LF and HHT-LF components and of PSD-HF and HHT-HF, for all 14 subjects.

6.3.1 Surrogate respiratory signal

Figure 6.4 shows PSD evolution over a 96s sliding window (50% overlap) for one subject.

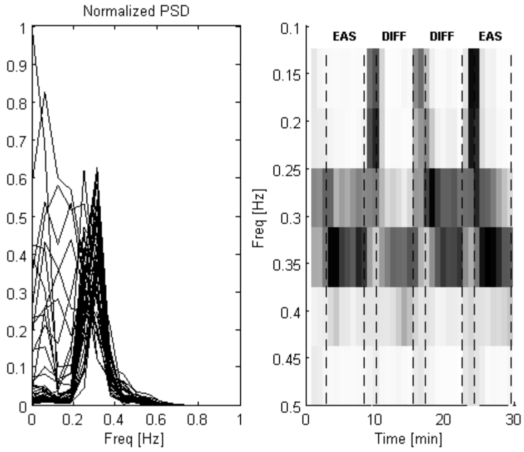

Figure 6.4 Overlapped PSD spectra of SRS, each one computed over a sliding 96 s window (left), and time-frequency PSD plot (right). EAS=Easy task, DIFF=Difficult task.

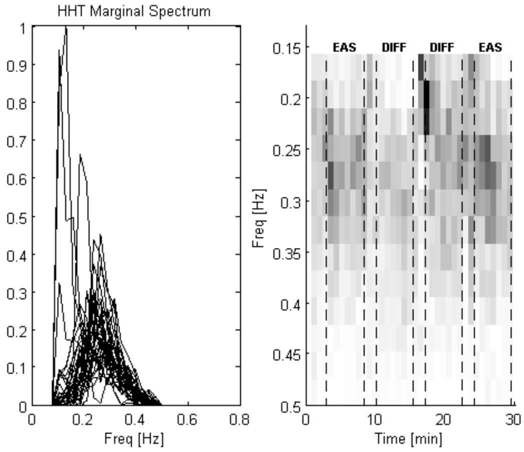

Figure 6.5 Overlapped HHT marginal energy spectra of SRS, each one computed over a sliding 96 s window (left), and HHT energy spectrum (right). EAS=Easy task, DIFF=Difficult task.

A dominant respiratory rate between 0.25 Hz and 0.35 Hz (15 rpm and 20 rpm, respectively) can be observed. In proximity of the start of the 2nd, 3rd and 4th task a transient lower frequency component (0.15-0.20 Hz) with higher power is also noticeable. Figure 6.5 shows HHT approach to the SRS of the same subject.

A large spread in respiratory rate can be observed and the low frequency-high power phenomenon is not evident except for the 3rd task start.

6.4 Discussion and conclusions

HRV and SRS from a single lead ambulatory ECG recording were analyzed with the goal of characterizing the cardio-respiratory response to a mental task in healthy subjects. A time-frequency approach was used for HRV analysis based on HHT, making no assumptions on inter-beat series stationarity. Results were then compared to traditional PSD-based frequency domain analysis. A sharp decrease in LF was found in most subjects during task execution with respect to the resting intervals, as shown in Figure 6.2 and 6.3. A remarkable correlation in PSD power and HHT energy time evolution was found for normalized LF in most subjects (r^2=0.63±0.17), as shown in Table 6.1. Normalized HF component showed slightly lower correlation (r^2=0.54±0.20). Average reaction time was significantly higher ($p<0.05$) for all subjects in the difficult tasks with respect to the easy, also error rate was higher. The difficulty level of the task could not be observed from LF evolution, except for one subject where the LF peak was higher for the two difficult tasks.

Respiratory rate and power were analyzed by means of SRS from an established PCA-based method. A frequency domain analysis based on PSD showed a dominant respiratory rate between 0.20 Hz and 0.35 Hz (12 rpm and 20 rpm, respectively) in most subjects, which in some cases was associated with a transient lower frequency component (0.15-0.20 Hz) with higher power in proximity of the task start, as shown in figure 6.4. HHT approach to the SRS was also adopted to account for non-stationarity in SRS. A large spread in respiratory rate was generally observed and the low frequency-high power phenomenon was not evident as in PSD approach, except in few cases. However, SRS frequency and time-frequency behavior was found sensitive to the PCA component choice, to R-peak alignment, to the time window of the ECG segments (i.e. the portion of the heart beat) considered for PCA, to muscular and power-line noise on the ECG signal, and perhaps to the subjective respiratory mechanics.

In conclusion, HRV analysis in the time-frequency domain and in the frequency domain lead to similar results in terms of normalized LF and HF components, the first being more evident and also the most relevant to the characterization of the cardio-respiratory response to a mental task in healthy subjects. On the other hand, SRS analysis requires further investigation as the results are potentially affected by numerous factors.

References

Backs RW, Seljos KA. Metabolic and cardiorespiratory measures of mental effort: the effects of level of difficulty in a working memory task. *Int J Psychophysiol* 1994; 16(1):57–68.

Hamilton P. Open source ECG analysis. *Comp Cardiol* 2002;29:101–104.

Huang, NE, *et al.* The Empirical Mode Decomposition and the Hilbert Spectrum for Nonlinear and Non-Stationary Time Series Analysis. *Proc R Soc Lond A* 1998; 454:903–995.

Kotani K, Takamasu K, Tachibana M. Respiratory-phase domain analysis of heart rate variability can accurately estimate cardiac vagal activity during a mental arithmetic task. *Methods Inf Med* 2007; 46(3):376–85.

Langley P, Bowers EJ, Murray A. Principal Component Analysis as a Tool for Analyzing Beat-to-Beat Changes in ECG Features: Application to ECG-Derived Respiration. *IEEE Trans Biomed Eng* 2010; 57(4): 821–829.

Nickel P, Nachreiner F. Sensitivity and diagnosticity of the 0.1-Hz component of heart rate variability as an indicator of mental workload. *Hum Factors* 2003; 45(4):575–90.

Sternberg S. High-speed scanning in human memory. *Science* 1966; 153(3736): 652–654.

Takahashi M. Heart rate variability in occupational health --a systematic review. *Ind Health* 2009; 47(6):589–602.

Task Force of the European Society of Cardiology and the North American Society of Pacing and Electrophysiology. Heart rate variability: standards of measurement, physiological interpretation and clinical use. *Circulation* 1996; 93:1043–1065.

Chapter 7: Regularity and joint time-frequency analyses of non stationary heart rate variability in the assessment of psycho-physiological workload induced by memory search task

Abstract

Short-term heart rate variability (HRV) has been proposed as qualitative indicator of psycho-physiological workload (PPW) in response to a mental task. Most specific HRV indices are computed from frequency-domain analysis, assuming weak-sense stationarity of the inter-beat interval (IBI) series.

The aim of this study was to investigate the contribution of regularity and joint time-frequency analyses of non-stationary IBI series, in the assessment of PPW induced by a high-speed memory scanning task, with the goal of discriminating task difficulty levels.

Instantaneous energy (IE) of the IBI series and its variance (IEV) were computed based on smoothed pseudo Wigner-Ville distribution, together with standard HRV indices. IBI series regularity was assessed by sample entropy (SampEn).

A single lead electrocardiogram was recorded from fourteen healthy subjects (age 29 ± 6) during rest (4 minutes) followed by four sessions (4:30 minutes each) of modified Sternberg's high-speed memory scanning task (SST) in the sequence: easy-difficult-difficult-easy.

Error rate was significantly different between easy and difficult tasks ($p<0.05$). SampEn discriminated between performance (task) and rest ($p<0.05$). Only IEV discriminated difficult tasks from other sessions (rest, easy tasks) ($p<0.05$). The results suggest superior ability of SampEn and IEV compared to standard HRV indices in discriminating difficulty level of SST.

7.1 Introduction

Heart rate variability (HRV) analysis is an established method (Task Force, 1996) for the assessment of the autonomic nervous system (ANS) regulation of the heart rhythm. Measures of HRV have been employed in numerous studies ranging from clinical investigations on autonomic function and cardiovascular risks, to psychophysiological research on mental workload and cognitive behavior (Berntson *et al.,* 1997; Task Force, 1996; Mathewson *et al.,* 2010; Mukherjee *et al.,* 2011; Mulder *et al.,* 2000). The non-invasive nature of HRV analysis has contributed to its application to research fields extending beyond clinical interest, making it a powerful tool for the assessment of the relationships between psychological and physiological processes.

In recent years, particular interest has been devoted to the assessment and quantification of psycho-physiological workload (PPW) associated to task performance in the work environment, with the goal of promoting safety and productivity (Henelius *et al.,* 2009; Hjortskov *et al.,* 2004).

HRV linear indices in the time-domain and frequency-domain have extensively been studied for the purpose. Power of HRV in the low frequency band (LF: 0.04-0.15 Hz) has been reported to reflect increasing mental effort in response to mental tasks involving working memory, such as mental arithmetic, memory search, and planning (Aasman *et al.,* 1987; Fairclough and Roberts, 2011; Mulder *et al.,* 2000; Redondo and Del Valle-Inclán, 1992), suggesting increasing attenuation of the baroreflex loop in response to increasing cognitive challenge induced by attention demand.

General studies on HRV, however, support the relevance of nonlinear analysis (Parlitz *et al.,* 2011; Pincus and Goldberger, 1994; Scumacher, 2004; Signorini *et al.*, 2011; Task Force, 1996) with the goal of quantifying complex dynamics in the multi-factorial regulation of the heart rhythm, which may not be described by linear analysis. To the best of our knowledge, to date only one study has been presented (Mukherjee *et al.,* 2011) on short term nonlinear analysis of HRV in mental effort assessment.

Moreover, traditional frequency-domain analysis of HRV employs Fourier-based, non-parametric estimation of power spectral density (PSD) of the inter-beat interval series (IBI series), which relies on the implicit assumption of data stationarity. To overcome this limitation, time-frequency techniques have been proposed (Choi and Williams, 1989; Cohen, 1989) and applied to the analysis of cardiovascular time series (Bailòn *et al.*, 2011a; Bailòn *et al.*, 2011b; Pola *et al.,* 1996), providing the ability to locate subtle transient fluctuations.

The aims of this study were to: *i*) assess wide-sense stationarity (WSS) of the inter-beat interval (IBI) series in response to a high-speed memory scanning task in healthy young subjects; *ii*) assess the contribution of time-domain regularity and joint time-frequency (JTF) analyses of IBI-series in discriminating between performance (task execution) and rest, as well as between easy and difficult tasks; *iii*) compare the proposed methods with standard HRV.

The memory search task employed in this study was a modified version of the well-known Sternberg’s secondary task (SST) (Sternberg, 1966).

7.2 Methods

7.2.1 Data Acquisition

Fourteen healthy subjects, aged 29 ± 6, participated in this study. The experimental protocol was approved by the ethical committee of the University of Bologna. All participants provided informed consent before undergoing the experiment.

The electrocardiogram (ECG) was continuously recorded while subjects were sitting at the desk, performing four sessions of the modified Sternberg memory-scanning task (Sternberg, 1966). Each session consisted in 90 trials. For each trial a memory set of *n* digits was displayed on the screen for 1500 ms, followed by a screen blank of 500 ms after which a probe symbol would appear for 1000 ms, prompting subjects to judge whether the symbol was part of the original set. Response timeout was set to 1500 ms following the probe's appearance.

Two difficulty levels were defined: easy, for memory sets of $n = 3$ digits; difficult, for memory sets of $n = 8$ digits. After a resting period (baseline) of 4 minutes (BL), tasks (T1,…, T4) were presented in the order: easy-difficult-difficult-easy, each one taking approximately 04:30 (mm:ss) and followed by a short rest. Recording duration was fixed (31:00) for all subjects, as well as the relative start time for the four tasks (04:00, 11:00, 18:00, 25:00).

A custom software application was used for the presentation of stimuli. It was run on an Intel® Core™ 2 Duo P8400 (2.26 GHz) laptop PC, equipped with GNU/Linux® OS. Stimuli were presented to the subjects on a 19" external monitor (output device). User response was recorded by an optical USB mouse, whose left- and right- buttons were mapped to match the "yes" and "no" responses, respectively (input device).

A single lead ECG signal in a modified lead two (MLII) setup was acquired using g.Tec gMOBILab+ ™. The pass-band of the ECG front-end was (0.5 – 100 Hz), the digitalized ECG was sampled at 256 samples/s, 16 bits/sample, with an amplitude resolution of 0.19 µV.

The ECG signal was processed off-line for beat detection and classification, by means of an established method (Hamilton, 2002). No abnormal (arrhythmic) beats were detected by the algorithm. The ECG signals were also visually inspected to verify that no abnormal beats were present.

Reaction time (RT), defined as the time interval between the presentation of the probe and the subject's response, and error rate (ER), defined as the percentage of incorrect and missing answers, were recorded for each trial, for all tasks.

7.2.2 Stationarity test

The weak-sense stationarity of the IBI series, namely the stability of the expected value and variance over time, was tested according to a criterion inspired by the one proposed for HRV analysis by Porta and coworkers (Porta *et al.*, 2004). Briefly, the IBI series of each session (BL, T1,…, T4) was considered individually. The first order trend was removed from the data. Assuming the generic session contained N_{BS} beats, N_{BS}-L+1 ordered sequences of L beats each could be constructed, such that $IBI_L(i) = (IBI(i), IBI(i+1), \ldots, IBI(i+L-1))$ was the generic sequence starting at the ith sample. Kolmogorov-Smirnov (KS) goodness-of-fit test was used to assess the normality of the distribution ($p<0.05$) of each sequence. If the null hypothesis was rejected, the data was log-transformed and the KS test repeated. If the null hypothesis was rejected again, the test was replaced by the Kruskal-Wallis rank-sum test (KW), with equal significance level (α=0.05). The number (N_N) of sequences satisfying the null hypothesis of normally distributed data was stored. If N_N was greater than a fixed threshold M, the null hypotheses of stable (i.e. not significantly varying over time) mean and variance were tested by the one-way analysis of variance (ANOVA) and the Bartlett's test, respectively; otherwise the KW and Levene test were used, respectively. In the first case, N_N ($>M$) sequences were used; in the second, all available sequences were used for statistical analysis. This choice differs from the implementation presented in previous works (Porta *et al.*, 2004; Magagnin *et al.*, 2011), where only M randomly selected sequences were used. In this study L=50, M=8 were used, as in (Porta *et al.*, 2004; Magagnin *et al.*, 2011). For each session of each recording, the WSS condition was assessed.

7.2.3 Time-domain HRV analysis

The standard time-domain statistical indices of HRV were computed: mean-IBI, standard deviation of normal-to-normal intervals (SDNN), square root of the mean squared differences of successive normal-to-normal intervals (RMSSD). Established nonlinear indices from the Poincaré phase-space plot were also computed, namely the standard deviation of the width-histogram (SD1) and the standard deviation of the length-histogram (SD2), quantifying short-term and long-term variability of the IBI series, respectively. Sample entropy (SampEn) was calculated for nonlinear analysis of data regularity.

SampEn quantifies the degree of complexity of the IBI series (Richman and Moorman, 2000). For the calculation of SampEn, the original time series $IBI(i)$, $i = 1,\ldots, N$, is considered and vector sequences of size m, $\boldsymbol{u}(1)$ through $\boldsymbol{u}(N-m+1)$, defined by $\boldsymbol{u}(i) = \{IBI(i),\ldots, IBI(i+m-1)\}$ are constructed. The vectors length m, is known as the *embedding dimension*. The constructed vectors represent m consecutive IBIs starting from the ith point. The distance $d[\boldsymbol{u}(i), \boldsymbol{u}(j)]$ between vectors $\boldsymbol{u}(i)$ and $\boldsymbol{u}(j)$ is defined as $d[\boldsymbol{u}(i), \boldsymbol{u}(j)] = \max\{|\boldsymbol{u}(i + k) - \boldsymbol{u}(j + k)|, 0 \le k \le m - 1\}$. The probability of finding another vector within distance r from the template vector $\boldsymbol{u}(i)$ is estimated by: $C^m{}_i(r)$ = {number of $j \neq i$, $j \le N\text{-}m+1$, such that $d[\boldsymbol{u}(i), \boldsymbol{u}(j)] \le r\}/(N\text{-}m+1)$. Defining:

$$\phi^m(r) = (N - m + 1)^{-1} \sum_{i=1}^{N-m+1} C_i^m(r) \tag{7.1}$$

as the average probability, sample entropy can be written as:

$$SampEn(m, r, N) = -\ln[\phi^m(r) / \phi^{m+1}(r)] \tag{7.2}$$

Generally, the higher is the value of SampEn, the higher is the complexity (or irregularity) of the data series (RR-interval series).

7.2.4 Frequency-domain HRV analysis

Welch periodogram was used (arbitrarily) assuming wide sense stationarity of the input data. The IBI series was evenly resampled by cubic spline interpolation, at 4 Hz. Power spectral density (PSD) was estimated by Welch periodogram for each session separately: BL, T1,.., T4. Low frequency (LF) power (P_{LF}: 0.04-0.15 Hz), high frequency (HF) power (P_{HF}) in the frequency band between the standard lower bound (0.15 Hz) and half the average heart rate (i.e. the highest frequency with physiological meaning) as in (Bailòn *et al.* 2011b),

P_{LF}/P_{HF} ratio, and total power in the low and high frequency bands combined together (P_{LF+HF}) were computed from the estimated PSD.

7.2.5 Time-frequency HRV analysis

To assess HRV without assuming stationarity of the IBI series, an established well recognized method (Bailòn *et al.*, 2011a; Bailòn *et al.*, 2011b ; Jasson *et al.*, 1997; Pola *et al.*, 1996) based on the smoothed pseudo Wigner-Ville distribution (SPWVD) was used. SPWVD is a member of the Cohen's class of time-frequency joint distributions (Cohen, 1989). For a band-limited discrete-time real valued signal $x(n)$ whose analytic signal is expressed as: $z(n) = x(n) + jH[x(n)]$, where $H[]$ is the Hilbert transform operator, SPWVD can be computed as:

$$W_z(n,m) = 2\sum_{k=-K+1}^{K-1} |h(k)|^2 \left[\sum_{q=-N+1}^{N-1} g(q)\, z(n+q+k) z^*(n+q-k) \right] e^{-j2\pi \frac{m}{M} k} \tag{7.3}$$

where $|h(k)|^2$ and $g(q)$ are the frequency- and time- smoothing windows, of length $2K$-1 and $2N$-1, respectively; n is the discrete time instant, m/M is the discrete normalized frequency, $m = -M+1, ..., M$. In actual implementations, the smoothing windows shapes are chosen empirically as trade-off values between conflicting requirements, mainly concerning the so-called "cross terms" consisting in undesirable frequency components generated by the autocorrelation product in (3). In the present study, a rectangular frequency-smoothing window (K=32) was used. The time-smoothing window was chosen according to (Bailòn *et al.*, 2011a), namely an exponential window (N=21) with damping factor γ=1/64 samples^{-1}. The signal $x(n)$ is the evenly resampled (4 Hz) IBI series. By definition, the analytic signal $z(n)$ preserves the spectral content of the original signal $x(n)$ (Choi and Williams, 1989; Pola *et al.*, 1996), hence W_z represents the energy distribution, with respect to time and frequency, of the IBI series.

The instantaneous energy in the LF band (IE_{LF}) at time instant n was calculated according to (Bailòn *et al.*, 2011a; Bailòn *et al.*, 2011b) as:

$$IE_{LF}(n) = \sum_{m=m_1}^{m_2} W_z(n,m) \tag{7.4}$$

where m_1, m_2 are the discrete frequency indices corresponding to the lower (0.04 Hz) and upper (0.15 Hz) boundaries of the LF frequency band. In a similar way the instantaneous energy in the HF band (IE_{HF}) was computed. In this study the HF band was assumed to range between 0.15 Hz and half the mean heart rate.

The total power in the frequency band spanning LF and HF (IE_{LF+HF}) representing a measure of the total short-term variability was computed by summing IE_{LF} and IE_{HF} computed by (7.4).

For each session (BL, T1,...,T4) the instantaneous energy variability (IEV) was calculated as variance of the instantaneous energy in the given frequency band: e.g. for the LF band $IEV_{LF} = Var(IE_{LF})$. Similarly, the mean instantaneous energy (IEM) was calculated, for each session, in the frequency bands of interest.

7.2.6 Statistical analysis

The null hypothesis of normally distributed data was tested according to the Lilliefors test, with a significance level of 0.05. If the null hypothesis was rejected, the data distribution was log-transformed and the normality test repeated. Subsequently, analysis of variance (ANOVA) was performed on all parameters individually.

Post-hoc analysis for multiple comparisons was then performed according to Tukey-Kramer *honestly significant differences* (HSD) criterion, to determine significant differences among groups, with a significance level of 0.05.

The linear relationship between HRV parameters and RT is assessed by Pearson's correlation, with a significance level of 0.05.

7.3 Results

7.3.1 Sternberg Task

Analysis of variance of ER showed significant differences among groups ($p<0.001$). *Post hoc* analysis by TK test showed a significant difference (α=0.05) in ER between difficult (T2, T3) and easy (T1, T4) tasks. The results are summarized in Table 7.1. The reported *p* values refer to ANOVA, indicating confidence level in rejecting the null hypothesis of all sessions (BL, T1,…, T4) having the same mean.

Table 7.1 Performance indices ANOVA

Parameter	Mean(SE)					
	BL	T1	T2	T3	T4	*p value*
ER [%]	N/A	4(1)	19(2)$^{(*)}$	23(2)$^{(*)}$	2(1)	$p<0.001$

N/A: not applicable

$^{(*)}$ significantly different (TK test, α=0.05) with respect to easy tasks.

7.3.2 Data stationarity

The WSS test rejected the null hypothesis of stable mean and variance within the given session. This result was obtained for all sessions (BL, T1,…,T4), for all recordings. Figure 7.1 shows an example of the IBI series for a generic recording.

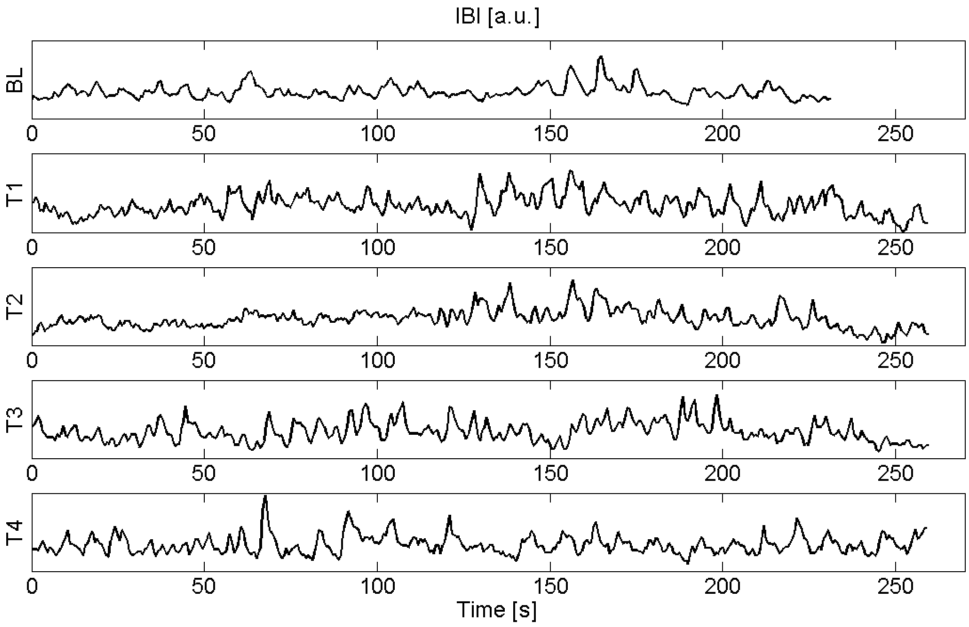

Figure 7.1 Example of IBI series. The de-trended IBI series is shown for each of the five sessions (BL, T1,..,T4) for a randomly chosen recording. The WSS condition was not satisfied ($p>0.05$).

7.3.3 HRV analysis

Table 7.2 summarizes ANOVA of all variability indices. The reported *p* values refer to ANOVA, indicating confidence level in rejecting the null hypothesis of all sessions having the same mean for the given parameter (row of table). *Post hoc* analysis was computed on parameters showing significant differences among sessions. Indices and ranges for multiple comparisons (RMC) are shown in Figure 7.2 and Figure 7.3. Dotted vertical lines mark the boundaries (95% C.I.) of baseline variability (BLV). Sessions whose RMC lies outside BLV are significantly different from BL.

A significant difference in the groups mean was observed for indices SDNN, SD2, P_{LF}, SampEn, IEV_{LF}, IEV_{LF+HF} across the five sessions (BL, T1,…,T4). Post hoc analysis (TK HSD test) showed that SampEn was able to discriminate between SST performance (T1,…,T4) and rest (BL) (Table 7.2 and Figure 7.2). Other indices (SDNN, SD2, P_{LF}, IEV_{LF}, IEV_{LF+HF}) were able to discriminate some tasks from baseline, but not all. Index IEV_{LF+HF} was able to discriminate difficult tasks from the other sessions (Table 7.2 and Figure 7.3). However no indices were able to discriminate easy from difficult tasks (i.e. difficulty level) as shown in Figure 7.2 and Figure 7.3 by overlapping RMC of easy and difficult tasks.

SampEn reported in this section was computed for an embedding dimension m=4, although other values (m=3,…,5) were also tested and lead to similar results.

Table 7.2 HRV indices ANOVA

Parameter	Mean(SE)					
	BL	T1	T2	T3	T4	*p value*
Mean-IBI[ms]	1012(42)	1002(46)	973(42)	988(39)	1011(35)	*N.S.*
SDNN [ms]	73(5)	59(5)	48(4) $^{\Delta}$	48(4) $^{\Delta}$	54(5) $^{\Delta}$	*$p<0.005$*
RMSSD [ms] (a)	1.59(0.06)	1.56(0.07)	1.49(0.06)	1.51(0.06)	1.56(0.06)	*N.S.*
SD1 [ms] (a)	1.44(0.06)	1.41(0.07)	1.34(0.06)	1.36(0.06)	1.41(0.06)	*N.S.*
SD2 [ms]	97(6)	76(6)	62(4) $^{\Delta}$	62(4) $^{\Delta}$	70(6) $^{\Delta}$	*$p<0.001$*
P_{LF} [ms^2] (a)	2.90(0.08)	2.55(0.09)	2.46(0.10) $^{\Delta}$	2.56(0.09)	2.58(0.10)	*$p<0.05$*
P_{HF} [ms^2] (a)	2.67(0.12)	2.56(0.13)	2.40(0.12)	2.45(0.11)	2.52(0.12)	*N.S.*
P_{LF+HF} [ms^2] (a)	3.15(0.08)	2.93(0.10)	2.78(0.10)	2.85(0.09)	2.90(0.10)	*N.S.*
P_{LF}/P_{HF} [a.u.]	2.38(0.49)	1.73(0.43)	1.75(0.37)	1.74(0.31)	1.63(0.29)	*N.S.*
SampEn [a.u.]	1.74(0.12)	1.08(0.13) $^{\Delta}$	1.06(0.12) $^{\Delta}$	1.07(0.09) $^{\Delta}$	1.13(0.10) $^{\Delta}$	*$p<0.001$*
IEV_{LF} [a.u.] (a)	11.03(0.15)	10.31(0.17) $^{\Delta}$	10.24(0.18) $^{\Delta}$	10.26(0.15) $^{\Delta}$	10.41(0.17)	*$p<0.01$*
IEV_{HF} [a.u.] (a)	10.09(0.24)	9.76(0.24)	9.57(0.18)	9.56(0.21)	9.78(0.22)	*N.S.*
IEV_{LF+HF} [a.u.] (a)	11.21(0.15)	10.65(0.18)	10.49(0.18) $^{\Delta}$	10.53(0.15) $^{\Delta}$	10.70(0.18)	*$p<0.05$*
IEM_{LF}/ IEM_{HF} [a.u.] (a)	3.00(0.52)	1.77(0.34)	1.75(0.34)	1.96(0.37)	1.88(0.30)	*N.S.*

(a) distribution log-transformed

$^{\Delta}$ significantly different from baseline (TK HSD test, *$p<0.05$*)

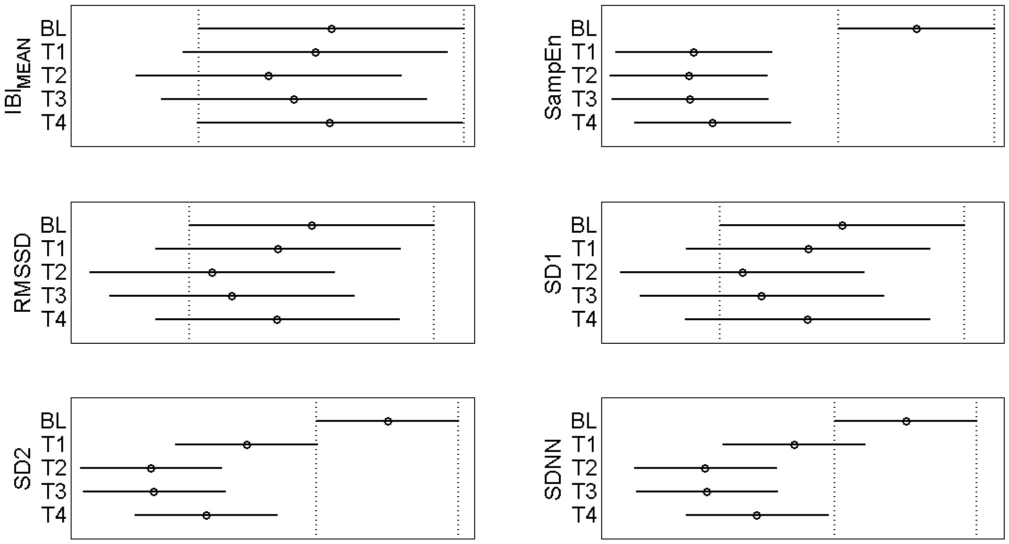

Figure 7.2 Variability of time indices. Time-domain parameters and range for multiple comparisons (RMC) are shown. Dotted vertical lines mark the boundaries (95% C.I.) of baseline variability. Sessions whose RMC do not overlap are significantly different. SampEn discriminates (any) task from baseline.

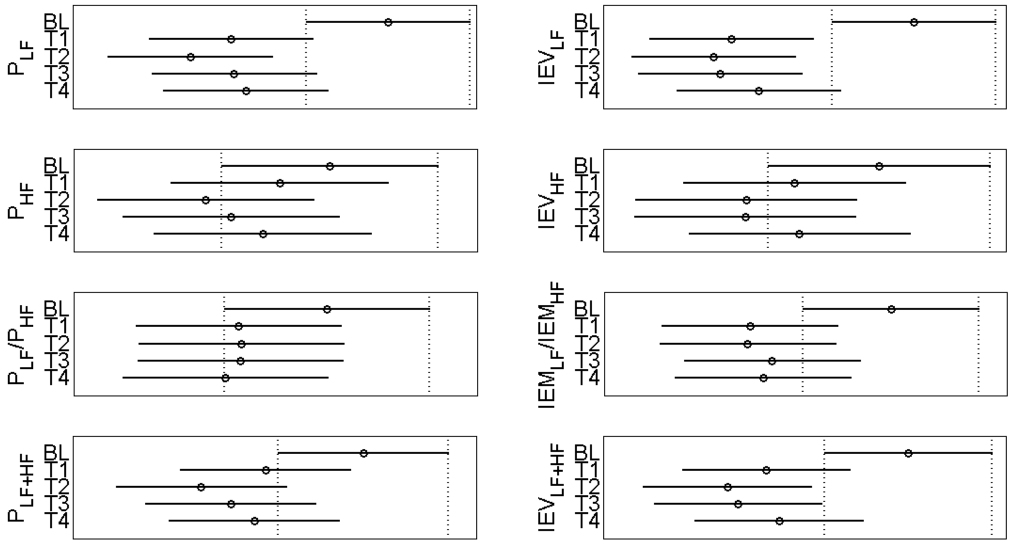

Figure 7.3 Variability of frequency and time-frequency indices. Frequency-domain parameters and range for multiple comparisons (RMC) are shown. Dotted vertical lines mark the boundaries (95% C.I.) of baseline variability. Sessions whose RMC do not overlap are significantly different. IEV_{LF+HF} is significantly different in difficult tasks (T2, T3) with respect to other sessions (BL, T1, T4).

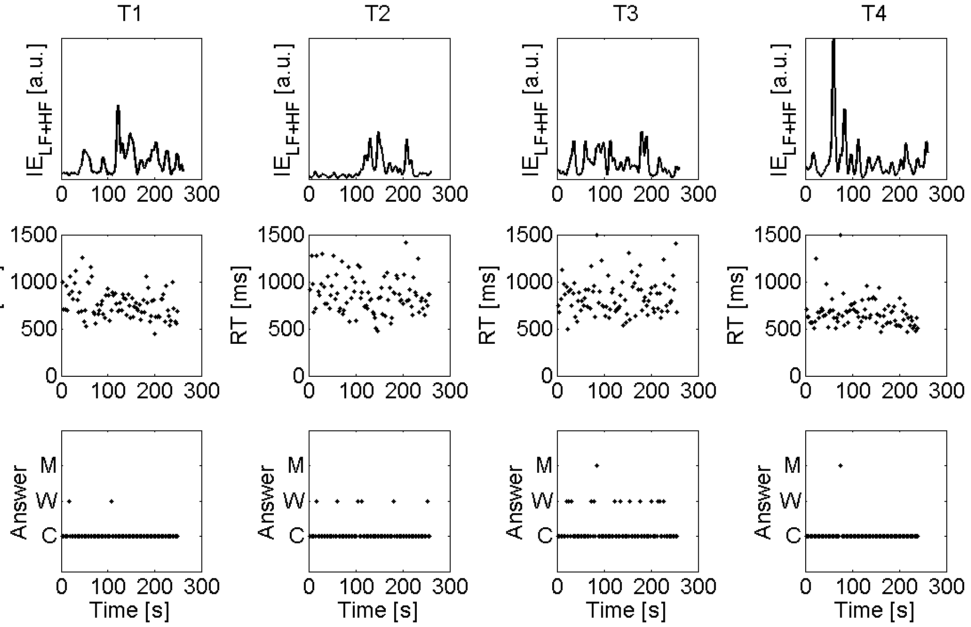

Figure 7.4 Temporal evolution of instantaneous energy and performance indices. Example of temporal evolution of instantaneous energy (IE), reaction time (RT) and answer (C: correct, W: wrong, M: missing) for the four tasks (T1,…,T4).

7.3.3 Time-frequency HRV analysis

Figure 7.4 shows an example of temporal evolution of IE and associated RT and answer (C: correct, W: wrong, M: missing) for all trials, for the four tasks. RT is bounded to 1500 ms by the protocol. The difficult tasks (T2, T3) show increased ER and decreased IEV with respect to the easy tasks.

7.4 Discussion

In the present study, the contribution of regularity and joint time-frequency analyses of non-stationary HRV in discriminating between performance (SST task execution) and rest was assessed and compared to the standard HRV (Task Force, 1996) approach.

Preliminary assessment of weak-sense stationarity of the (first order de-trended) IBI series was performed on individual sessions (BL, T1,…,T4) of each recording. The WSS condition was not met, in any recordings, suggesting that time-frequency methods not relying on data stationarity could exhibit improved ability in discriminating baseline from task execution.

To verify actual difference in task difficulty level (SST easy vs. SST difficult), ER was adopted as performance index. ER was found significantly different in difficult tasks with respect to the easy ones (TK HSD, $p<0.05$).

Post hoc multiple comparisons analysis of the time-domain indices showed that only regularity index SampEn was able to discriminate ($p<0.05$) SST task execution (performance) from baseline (rest). This parameter quantifies the degree of complexity of the IBI series. Lower values of SampEn indicate increased regularity (decreased complexity). To the authors' knowledge, no studies have been presented in literature using SampEn in short-term HRV analysis of cognitive effort in response to memory search tasks.

A recent work (Vuksanović and Gal, 2007) on arithmetic mental stress with verbalization in which a similar experimental setting (age range of participants, task duration) was used, SampEn was also found lower during mental task execution with respect to the resting stage preceding the task performance.

However, in the present study, the significant decrease in SampEn during task execution indicating increased regularity of the IBI series, was not reflected by a significant decrease in the total power (P_{LF+HF}), suggesting the superior ability of the time-domain non linear index in discriminating performance from rest.

Long-term variability indices (SDNN, SD2) were able to discriminate tasks following the first (T2, T3, T4). The significant decrease in "slow variability" indices (SDNN, SD2) during SST task performance appears to be consistent with previous work in which a memory scanning task was used (Redondo and Del Valle-Inclán, 1992). However, standard HRV frequency-domain indices (P_{LF}, P_{HF}, P_{LF}/P_{HF}) did not show the discrimination ability of the time-domain indices. P_{LF} was reduced during task execution (Figure 7.3) in accordance to previous findings (Mulder *et al.*, 2000; Nickel and Nachreiner, 2003) but not significantly.

In Figure 7.3, frequency-domain indices of standard HRV (left column) are compared to those from the time-frequency domain (right column). In the LF band (0.04-0.15 Hz), IEV_{LF}

was able to discriminate three tasks (T1,T2,T3) from baseline, whereas P_{LF} could only discriminate one (T2). Unlike any indices from standard HRV, index IEV_{LF+HF} was able to discriminate difficult tasks from other sessions (baseline and easy tasks).

It shall be noted that, given the short duration of the sessions (less than 5 min), the LF+HF frequency band (from 0.04 Hz to half the mean heart rate) comprises the entire frequency band of interest. Hence, IEV_{LF+HF} represents a measure of “global” variability of the energy distribution of the IBI series.

However, none of the above indices were able to discriminate task difficulty, consistently with previous work (Nickel and Nachreiner, 2003).

7.5 Conclusions

In this study psychophysiological workload in response to a high-speed memory scanning task (Sternberg, 1966) in healthy young subjects was assessed by means of standard HRV indices complemented with joint time-frequency and regularity analyses of the IBI-series.

A superior ability of regularity index (SampEn) in discriminating performance (task execution) from rest; and instantaneous energy variability (IEV_{LF+HF}) in discriminating difficult tasks from other sessions (rest and easy tasks) was shown in non-stationary IBI series, suggesting a potential use of the proposed indices in discriminating PPW levels in response to varying SST difficulty. However, replication on a larger dataset is required to confirm the validity of the proposed method.

References

Aasman J, Mulder G, Mulder LJM. Operator effort and the measurement of heart rate variability. *Hum Factors* 1987; 29(2):161–170.

Bailón R, Laouini G, Grao C, Orini M, Laguna P, Meste O. The Integral Pulse Frequency Modulation Model With Time-Varying Threshold: Application to Heart Rate Variability Analysis During Exercise Stress Testing. *IEEE Trans Biomed Eng* 2011a; 58(3):642–52.

Bailón R, Serrano P, Laguna P. Influence of time-varying mean heart rate in coronary artery disease diagnostic performance of heart rate variability indices from exercise stress testing. *J Electrocardiol* 2011b; 44(4):445–52.

Berntson GG, Bigger JT Jr, Eckberg DL, Grossman P, Kaufmann PG, Malik M, Nagaraja HN, Porges SW, Saul JP, Stone PH, van der Molen MW. Heart rate variability: origins, methods, and interpretive caveats. *Psychophysiology* 1997; 34(6):623–48.

Choi H, Williams WJ. Improved time-frequency representation of multicomponent signals using exponential kernels. *IEEE Trans Acoust, Speech Signal Processing* 1989; 37(6):862–871.

Cohen L. Time-frequency distribution: a review. *Proc IEEE* 1989; 77(7):941–981.

Fairclough SH, Roberts JS. Effects of performance feedback on cardiovascular reactivity and frontal EEG asymmetry. *Int J Psychophysiol* 2011; 81(3):291–298.

Hamilton P. Open source ECG analysis. *Comp Cardiol* 2002; 29:101–104.

Henelius A, Hirvonen K, Holm A, Korpela J, Muller K. Mental workload classification using heart rate metrics. *Conf Proc IEEE Eng Med Biol Soc* 2009; 1836–39.

Hjortskov N, Rissén D, Blangsted AK, Fallentin N, Lundberg U, Søgaard K. The effect of mental stress on heart rate variability and blood pressure during computer work. *Eur J Appl Physiol* 2004; 92(1-2):84–9.

Jasson S, Médigue C., Maison-Blanche P, Montano N, Meyer L, Vermeiren C, Mansier P, Coumel P, Malliani A, Swynghedauw B. Instant power spectrum analysis of heart rate variability during orthostatic tilt using a time-/frequency-domain method. *Circulation* 1997; 96(10):3521–3526.

Magagnin V, Bassani T, Bari V, Turiel M, Maestri R, Pinna GD, Porta A. Non-stationarities significantly distort short-term spectral, symbolic and entropy heart rate variability indices. *Physiol Meas* 2011; 32(11):1775–1786.

Mathewson KJ, Jetha MK, Drmic IE, Bryson SE, Goldberg JO, Hall GB, Santesso DL, Segalowitz SJ, Schmidt LA. Autonomic predictors of Stroop performance in young and middle-aged adults. *Int J Psychophysiol* 2010; 76(3):123–9.

Mukherjee S, Yadav R, Yung I, Zajdel DP, Oken BS. Sensitivity to mental effort and test-retest reliability of heart rate variability measures in healthy seniors. *Clin Neurophysiol* 2011; 122(10):2059–66.

Mulder G, Mulder LJM, Meijman TF, Veldman JBP, Van Roon AM. A psychophysiological approach to working conditions. In Backs, R.W., Boucsein, W., (Eds.), *Engineering psychophysiology: Issues and applications*. Erlbaum, Mahwah, 2000; pp. 139–159.

Nickel P, Nachreiner F. Sensitivity and diagnosticity of the 0.1-Hz component of heart rate variability as an indicator of mental workload. *Hum Factors* 2003; 45(4):575–90.

Parlitz U, Berg S, Luther S, Schirdewan A, Kurths J, Wessel N. Classifying cardiac biosignals using ordinal pattern statistics and symbolic dynamics. Comput. Biol. Med. [ahead of print]

Pincus SM, Goldberger AL. Physiological time-series analysis: what does regularity quantify?.*Am J Physiol* 1994; 266(4 pt 2):H1643–56.

Pola S, Macerata A, Emdin M, Marchesi C. Estimation of the power spectral density in nonstationary cardiovascular time series: assessing the role of the time-frequency representations (TFR). *IEEE Trans Biomed Eng* 1996; 43(1):46–59.

Porta A, D'Addio G, Guzzetti S, Lucini D, Pagani M. Testing the Presence of Non Stationarities in Short Heart Rate Variability Series. *Comp Cardiol* 2004; 31:645–648.

Richman JS, Moorman RJ. Physiological time-series analysis using approximate entropy and sample entropy. *Am J Physiol Heart Circ Physiol* 2000; 278(6):H2039–49.

Redondo M, Del Valle-Inclán F. Decrements in heart rate variability during memory search. *Int J Psychophysiol* 1992; 13(1):29–35.

Schumacher A. Linear and nonlinear approaches to the analysis of R-R interval variability. *Biol Res Nurs* 2004; 5(3):211–221.

Signorini MG, Ferrario M, Cerutti S, Magenes G. Advances in Monitoring Cardiovascular Signals. Contribution of Nonlinear Signal Processing. *Conf Proc IEEE Eng Med Biol Soc* [ahead of print]

Sternberg S. High-speed scanning in human memory. *Science* 1966; 153, 652–54.

Task Force of the European Society of Cardiology the North American Society of Pacing Electrophysiology. Heart Rate Variability Standards of Measurement, Physiological Interpretation, and Clinical Use. *Circulation* 1996; 93(5):1043–65.

Vuksanović V, Gal V. Heart rate variability in mental stress aloud. *Med Eng Phys* 2007; 29(3):344–349.

Part III

This part presents the analysis of the atrial activation signal (continuous wavefront) in atrial fibrillation, with emphasis on original contributions. In Chapter 8 a novel method for online electrocardiogram delineation based on wavelet-transforms and 32-bit integer linear algebra is presented. In Chapter 9 a novel method for the estimation of the atrial signal and the dominant fibrillatory rate based on surface electrocardiogram is presented. In Chapter 10 the analysis of temporal variability of spatial complexity and spectral distribution in body surface potential maps is presented, based on a novel approach built on the automatic delineation method introduced in Chapter 8. Emphasis is given to the novel finding of linear correlation between spectral concentration and temporal regularity of spectral distribution.

Scientific work:

Chapter 8:

Di Marco LY and Chiari L. A wavelet-based ECG delineation algorithm for 32-bit integer online processing. *Biomed Eng Online* 2011 Apr 3;10:23.

Chapter 9:

Di Marco LY, King S, Bourke JP, Chiari L, Murray A, Langley P. Time-frequency analysis of atrial fibrillation comparing morphology-clustering based QRS-T cancellation with blind source separation in multi-lead surface ECG recordings. *Comp Cardiol* 2011; 38:269−272.

Chapter 10:

Di Marco LY, Bourke JP, Langley P. Spatial complexity and spectral distribution variability of atrial activity in surface ECG recordings of atrial fibrillation. *Med Biol Eng Comp* [in press]

Chapter 8: A wavelet-based ECG delineation algorithm for 32-bit integer online processing

Abstract

Since the first well-known electrocardiogram (ECG) delineator based on Wavelet Transform (WT) presented by Li *et al.* in 1995, a significant research effort has been devoted to the exploitation of this promising method. Its ability to reliably delineate the major waveform components (P, Q and mono- or bi-phasic T wave) would make it a suitable candidate for efficient online processing of ambulatory ECG signals. Unfortunately, previous implementations of this method adopt non-linear operators such as *root mean square* (RMS) or floating point algebra, which are computationally demanding.

This paper presents a 32-bit integer, linear algebra advanced approach to online QRS detection and P-Q-T waves delineation of a single lead ECG signal, based on WT.

The QRS detector performance was validated on the MIT-BIH Arrhythmia Database (sensitivity Se=99.77%, positive predictive value P+=99.86%, on 109010 annotated beats) and on the European ST-T Database (Se=99.81%, P+=99.56%, on 788050 annotated beats). The ECG delineator was validated on the QT Database, showing a mean error between manual and automatic annotation below 1.5 samples for all fiducial points: P-onset, P-peak, P-offset, QRS-onset, QRS-offset, T-peak, T-offset, and a mean standard deviation comparable to other established methods.

The proposed algorithm exhibits reliable QRS detection as well as accurate ECG delineation, in spite of a simple structure built on integer linear algebra.

8.1 Introduction

The electrocardiogram (ECG) is the recording of the electrical activity of the heart by means of electrodes placed on the body surface. It is the most commonly used non-invasive test in primary care for heart rate and rhythm-related abnormalities detection (Fairweather *et al.*, 2007; Hooper *et al.*, 2001). In recent years the interest for the ECG signal analysis has extended from clinical practice and research to disciplines such as cognitive psychophysiology (Causse *et al.*, 2010; Healey and Picard, 2005), physical training (Corrado *et al.*, 2010; Higgins, 2008) and rehabilitation (Mutikainen *et al.*, 2009).

Many non-diagnostic applications do not require the full 12-lead setup of clinical ECG, employing a limited number of electrodes. In some cases a single lead setup, requiring only three electrodes, is sufficient. Such applications focus on ambulatory ECG monitoring, namely in unconstrained conditions, in which subjects perform normal activities as in their daily life (Bowers *et al.*, 2008; Figueiredo *et al.*, 2010; Healey and Picard, 2005; Porges and Byrne, 1992).

Ambulatory ECG analysis requires processing of signals which are affected by considerable noise, mainly caused by electrode motion and muscular activity, more prominently than in resting ECG recordings, and by power-line coupling. Moreover, emerging wearable technologies for ambulatory ECG monitoring have limited processing resources and low power budget.

Clinical information on the cardiac beat is carried by the waveforms appearing on the electrocardiogram, namely: QRS-complex and P, T, U, waves. Their amplitudes and relative time intervals provide insight on heart rhythm abnormalities and heart disease such as ischemia and myocardial infarction. Electrocardiogram delineation is the automatic process of determining such amplitudes and time intervals.

Performing an accurate delineation is quite a challenging task, for many reasons. For example, the P wave is characterized by low amplitude and may be masked by electrode motion or by muscular noise. The P and T waves may be biphasic, which increases the difficulty to accurately determine their onset or offset. Moreover, some arrhythmic beats may not contain all the standard ECG waves, for example the P wave may be missing, while in accelerated heart rate patterns, it might be partially overlapped to the T wave of the previous beat.

The first stage of ECG delineation is devoted to detecting the QRS-complex, which in most cases is the most pronounced wave of the heart cycle. Subsequent processing locates P, QRS-complex and T waves fiducial points (onset, peak, offset).

The cyclic nature of the ECG signal and its spectral components, which mainly appear in well-known and distinguishable frequency bands, make ECG a suitable candidate for multi-resolution decomposition by means of wavelet transforms (Mallat, 1989; Mallat and Zhong, 1992). Methods based on wavelet transforms have been proposed by numerous authors (Addison, 2005; Boichat *et al.*, 2009; Ghaffari *et al.*, 2009; Martinez *et al.*, 2004; Sivannarayana and Reddy, 1999; Sovilj *et al.*, 2004), building on the first well-known ECG delineator proposed by Li and coworkers (Li *et al.*, 1995).

Unfortunately, most of these ECG delineation algorithms adopt non-linear operators such as *root mean square* (RMS) or floating point algebra, which are computationally demanding. The work by Sovilj and coworkers (Sovilj *et al.*, 2004) presents a real-time implementation of QRS detection and P wave delineation, though no validation on standard databases is provided, nor is the P wave delineation criterion explained. In (Bahoura, 1997) a WT-based algorithm for real-time QRS detection and ECG delineation is presented, though no validation is reported on delineation, and the total number of annotated beats used in the validation of QRS detection does not match the record-by-record count, as noted in (Martinez *et al.*, 2004).

The work by Boichat and coworkers (Boichat *et al.*, 2009) presents a real-time implementation of the offline method proposed in (Martinez *et al.*, 2004), though no validation on arrhythmia databases (such as the MIT-BIH Arrhythmia Database) is provided. The delineation of QRS onset and QRS offset in (Boichat *et al.*, 2009) is performed on WT detail coefficients at scale 2^4, namely on the output of a pass-band FIR filter with a 3dB band of 4.1-13.5 Hz. Moreover, the criterion adopted for the validation of the delineation algorithm is based on a 320 ms window, which exceeds the maximum tolerance (150 ms) for QRS detection accuracy allowed by the ANSI/AAMI-EC57:1998 standard.

This paper presents a wavelet-based algorithm for single lead QRS detection and ECG delineation of P wave, QRS-complex and T wave, under the algorithmic constraint of 32-bit integer linear algebra online processing and compliance with ANSI/AAMI-EC57:1998 requirements on QRS detection accuracy. The algorithm was validated on MIT-BIH Arrhythmia Database (MITDB), the European ST-T Database (EDB), and QT Database (QTDB), available from Physionet.

8.2 Methods

8.2.1 Wavelet Transform

The general theory on wavelet transforms for multi-resolution analysis is described in detail in (Mallat, 1989; Mallat, 1989; Mallat and Zhong, 1992) and its application to ECG signal delineation is presented in (Li *et al.*, 1995; Martinez *et al.*, 2004) while a review is given in (Addison, 2005).

With reference to the family of spline functions of degree *2r+2* proposed in (Mallat and Zhong, 1992) for the smoothing function $\theta(t)$, in this study the 8th degree (r=3) was adopted. Its Fourier transform is expressed in (8.1.1) and the Fourier transform of the wavelet function is expressed in (8.1.2).

$$\Theta(\omega) = \left(\frac{\sin \frac{\omega}{4}}{\frac{\omega}{4}} \right)^8 \tag{8.1.1}$$

$$\Psi(\omega) = j\omega \left(\frac{\sin \frac{\omega}{4}}{\frac{\omega}{4}} \right)^8 \tag{8.1.2}$$

Unlike previous studies (Bahoura *et al.*, 1997; Boichat *et al.*, 2009; Ghaffari *et al.*, 2009; Li *et al.*, 1995; Martinez *et al.*, 2004; Sovilj *et al.*, 2004) where a cubic spline smoothing function $\theta(t)$ (r=1) was used, in this study a higher value of r was adopted to reduce the width of the compact support and the pass-band of the equivalent filter for scales higher than 2^1, to improve frequency band separation across scales. However, the number of filter taps increases with r, therefore a tradeoff should be determined between computational effort and delineation performance.

Figure 8.1 shows the smoothing function $\theta(t)$ and wavelet function $\psi(t)$ for r=1 and r=3. The compact support of the smoothing (scaling) function decreases in width as r increases.

The low-pass filter H and high-pass filter G derived from (8.1.1) and (8.1.2) can be expressed as:

$$H(e^{j\omega}) = e^{j\frac{\omega}{2}}\left(\cos\frac{\omega}{2}\right)^7$$
$$G(e^{j\omega}) = 4je^{j\frac{\omega}{2}}\sin\left(\frac{\omega}{2}\right) \tag{8.2}$$

whose finite impulse response h_n and g_n are given by the coefficients reported in Table 8.1.

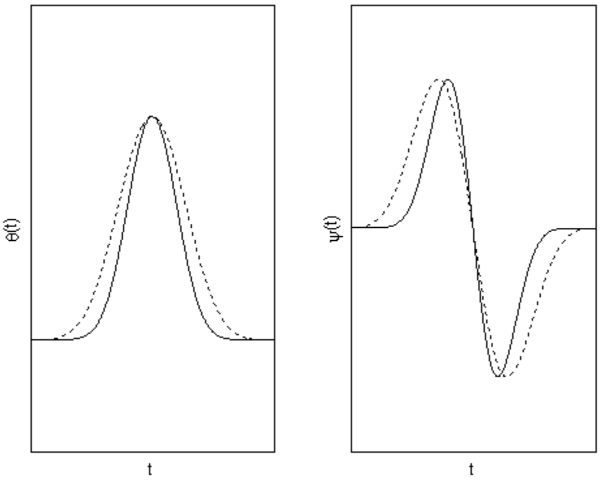

Figure 8.1 Smoothing function and wavelet function. Smoothing function θ(t) (left) and wavelet function ψ(t) (right), for r=1 (dotted line) and r=3 (solid line).

Table 8.1 – Wavelet Filters Impulse Response

N	h_n	g_n
-2	1/128	
-1	7/128	
0	21/128	-2
1	35/128	2
2	35/128	
3	21/128	
4	7/128	
5	1/128	

It shall be noted that h_n is symmetrical and of even length, representing a linear phase low-pass FIR filter, while g_n is anti-symmetrical of even length, representing a linear phase high-pass FIR filter.

The frequency response for the filter bank generalized for any given scale can be written as:

$$Q_k(e^{j\omega}) = \begin{cases} G(e^{j\omega}), & k = 1 \\ G(e^{j2^{k-1}\omega}) \cdot \prod_{l=0}^{k-2} H(e^{j2^{l}\omega}), & k \geq 2 \end{cases} \tag{8.3}$$

The filter bank structure is illustrated in Figure 8.2.

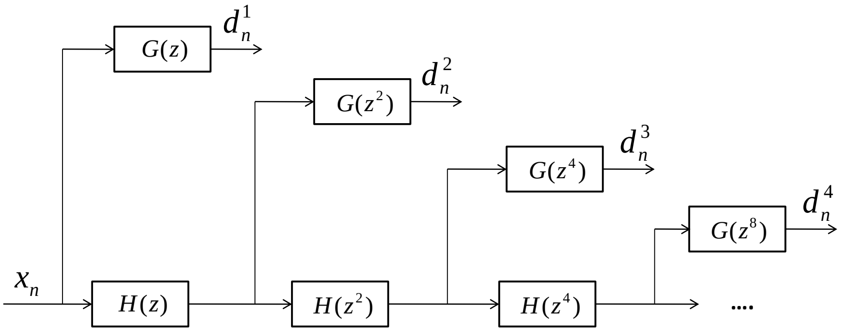

Figure 8.2 DWT filter bank. Filter bank implementation of biorthogonal dyadic wavelet transform without decimation (algorithme à trous). d^k_n is the detail coefficient series for scale 2^k. Inspired by (Martinez *et al.*, 2004).

The frequency response of the equivalent filters Q_k in (8.3) is displayed in Figure 8.3 for the first four scales, for r=1 (cubic spline smoothing function) and r=3 (8th order spline smoothing function). For any given scale 2^k, Q_k pass-band narrows with increasing r, improving frequency separation of the filter bank across scales.

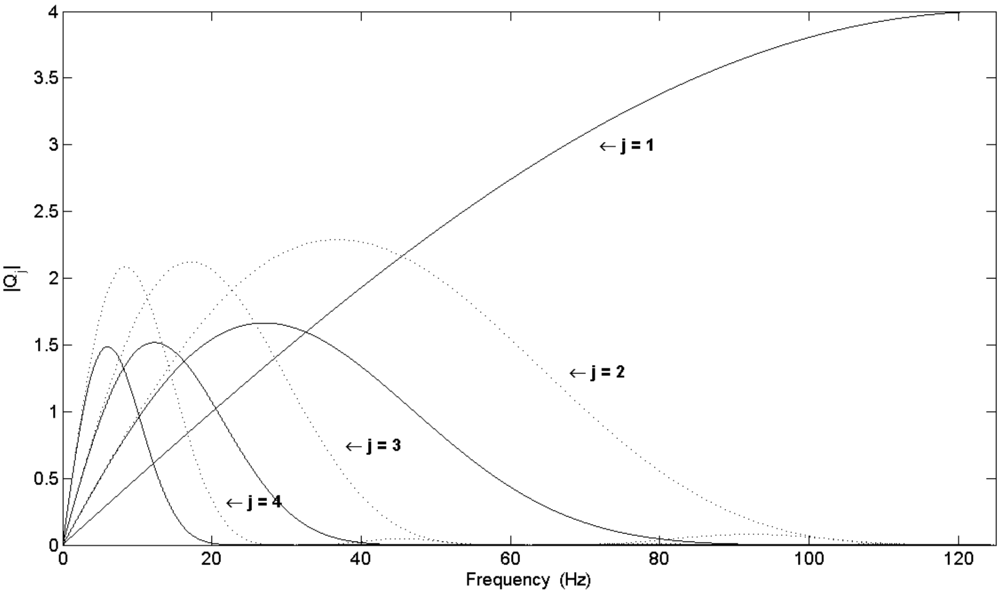

Figure 8.3 Equivalent filters magnitude response. Equivalent Filters Q_k magnitude response, for different scales 2^k, for r=1 (dotted line) and r=3 (solid line). Sample frequency F_s = 250 samples/s.

The group delay of the equivalent filter Q_k must be accounted for in multi-scale analysis of discrete wavelet transform (DWT) coefficients. To match zero-crossings (and their relative modulus-maxima) across different scales, DWT coefficients must be aligned temporally.

The group delay of Q_k at scale 2^k, k >1, is given by:

$$\tau_g^k = \sum_{l=1}^{k-1} \tau_{g,H}^l + \tau_{g,G}^k \tag{8.4.1}$$

where:

$$\tau_{g,H}^l = -3 \cdot 2^{l-2} \tag{8.4.2}$$

is the group delay of the low-pass filter at scale 2^l , and

$$\tau_{g,G}^k = -2^{k-2} \tag{8.4.3}$$

is the group delay of the high-pass filter at scale 2^k.

According to (Clifford *et al.*, 2006; Pan and Tompkins, 1985), the energy of the main waveforms composing the ECG, namely QRS-complex, P and T waves, lies within a limited frequency range. As a consequence, a limited number of scales is required for ECG delineation. Table 8.2 summarizes the cutoff frequencies of Q_k filters for the scales of interest, for *r*=1 and *r*=3.

Table 8.2 – Wavelet Filters Bandwidth

Scale 2^k	Bandwidth [Hz] (*) Cubic Spline θ(t) (*r*=1)	Bandwidth [Hz] (*) 8th order Spline θ(t) (*r*=3)
k = 1	62.50 – 125.00	62.50 – 125.00
k = 2	18.02 – 58.60	13.12 – 43.55
k = 3	8.36 – 27.46	5.98 – 19.99
k = 4	4.11 – 13.52	2.93 – 9.80

(*) 3 dB cut-off

8.2.2 Description of the Algorithm

The raw ECG signal is assumed to be sampled at 250 samples/s. The databases used for validation contain records of ECG data stored at 12-bit/sample. Therefore, to prevent overflow in a (signed) integer implementation of the low-pass filter adopted in the filter bank, 16-bit integer capacity is not sufficient. This constitutes the only reason for adopting a 32-bit instead of 16-bit implementation. However, a 32-bit implementation also complies with input signals (raw ECG data) with a sample resolution up to 24-bit/sample. Most, if not all, commercially available ECG front-end devices currently fall within this category. In order to comply with the largest set of such devices on the market, no assumptions are made on the amplitude resolution (typically expressed in units of μV)

The DWT properties which the proposed method is based on are well described in (Li *et al.*, 1995; Martinez *et al.*, 2004). Based on the properties of the filter bank (8.2), the zero-crossings of the DWT coefficients d^k_n correspond to the local maxima or minima of the smoothed input signal at different scales, and the maximum absolute values of d^k_n are associated with maximum slopes in the filtered signal (Martinez *et al.*, 2004).

Figure 8.4 shows DWT detail coefficients computed by the present algorithm, for actual ECG signals (record 108 and 208, from MITDB).

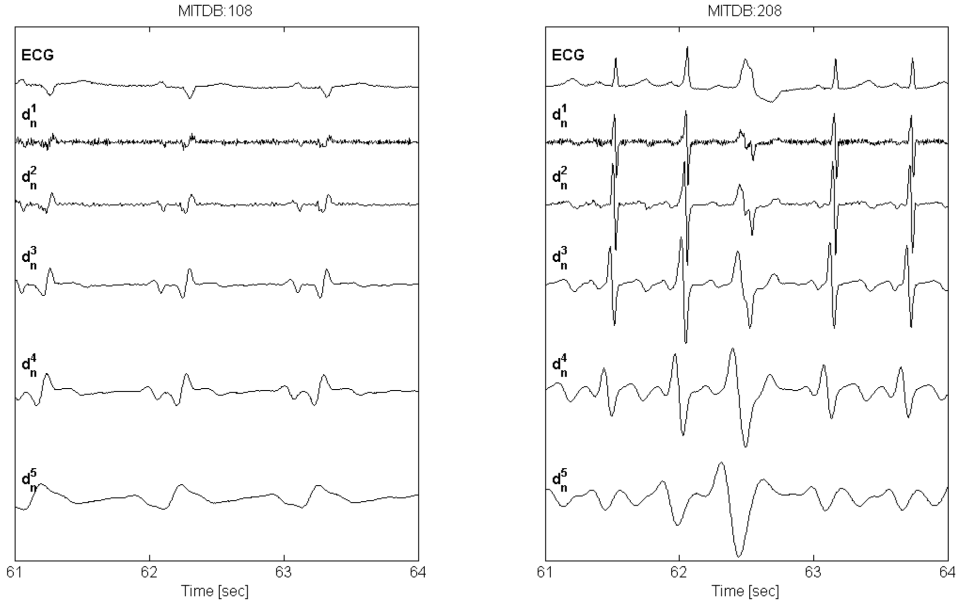

Figure 8.4 ECG signal and DWT decomposition. Examples of ECG signals from MITDB records (resampled at F_S=250 samples/s) MITDB:108 (left), MITDB:208 (right), and DWT detail coefficient d^k_n at scales 2^1 through 2^5.

At a sampling frequency of 250 samples/s, the spectral content of the ECG signal mainly falls within the first five scales of the filter bank (8.2). In particular, the QRS-complex is prominent at scales 2^2 and 2^3 while its energy decreases at increasing scales and becomes very low at scales higher than 2^4, while P shows high energy at scale 2^3 which decreases at higher ones. At scales 2^3 through 2^5 T wave has high energy, though at scale 2^5 the baseline drift, including respiration effects, becomes prominent. For this reason, scale 2^5 is not considered in this study. At scales 2^1 and 2^2 small peaks in Q and S waves may show zero-crossings though at such low scales, especially scale 2^1, muscular noise and power-line coupling may appear.

Using the information of local maxima, minima and zero-crossing at the scales of interest, the algorithm identifies for each beat the significant points of the ECG in the following steps: 1) detection of the QRS-complex; 2) QRS-complex delineation (onset, offset); 3) P wave delineation (onset, peak, offset); 4) T wave delineation (peak, offset) of the previous beat. Figure 8.5 displays the flow chart of the state machine for online parsing of detail coefficients d^2_n, for QRS detection. Unlike previous works (Li *et al.*, 1995; Martinez *et al.*, 2004), for QRS detection only two scales (2^2, 2^3) are processed.

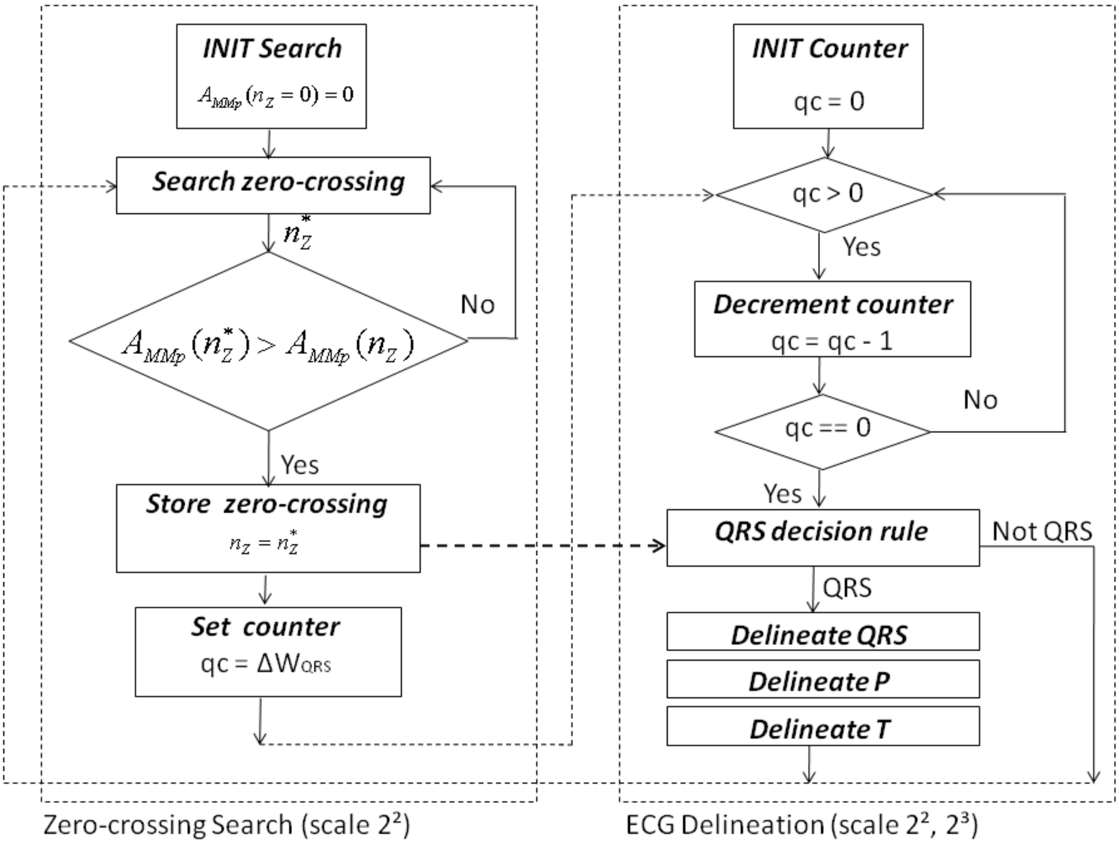

Figure 8.5 ECG delineation state machine. State Machine flow chart for online ECG delineation. The zero-corssing n_Z with the largest modulus-maxima pair amplitude $A_{MMp}(nZ)$ is detected within ΔW_{QRS} (250 ms) at scale 2^2. Detail coefficients d^k_n at scales 2^2 and 2^3 are parsed for the verification of QRS candidates according to the QRS-detection decision rule. After QRS-complex detection, the delineation process delineates in the order: the QRS-complex, the P wave, and the T wave.

The algorithm proposed in this work was intended for online processing, therefore it is causal: at discrete time T_i, only ECG samples at $T_k \leq T_i$ are assumed to be available.

To comply with low power budget constraints, the algorithm does not perform back-search for missed beats. The drawback is a decrease in sensitivity; the advantage is a decrease in storage memory and processing time. A memory buffer of 1 s for WT coefficients is sufficient for QRS detection, whereas the required storage size increases (depending on the inter-beat interval duration, in general no more than 1.5 s) for computing delineation of the T wave of the previous beat.

QRS detection

For each beat, the QRS-complex is detected using wavelet detail coefficients d^k_n at scales 2^2 and 2^3. As shown in Figure 8.5, only scale 2^2 is parsed for zero-crossings. When a zero-crossing is detected, the adjacent modulus-maxima pair $MMp(n_Z)$ is determined and the associated amplitude $A_{MMp}(n_Z)$, defined as the difference between the positive maximum and negative minimum detail coefficients, is computed. The zero-crossing is stored and an observation window ΔW_{QRS} of 250 ms is initialized: if a new zero-crossing n_Z^* is detected within this window such that $A_{MMp}(n_Z^*) > A_{MMp}(n_Z)$, the window is reset and n_Z^* is stored, replacing n_Z, as shown in Figure 8.5. The process is repeated until a full window elapses without new candidates. The zero-crossing n_Z represents the QRS-candidate. The QRS-detection decision rule is defined as follows: a window of 200 ms centred around n_Z is considered, and the maximum-minimum difference $\Delta_{d^2_n}(n_Z)$ of detail coefficients within such window, at scale 2^2, is computed:

$$\Delta_{d_n^2}(n_Z) \equiv \max_{n\in[n_Z-\Delta W,\, n_Z+\Delta W]}\left\{ d_n^2 \right\} - \min_{n\in[n_Z-\Delta W,\, n_Z+\Delta W]}\left\{ d_n^2 \right\} \tag{8.5.1}$$

where ΔW represents a time interval of 100 ms. The following condition is then tested:

$$\Delta_{d_n^2}(n_Z) > \varepsilon_{QRS}^2 \tag{8.5.2}$$

where ε^2_{QRS} is an empirically determined threshold computed as follows:

$$\varepsilon_{QRS}^2 = \frac{11}{32}\cdot\frac{\sum_{n_Z}\Delta_{d_n^2}(n_z)}{N} \tag{8.5.3}$$

where the summation encompasses the N (=4) most recent QRS-candidates that satisfied (8.5.2). Under the assumption that the time distance between two consecutive beats is generally not longer than 2 s (corresponding to a heart rate of 30 beats/min), it takes not more than 8 s to collect N (=4) confirmed candidates. For this reason, a learning period of 8 s is allowed before the algorithm outputs any detected beats.

If (8.5.2) is met, the decision process proceeds to the next step considering scale 2^3:

$$\Delta_{d_n^3} \equiv \max_{n\in[n_Z-\Delta W,\, n_Z+\Delta W]}\left\{ d_n^3 \right\} - \min_{n\in[n_Z-\Delta W,\, n_Z+\Delta W]}\left\{ d_n^3 \right\} \tag{8.5.4}$$

$$\Delta_{d_n^3} > \varepsilon_{QRS}^3 \tag{8.5.5}$$

where ε^3_{QRS} is an empirically determined threshold computed as in (8.5.3), for scale 2^3. It shall be noted that, in (8.5.4), *n* spans the same window as in (8.5.1). Coefficients across different scales are time-aligned by accounting for the group delay computed in (8.4.1).

If (8.5.2) and (8.5.5) are met, the QRS-candidate is confirmed, thresholds ε^2_{QRS} and ε^3_{QRS} are updated. Then, if the learning period is expired, the zero-crossing is marked as the local peak of a QRS-complex, and the algorithm proceeds for the delineation of P, QRS, T waves.. It shall be noted that thresholds ε^2_{QRS} and ε^3_{QRS} are initialized to zero and iteratively adapt to QRS candidates. At the early stages of this process, QRS misdetections (false positives) are likely to occur. To prevent this, the algorithm does not output any detected QRS complexes until the learning period has expired. A learning period of 8 s is generally sufficient, although there may be extreme conditions such as lead-fail, cardiac arrest, poor signal-to-noise ratio, in which a longer time is required.

QRS delineation

QRS delineation is performed at scale 2^2. After detecting the QRS-complex, the QRS onset fiducial point is determined starting from the position n_{pre} of the modulus maximum preceding the zero-crossing n_Z of the QRS-complex at scale 2^2.

The following thresholds are defined, based on local d^2_n coefficient values:

$$\begin{aligned} \varepsilon^2_{Q\,on,I} &= \frac{d^2_{n\,pre} + d^2_{n\,post}}{32} \\ \varepsilon^2_{Qon,II} &= \frac{d^2_{n\,pre} + d^2_{n\,post}}{16} \end{aligned} \tag{8.5.6}$$

where n_{post} is the sample index of the modulus maximum following n_Z. The delineation algorithm searches back from n_{pre} for negative minima or positive maxima, and stores the first crossing of the threshold $\varepsilon^2_{\mathrm{Qon,\,I}}$ to be assigned to QRS onset in case no modulus maxima are found within a fixed size window of 120 ms preceding n_{pre}.

The algorithm stops when a modulus maximum is detected whose amplitude is lower than the threshold $\varepsilon^2_{Qon,II}$, or the end of the search window has been reached. If at least one modulus maximum is found, a new threshold is defined:

$$\varepsilon^2_{Q\,on,III} = \frac{d^2_{n\,left}}{4} \tag{8.5.7}$$

where n_{left} is the sample index at which d^2_n has its left-most modulus maximum. The algorithm searches back from n_{left} until the first crossing of the new threshold $\varepsilon^2_{Qon,III}$ or the end of the fixed-size window is reached. The value is assigned to QRS onset. The symmetrical criterion is adopted for the determination of QRS offset, starting from the position n_{post} of the modulus maximum following the zero-crossing n_Z. The threshold used for QRS offset delineation are:

$$\begin{aligned} \varepsilon^2_{Q\,off,I} &= \frac{d^2_{n\,post}}{4} \\ \varepsilon^2_{Qoff,II} &= \frac{d^2_{n\,post}}{8} \\ \varepsilon^2_{Qoff,III} &= \frac{d^2_{n\,right}}{4} \end{aligned} \tag{8.5.8}$$

where n_{right} is the sample index of the right-most modulus maximum following n_{post} whose amplitude exceeds threshold $\varepsilon^2_{Qoff,II}$.

Figure 8.6 shows examples of different QRS morphologies from QTDB records, the related manual annotations and the automatic delineation markers.

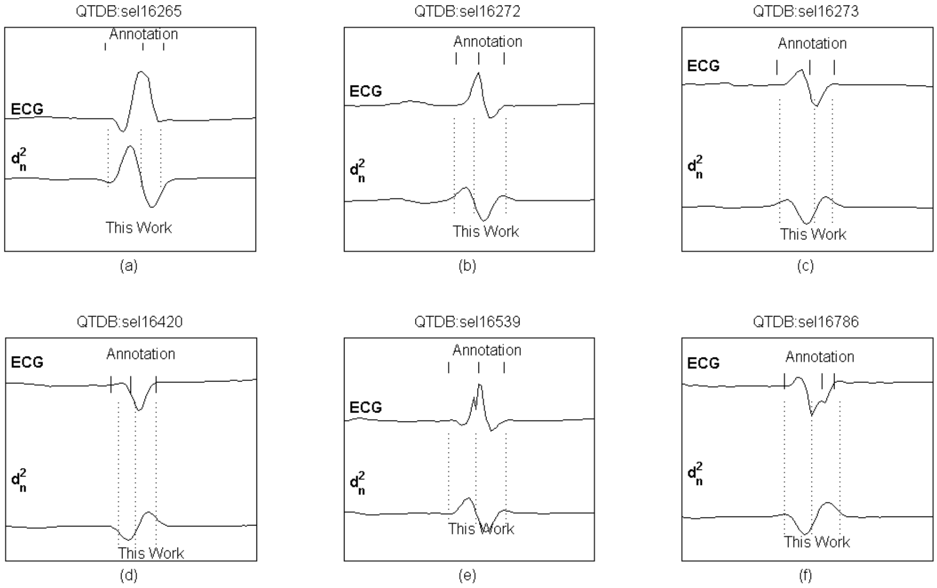

(a) (b) (c)

(d) (e) (f)

Figure 8.6 Delineation of QRS morphologies. Examples of various QRS morphologies from QTDB records, with manual annotations (top) and delineated characteristic points (bottom): QRS onset, dominant QRS peak, QRS offset.

P wave delineation

P wave delineation is performed at scale 2^3. Mono- and bi-phasic P waves are handled. After delineating the QRS-complex, the algorithm searches back from QRS onset on scale 2^3 for the P wave. A fixed-size window whose length is chosen to be the shortest between 300 ms and half the last inter-beat interval is used for the search. Within this window, all zero-crossings are stored. The zero-crossing search is limited to a sub-portion of the window excluding the first (left-most) 100 ms which are only used for determining P onset. The zero crossing n_Z with maximizes $A_{MMp}(n_Z)$ is marked as P wave dominant peak. To determine the mono- bi-phasic morphology of the P wave, specific conditions are tested:

$$\frac{1}{2}\left|d^3_{n\,post}\right| \le \left|d^3_{n\,pre}\right| \le 2\left|d^3_{n\,post}\right| \tag{8.6.1}$$

where $|d^3_{n\,pre}|$ is the modulus maximum preceding the zero-crossing n_Z, at scale 2^3, and $|d^3_{n\,post}|$ is the modulus maximum following n_Z. If (8.6.1) is verified, and a zero-crossing n^L_Z preceding n_Z is available within a distance of 100 ms, (8.6.1) is tested also for n^L_Z. If such condition is verified, the following is also tested:

$$A_{MMp}(n^L_Z) > \frac{3}{4} A_{MMp}(n_Z) \tag{8.6.2.1}$$

If (8.6.1) and (8.6.2.1) are verified for n^L_Z, the P wave is considered to be bi-phasic and n_{pre} is defined as the sample corresponding to the left-most modulus maximum of $MMp(n^L_Z)$ otherwise n_{pre} is defined as the sample corresponding to the left-most modulus maximum of $MMp(n_Z)$.

The same procedure is adopted in the search of n^R_Z following n_Z within a distance of 100 ms. If (8.6.1) is verified for n^R_Z the following condition is tested:

$$A_{MMp}(n_Z^R) > \frac{3}{4} A_{MMp}(n_Z) \tag{8.6.2.2}$$

If (8.6.1) and (8.6.2.2) are verified for n^R_Z, the P wave is considered to be bi-phasic and n_{post} is defined as the sample corresponding to the right-most modulus maximum of $MMp(n^R_Z)$ otherwise n_{post} is defined as the sample corresponding to the right-most modulus maximum of $MMp(n_Z)$.

The sample n_{pre} becomes the starting point for searching back the first crossing of a threshold:

$$\varepsilon^3_{P\,on} = \frac{d^3_{n\,pre}}{4} \tag{8.6.3}$$

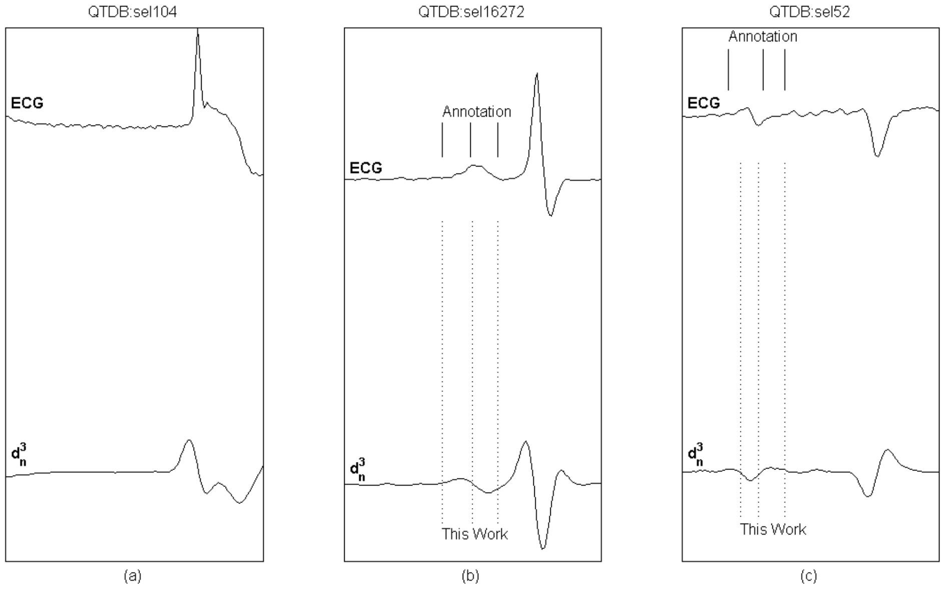

(a) (b) (c)

Figure 8.7 Delineation of P wave. Examples of P waves from QTDB records, with manual annotations (top) and delineated characteristic points (bottom): P onset, dominant P peak, P offset. (a) absent P wave, (b) positive P wave, (c) bi-phasic P wave.

If such crossing point is found within the search window, it is assigned to P onset.

The algorithm then searches for P offset, namely the estimated end of P, adopting the same procedure described for P onset. The threshold adopted is:

$$\varepsilon^3_{P\,off} = \frac{35 \cdot d^3_{n\,post}}{64} \qquad (8.6.4)$$

If P onset, peak and offset are found within the search window, P wave delineation result is positive, otherwise the algorithm declares that P wave could not be delineated for the given beat. Figure 8.7 shows examples of P morphologies from QTDB records, the related manual annotations and the automatic delineation markers.

T wave delineation

T wave delineation is performed at scale 2^3. The following possible morphologies are handled: positive (+), negative (-), biphasic (+/- or -/+), upward and downward. At each identified QRS-complex, T wave is delineated for the previous beat. The search is done over a window defined as:

$$\Delta W_T = \left\{ n_{QRS_{off}}(i-1) + 80ms\,,\, n_{QRS_{off}}(i-1) + \frac{19 \cdot rr}{32} \right\} \qquad (8.7.1)$$

where $n_{QRS\ off}$ *(i-1)* denotes the sample of the QRS offset of the previous beat (assuming i*th* beat is the latest detected). The T wave dominant peak is searched within a sub-window of ΔW_T:

$$\Delta W_{T_{PK}} = \left\{ n_{QRS_{off}}(i-1) + 80ms\,,\, n_{QRS_{off}}(i-1) + \frac{rr}{2} \right\} \qquad (8.7.2)$$

Within $\Delta W_{T\ PK}$ all zero-crossings are stored. A zero-crossing n_Z is considered to have a positive (negative) *slope* if the first non-zero detail coefficient preceding n_Z is negative (positive), and the first non-zero detail coefficient following n_Z is positive (negative). For zero-crossings n_Z with negative (positive) slopes, the maximum (minimum) value $M_{n\ pre}$ of positive (negative) d^3_n coefficients preceding n_Z is stored, together with the minimum (maximum) value $M_{n\ post}$ of negative (positive) d^3_n coefficients following n_Z. The absolute value of the difference $\Delta_{MM}(n_Z)$ between $M_{n\ pre}$ and $M_{n\ post}$ is computed and the zero-crossing n_Z with the highest value is considered. If an adjacent zero-crossing n^L_Z to the left of n_Z exists and the following condition is met:

$$\Delta_{MM}(n^L_Z) > \frac{51}{64}\Delta_{MM}(n_Z) \qquad (8.7.3)$$

then n^L_Z is marked as T wave dominant peak T_{pk}, n_Z is marked as the end T_{off} of the dominant wave (i.e. the wave whose peak is surrounded by the largest slopes), and the bi-phasic T wave end T_{end} is searched to the right of n_{post} following n_Z. T_{end} is then assigned to the first sample for which d^3_n falls below a threshold ε^3_{Tend} defined as:

$$\varepsilon^3_{T\,end} = \frac{19 \cdot d^3_{n\,post}}{64} \tag{8.7.4}$$

If $n^L{}_Z$ does not exist or (8.7.3) is not verified, n_Z is marked as T_{pk} , and the search proceeds to the right of n_{post} following n_Z. T_{off} is assigned to the first sample for which $d^3{}_n$ falls below a threshold $\varepsilon^3{}_{Toff}$, defined as:

$$\varepsilon^3_{T\,off} = \frac{19 \cdot d^3_{n\,post}}{64} \tag{8.7.5}$$

where n_{post} refers to n_Z. If an adjacent zero-crossing $n^R{}_Z$ exists to the right of n_Z, such that:

$$\Delta_{MM}(n^R_Z) \geq \frac{1}{2}\Delta_{MM}(n_Z) \tag{8.7.6}$$

the T wave is considered to be bi-phasic and T_{end} is defined as the first sample for which $d^3{}_n$ falls below the threshold in (8.4) where n_{post} now refers to $n^R{}_Z$.

Figure 8.8 shows examples of various T wave morphologies from QTDB records, the related manual annotations and the automatic delineation markers.

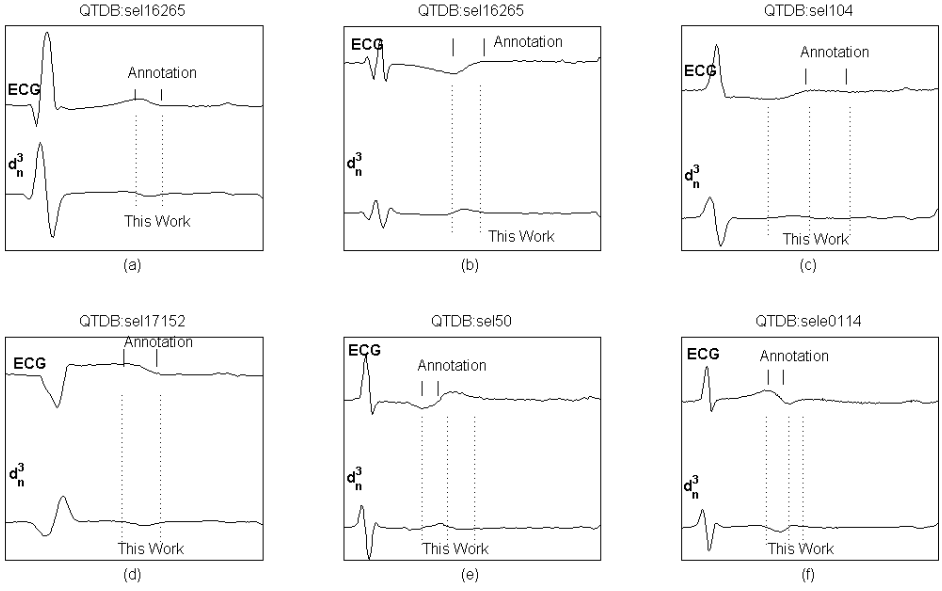

Figure 8.8 Delineation of T wave. Examples of T waves from QTDB records, with manual annotations (top) and delineated characteristic points (bottom): dominant T peak, dominant T offset, T end. (a) positive T wave, (b) negative T wave, (c) upward T wave, (d) downward T wave, (e) and (f) bi-phasic T wave.

8.2.3 Validation

The QRS detection algorithm was validated on manually annotated ECG databases, namely the MIT-BIH Arrhythmia Database (MITDB) and the European ST-T Database

(EDB), whereas the P-QRS-T delineation algorithm was validated on the QT Database (QTDB).

The MITDB database includes a selection of Holter recordings covering a broad spectrum of arrhythmias.

The EDB database contains annotated excerpts of ambulatory ECG recordings with a representative selection of ECG abnormalities including ST segment displacement and cardiac axis shifts.

The QTDB database contains records from MITDB and EDB, and from several other databases (Normal Sinus Rhythm, ST Change, Supraventricular Arrhythmia, Sudden Death, Long Term Recordings). This database was created for validation of waveform boundaries and contains annotations by cardiologists for at least 30 beats per record, including QRS-complex, P, T, U waves delineation.

For the QRS detector validation on MITDB and EDB, the first ECG channel was used and, for MITDB only, raw data were resampled at 250 samples/s before processing.

For the validation on QTDB, reference annotations of first cardiologist (*q1c* files from QTDB) were used in this work. Records from this database are sampled at 250 samples/s, therefore no resampling was required.

Table 8.3 summarizes the databases used for validation.

Table 8.3 – Databases used for validation

Database	#Annotated Beats	Records	Record Duration
MITDB	109010	48	30 min
EDB	788050	90	120 min
QTDB	3622	105	15 min

To assess QRS detection performance, sensitivity (Se) and positive predictive value (P^+) were calculated: Se = TP/(TP+FN) where TP is the total number of true positives identified in the given record, FN is the total number of false negatives; P^+ = TP/(TP+FP) where FP is the total number of false positives.

A true positive is achieved when the time difference between the given annotated beat and the detected beat is not greater than 150 ms, in compliance with ANSI/AAMI-EC57:1998 standard.

For the validation of ECG delineation on QTDB, the metrics proposed in (Boichat *et al.*, 2009; Martinez *et al.*, 2004) were adopted, where m is the mean value of the errors intended as the time difference between automatic and reference annotation, for all annotations, and s is the average standard deviation of the error, calculated by averaging the intra-recording standard deviations.

For each fiducial point delineation, the ECG channel with least error was chosen, as in (Boichat *et al.*, 2009; Martinez *et al.*, 2004). Sensitivity was calculated for each characteristic point, for P wave, T wave and QRS-complex, separately. For T wave, manual annotations T-peak and T-offset, are matched to T_{pk} an T_{off} as defined in the delineation method, respectively.

A true positive is achieved when the wave is annotated and the delineation process detects the presence of such wave within a time distance not greater than 150 ms. In (Boichat *et al.*,

2009) a window of 320 ms is used, in (Martinez *et al.*, 2004) the window size is not reported. A false positive occurs when the delineation process locates a characteristic point which was not annotated. A false negative is considered when the delineation process fails to locate the annotated fiducial point within the above mentioned tolerance of 150 ms. Positive predictive value could not be calculated, as noted in (Martinez *et al.*, 2004): when there is no annotation it is not possible to determine whether the cardiologist considered that there was no waveform to annotate or was not confident in annotating it (perhaps because of the noise level). Nevertheless, for points other than the QRS delineation, P^+ was calculated under the assumption that an absent mark in the annotated beat means that there is no waveform. As a result, the calculated P^+ can be interpreted as a lower limit (P^+_{min}) of the actual one.

8.3 Results

8.3.1 QRS detection

Table 8.4 and Table 8.5 show the QRS detector performance on MITDB and EDB databases, respectively. Results are compared to previous studies. As in (Martinez *et al.*, 2004) segments with ventricular flutter in record 207 of MITDB (for an overall length of approximately 2 min 20 s) and those marked as unreadable (in the pertaining annotation file) in EDB, were excluded.

Table 8.4 – Comparison of QRS Detection Performance (First ECG Channel of MITDB)

QRS Detector	# annotations	FP	FN	*Se* [%]	P^+ [%]
This work	109010	148	252	99.77	99.86
Martinez *et al.,* 2004	109428	153	220	99.80	99.86
Ghaffari *et al.,* 2009	109428	129	101	99.91	99.88
Aristotle (Moody and Mark, 1982)	109428	94	1861	98.30	99.91
Li *et al.,* 1995	104182 (*)	65	112	99.89	99.94
Afonso *et al.,* 1999	90909	406	374	99.59	99.56
Bahoura *et al.,* 1997	109809 (*)	135	184	99.83	99.88
Lee *et al.,* 1996	109481	137	335	99.69	99.88
Hamilton and Tompkins, 1986	109267	248	340	99.69	99.77
Pan and Tompkins, 1985	109809 (*)	507	277	99.75	99.54
Poli *et al.,* 1995	109963	545	441	99.60	99.50
Moraes *et al.,* 2002	N/R	N/R	N/R	99.22	99.73
Hamilton, 2002	N/R	N/R	N/R	99.80	99.80

Inspired by (Martinez *et al.*, 2004), Table 2
(*) a discrepancy was found in the original publication between reported total and record-by-record count
N/R: not reported

Table 8.5 – Comparison of QRS Detection Performance on the European ST-T Database (EDB)

QRS Detector	# annotations	FP	FN	*Se* [%]	P^+ [%]
This work	788050	3511	1483	99.81	99.56
Martinez *et al.*, 2004	787103	4077	3044	99.61	99.48
Aristotle (Moody and Mark, 1982)	787103	10405	38635	95.09	98.63

Inspired by (Martinez *et al.*, 2004), Table 2

8.3.2 ECG delineation

ECG delineation results are shown in Table 8.6, where they are also compared to the ones obtained in previous studies.

Table 8.6 – Comparison of Delineation Performance with Published Methods (QT Database)

Method	Param	P onset	P peak	P offset	QRS onset	QRS offset	T peak	T offset
	# annot	3194	3194	3194	3623	3623	3542	3542
This work	*Se* [%]	98.15	98.15	98.15	100	100	99.72	99.77
	P^+_{min} [%]	91.00	91.00	91.00	N/A	N/A	97.76	97.76
	$m \pm s$	-4.5±13.4	-4.7±9.7	-2.5±13.0	-5.1±7.2	0.9±8.7	-0.3±12.8	1.3±18.6
Martinez *et al.*, 2004	*Se* [%]	98.87	98.87	98.75	99.97	99.97	99.77	99.77
	P^+_{min} [%]	91.03	91.03	91.03	N/A	N/A	97.79	97.79
	$m \pm s$	2.0±14.8	3.6±13.2	1.9±12.8	4.6±7.7	0.8±8.7	0.2±13.9	-1.6±18.1
Laguna *et al.*, 1994	*Se* [%]	97.70	97.70	97.70	99.92	99.92	99.00	99.00
	P^+_{min}[%]	91.17	91.17	91.17	N/A	N/A	97.74	97.71
	$m \pm s$	14.0±13.3	4.8±10.6	-0.1±12.3	-3.6±8.6	-1.1±8.3	-7.2±14.3	13.5±27.0
Boichat *et al.*, 2009 (*)	*Se* [%]	99.87	99.87	99.91	99.97	99.97	99.97	99.97
	P^+_{min} [%]	91.98	92.46	91.70	98.61	98.72	98.91	98.50
	$m \pm s$	8.6±11.2	10.1±8.9	0.9±10.1	3.4±7.0	3.5±8.3	3.7±13.0	-2.4±16.9
$2\sigma_{CSE}$ Tolerance [24]		10.2	-	12.7	6.5	11.6	-	30.6

Partially inspired by (Martinez *et al.*, 2004), Table 3
(*) 16-bit integer implementation. No. annotations not reported. *Se* and P^+_{min} use 320 ms window
N/A: not applicable, N/R: not reported

The results reported by (Ghaffari *et al.*, 2009) are not included in the table because the number of leads used for detection was not stated, nor was the number of annotated beats; it is also unclear the extent to which the authors used third party annotations for validation of their algorithm on the QT Database. The accepted *two-standard-deviations* $2\sigma_{CSE}$ tolerance, defined by the Common Standards for Electrocardiography (CSE) working party in (The CSE Working Party, 1985) based on measurements made on different experts annotations, is also reported in the bottom row of the table. Table 8.7 shows inter-cardiologist annotations variability calculated on the QTDB records that were annotated by two different cardiologists. Unfortunately, only eleven records include double annotations, and only for QRS and T wave, not for P wave.

Table 8.7 – Inter-Cardiologist Annotation Variability on QTDB (Annotation Files: q1c vs. q2c)

	# matched Annotations	Mean Error ± SD [ms]
Q onset	360	-3.12 ± 14.06
T peak	359	-0.28 ± 26.24
T offset	359	-2.99 ± 39.60

8.4 Discussion

The proposed algorithm performs online QRS detection as well as P, QRS, T waves delineation. Unlike previous DWT based methods (Boichat *et al.*, 2009; Li *et al.*, 1995; Martinez *et al.*, 2004), the present only uses two scales (2^2, 2^3), for both QRS detection and ECG delineation. The QRS detection showed an excellent performance on the MIT-BIH Arrhythmia Database, achieving a sensitivity of 99.77% and a positive predictive value of 99.86% on 109010 annotated beats, and on the European ST-T Database, achieving a sensitivity of 99.81% and a positive predictive value of 99.56% on 788050 annotated beats. Sensitivity and positive predictive value reported for the ST-T database are the highest among previous works, as shown in Table 8.5.

The validation on the QT Database showed very good performance in P, QRS, T waves delineation. The mean error (*m*) and the average standard deviation (*s*) were comparable to the ones obtained by other WT-based delineators, as shown in Table 8.6. Mean error (*m*) was lower than 6 ms (1.5 samples, at F_s=250 samples/s) for all characteristic points, whereas the average standard deviation (*s*) was around 8 ms (2 samples) for QRS delineation, and 12 ms (3 samples) for P wave and T peak delineation. Relatively high values of *s* in T wave delineation are present in all algorithms, and may be caused by the difficulty in determining the exact fiducial points as confirmed by the large inter-cardiologist annotation variability, especially for T offset as shown in Table 8.7.

Comparing the average standard deviation (*s*) with the $2\sigma_{CSE}$ tolerances, the condition $s < \sigma_{CSE}$ (referred to in (Martinez *et al.*, 2004) as “strict criterion”) is met for P peak, QRS offset, T offset, whereas the condition $s < 2\sigma_{CSE}$ (referred to in (Martinez *et al.*, 2004) as “loose criterion”) is not met for any of the characteristic points. However, the “strict criterion” is not met by any methods, as shown in Table 8.6.

Sensitivity and positive predictive value of the ECG delineator for P, QRS, T waves were comparable to the values reported by others, as shown in Table 8.6. However, it shall be noted that the width of the search window adopted in the computation of true positives (TP) is not the same for all methods. In (Martinez *et al.*, 2004) the window width was not reported, in (Boichat *et al.*, 2009) it was set to 320 ms. In the present work, the window width was set to 150 ms. As a result, *Se* sand P^+_{min} may not be comparable across different methods.

Previous DWT-based methods (Boichat *et al.*, 2009; Martinez *et al.*, 2004) compute the adaptive thresholds in QRS detection ε^k_{QRS} based on the *root mean square* (RMS) of d^k_n coefficients at the scales of interest. In (Martinez *et al.*, 2004) RMS is computed over $N=2^{16}$

samples excerpts, for the first three scales (2^1, 2^2, 2^3). In (Boichat *et al.*, 2009) RMS is emulated over $N=2^9$ samples excerpts for the first four scales. RMS is computationally demanding, as it requires squaring and summing N coefficients and calculating a square root. Although the square root was emulated in (Boichat *et al.*, 2009), a considerable amount of computations is required for squaring large data excerpts. In the present method, which uses only two scales, all thresholds are calculated from few (local) coefficients, which dramatically reduces the computational effort. In particular, the computation of ε^2_{QRS} by (8.5.3) only requires N=4 data-points, compared to $N=2^9$ in (Boichat *et al.*, 2009) and $N=2^{16}$ in (Martinez *et al.*, 2004), and this computation does not require squaring as in RMS. This observation also applies to ε^3_{QRS}. Moreover, all thresholds are expressed in the linear form of $(A \cdot v)/2^B$, where v is an integer variable (or the sum of integer variables), A and B are positive constant integer values. Thus all thresholds can be computed by elementary shift and add operations.

The ECG data used in this work were either originally sampled at 250 samples/s or resampled accordingly. Although many ECG front-end devices currently on the market offer data streams at 250 samples/s or 256 samples/s, there may be devices that provide a fixed sample rate which is significantly different from 250 samples/s. In order to preserve an integer linear algebra implementation in these cases, depending on the sample rate different scales of the DWT filter bank (8.2) may be used, or the filter bank itself may need to be redesigned, either by using a different order of the spline smoothing function $\theta(t)$, or different scaling and wavelet functions.

8.5 Conclusions

In this paper, a WT-based single-lead ECG delineation algorithm, designed for online 32-bit integer linear algebra processing, with shift/add operations replacing multiplications and divisions, was presented. The algorithm complies with a sample resolution up to 24-bit/sample without any assumptions on the amplitude resolution of the ECG signal.

The algorithm detects the QRS-complex, delineates the onset, peak, and offset of the mono- or bi-phasic P wave, the onset and offset of the QRS-complex, the dominant peak and offset of the mono- or bi-phasic T wave.

The QRS detector achieved excellent performance on the MIT-BIH Arrhythmia database (*Se*=99.77%, P^+=99.86%, 109010 annotated beats) and on the European ST-T Database, (*Se*=99.81%, P^+=99.56%, 788050 annotated beats).

The proposed algorithm also exhibited very good accuracy in P, QRS, T delineator on QT Database, where the mean error between automatic and manual annotations was lower than 1.5 samples for all the characteristic points, and the associated average standard deviations were comparable to the ones reported from previous methods. However, the QTDB database contains a limited number of annotations, which makes the validation of an automatic ECG delineator not comprehensive.

Based on the results achieved on standard databases, the proposed algorithm exhibits reliable QRS detection as well as accurate ECG delineation. Reliability and accuracy are close to the highest among the ones obtained in other studies, in spite of a simplified structure built on integer linear algebra which makes the proposed algorithm a suitable candidate for online QRS detection and ECG delineation under strict power constraints and limited computational resources, such as in wearable devices for long-term non-diagnostic ambulatory monitoring.

References

Addison P: Wavelet transforms and the ECG: a review. *Physiol Meas* 2005; 26:155–199.

Afonso VX, Tompkins WJ, Nguyen TQ, Luo S: ECG beat detection using filter banks. *IEEE Trans Biomed Eng* 1999; 46:192–201.

Bahoura M, Hassani M, Hubin M: DSP implementation of wavelet transform for real time ECG wave forms detection and heart rate analysis. *Comput Meth Programs Biomed* 1997; 52:35–44.

Boichat N, Khaled N, Rincon F, Atienza D: Wavelet-based ECG delineation on a wearable embedded sensor platform. *Proc 6th IEEE Int Workshop on Body Sensor Networks* 2009; 256–261.

Bowers EJ, Murray A, Langley P: Respiratory rate derived from principal component analysis of single lead electrocardiogram. *Comput Cardiol* 2008; 35:437–440.

Causse M, Sénard JM, Démonet JF , Pastor J: Monitoring cognitive and emotional processes through pupil and cardiac response during dynamic versus logical task. *Appl Psychophysiol Biofeedback* 2010; 35:115–123.

Clifford GD, Azuaje F, McSharry PE: *Advanced methods and tools for ECG data analysis* Ed. Artech House 2006; pp. 55–57.

Corrado D *et al.*: Recommendations for interpretation of 12-lead electrocardiogram in the athlete. *Eur Heart J* 2010; 31:243–259.

Fairweather JAA, Johnston P, Luo S, Macfarlane PW: Computer analysis of implanted cardiac pacemaker rhythm. *Comput Cardiol* 2007; 34:193–196.

Figueiredo CP, Becher K, Hoffmann KP, Mendes PM: Low power wireless acquisition module for wearable health monitoring systems. *Conf Proc IEEE Eng Med Biol Soc* 2010; 1:704–7.

Ghaffari A, Homaeinezhad MR, Akraminia M, Atarod M, Daevaeiha M: A robust wavelet-based multi-lead Electrocardiogram delineation algorithm. *Med Eng Phys* 2009; 31:1219–27.

Hamilton P: Open source ECG analysis. *Comput Cardiol* 2002; 29:101–104.

Hamilton PS, Tompkins W: Quantitative investigation of QRS detection rules using the MIT/BIH arrhythmia database. *IEEE Trans Biomed Eng* 1986; 33:1157–1165.

Healey JA, Picard RW: Detecting stress during real-world driving tasks using physiological sensors. *IEEE Trans Intell Transp Syst* 2005; 6:156–166.

Higgins JP: Normal resting electrocardiographic variants in young athletes. *Phys. Sportsmed.* 2008; 36:69–75.

Hooper GS, Yellowlees P, Marwick TH, Currie PJ, Bidstrup BP: Telehealth and the diagnosis and management of cardiac disease. *J Telemed Telecare* 2001; 7:249–56.

Laguna P, Jané R, Caminal P: Automatic detection of wave boundaries in multilead ECG signals: Validation with the CSE database. *Comput Biomed Res* 1994; 27:45–60.

Lee J, Jeong K, Yoon J, Lee M: A simple real-time QRS detection algorithm. *Proc 18th Ann Int Conf IEEE Engineering in Medicine and Biology Soc* 1996; pp. 1396–1398.

Li C, Zheng C, Tai C: Detection of ECG characteristic points using wavelet transforms. *IEEE Trans Biomed Eng* 1995; 42: 21–28.

Mallat SG: A theory for multiresolution signal decomposition: the wavelet representation. *IEEE Trans Pattern Anal Machine Intell* 1989; 11:674–693.

Mallat S: Zero-crossings of a wavelet transform. *IEEE Trans Inform Theory* 1991; 37:1019–1033.

Mallat SG, Zhong S: Characterization of signals from multiscale edges. *IEEE Trans Pattern Anal Machine Intell* 1992; 14:710–732.

Martinez J, Almeida R, Olmos S, Rocha A, Laguna P: A wavelet-based ECG delineator: evaluation on standard databases. *IEEE Trans Biomed Eng* 2004; 51:570–581.

Moody GB, Mark RG: Development and evaluation of a 2-lead ECG analysis program. *Comput Cardiol* 1982; 4:39–44.

Moraes J, Freitas M, Vilani F, Costa E: A QRS complex detection algorithm using electrocardiogram leads. *Comput Cardiol* 2002; 29:205–208.

Mutikainen S, Rantanen T, Alén M, Kauppinen M, Karjalainen J, Ortega-Alonso A, Kaprio J, Kujala UM: Electrocardiographic and other clinical correlates of walking ability in older women. *Arch Gerontol Geriatr* 2009; 51:216–21.

Pan J, Tompkins WJ: A real-time QRS detection algorithm. *IEEE Trans Biomed Eng* 1985; 32:230–236.

Poli R, Cagnoni S, Valli G: Genetic design of optimum linear and nonlinear QRS detectors. *IEEE Trans Biomed Eng* 1995; 42:1137–1141.

Porges SW, Byrne EA: Research methods for measurement of heart rate and respiration. *Biol Psychol* 1992; 34:91–130.

Sivannarayana N, Reddy DC: Biorthogonal wavelet transforms for ECG parameters estimation. *Med Eng Phys* 1999; 21:167–174.

Sovilj S, Jeras M, Magjarevic R: Real time P-wave detector based on wavelet analysis. *Proc 12th IEEE Mediterranean Electrotechnical Conf* 2004; 1:403–406.

The CSE Working Party: Recomendations for measurement standards in quantitative electrocardiography. *Eur Heart J* 1985; 6:815–825.

Chapter 9: Time-frequency Analysis of Atrial Fibrillation Comparing Morphology-clustering Based QRS-T Cancellation with Blind Source Separation in Multi-lead Surface ECG Recordings

Abstract

To separate the atrial (AA) from the ventricular (VA) electrical activity in surface ECG recordings of atrial fibrillation (AF), various methods have been proposed, such as QRS-T cancellation by beat-averaged template subtraction, and blind source separation (BSS). Although QRS-T cancellation is computationally more efficient than BSS, and allows the preservation of spatial information, it is sensitive to morphology changes, which produce large residuals in AA, biasing the frequency analysis.

Aim of this study was: (i) to propose an improved approach to VA cancellation based on k-means morphology clustering (MC); (ii) to validate its ability to estimate AF dominant frequency (DF) on a standard database with intra-cardiac and surface ECG recordings (IAFDB, Physionet.org); (iii) to compare the temporal evolution of the spectral content of MC-estimated AA (MC-AA) with the one obtained from a reference BSS method based on Independent component analysis (ICA) and second-order blind identification (SOBI), in 14 body surface potential map (BSPM) recordings.

QRS-T amplitude in MC-AA was significantly lower ($p<0.001$) than in ECG (in closest BSPM channel to V1).

The validation on IAFDB showed no significant difference in DF estimation ($p=0.546$) in 17 recordings. Also no significant difference in DF estimation ($p=0.208$) with respect to the reference BSS method was observed.

The proposed QRS-T cancellation method effectively suppresses VA and accurately estimates DF compared to an established BSS method.

9.1 Introduction

Atrial fibrillation (AF) is a common cardiac arrhythmia affecting between 2% and 10% of people over 50 years of age (Fuster *et al.*, 2001). AF is a major cause of morbidity and mortality in the elderly population where the risk of stroke is five times higher (Langley *et al.*, 2006). For this reason an increasing clinical research interest has been devoted to AF in recent years (Bollmann *et al.* 2006; Rieta *et al.*, 2004).

Methods reported in literature to cancel VA from the ECG involve direct suppression of the QRS complex and the T-wave by subtracting a fixed template obtained by averaging consecutive beats (BA). It relies on the fact that AF is uncoupled to the ventricular activity, thus subtracting an averaged QRS-T segment from the ECG produces a residual signal which closely represents AF (Bollmann *et al.*, 2006; Langley *et al.*, 2006; Stridh and Sörnmo, 2001). Unfortunately, since average beat subtraction is performed on individual leads, this process is sensitive to alterations in the electrical axis, which produces large QRS-related residuals in AA (Bollmann *et al.*, 2006) which in turn affect its spectral content. Another approach to AA extraction is based on the hypothesis that AA and VA originate from statistically separable sources (Bollmann *et al.*, 2006; Langley *et al.*, 2006), which may be treated by blind source separation (BSS) methods, when multi-lead surface ECG recordings are available. Independent component analysis (ICA) has successfully been adopted (Bollmann *et al.*, 2006; Rieta *et al.*, 2004) and improved with second order blind identification (SOBI) (Castells *et al.*, 2005), as well as principal component analysis (PCA) (Langley *et al.*, 2006).

A recording length of at least 10 s is required for adequate computation of the average beat in QRS-T cancellation, whereas the recording length can be shorter in BSS (Bollmann *et al.*, 2006). However, BSS only allows the derivation of a global atrial signal with contributions from all leads, which limits its spatial resolution (Bollmann *et al.*, 2006). On the other hand, QRS-T cancellation is computationally more efficient than BSS, and allows the preservation of spatial information from individual leads.

The aim of this study is threefold: (i) to propose an improved approach to VA cancellation based on a k-means morphology clustering criterion; (ii) to validate its ability to estimate DF on a standard database with simultaneous intra-cardiac and surface ECG recordings (Intracardiac Atrial Fibrillation Database, Physionet.org); (iii) to compare the temporal evolution of the spectral content of MC estimated AA (MC-AA) with the one obtained from a reference BSS method based on ICA-SOBI (ICA-AA), in 14 body surface potential map (BSPM) recordings.

9.2 Methods

9.2.1 Data acquisition

Fourteen recordings of 67-lead surface ECG (64-thoracic, three bipolar limb leads) from fourteen male patients with AF (age 60±9 years) were considered for this study, each 3 minutes in duration.

The surface ECG data were recorded by Biosemi ActiveTwo™ (Biosemi, Amsterdam, NL) at a sampling rate of 2048 samples/s, 24-bit/sample.

9.2.2 ECG processing

The ECG signal was processed offline in MATLAB® (The Mathworks, Natick, Massachusetts, USA).

The ECG was band-pass filtered (3-dB pass-band: 0.5-100 Hz) and then down-sampled to 250 samples/s for beat detection. An established discrete-wavelet transform based method (Di Marco and Chiari, 2011) was used for beat detection.

9.2.3 QRS-T clustering

For the ith detected beat, a QRS-T window was defined as:

$$\begin{aligned}
&T_1(i) = QRS_{PK}(i) - \Delta_{80} \\
&QTc_{REF} = \Delta_{440} \\
&T_2(i) = T_1(i) + QTc_{REF} \cdot \sqrt{RR_{MEAN}} \\
&W_{QRST}(i) = \{T_1(i), T_2(i)\}
\end{aligned} \tag{9.1}$$

where $QRS_{PK}(i)$ is the fiducial point (i.e. dominant peak) of the *i*th beat, Δ_{80} is a time delta of 80 ms, QTc_{REF} is an empirical reference value of QTc (Bazett) set to 440 ms, and RR_{MEAN} is the mean RR interval duration (in units of seconds) of the entire recording.

A QRS-T collection matrix *B* can be constructed, whose columns are the ECG samples of $W_{QRST}(i)$, i=1,...,M, where *M* is the number of detected beats.

Rows of *B* are treated as *N* observations of an *M*-dimensional variable. *k-means* clustering is performed using correlation distance: $d_{CORR}(x_n, x_m) = 1 - \rho(x_n, x_m)$ as dissimilarity criterion. Collected beats are grouped according to the dissimilarity metrics to form the columns of the starting guess matrix to initialize the *k-means* clustering process.

9.2.4 Blind source separation

An extensive description of the ICA-SOBI approach to BSS of AA is given in (Castells *et al.*, 2005).

In the present study a subset of 14 channels was chosen from the anterior BSPM map as sensor variables for ICA-SOBI, including the top-central portion of the right-anterior torso, as shown in Figure 9.1. This choice includes CH15 (closest to V1 in 12-lead ECG) where the atrial activity is prominent. ICA (JADE implementation) and subsequent SOBI were then performed, as suggested in (Castells *et al.*, 2005). Spectral concentration (SC) was adopted to select the source representing AA (source with highest SC):

$$\begin{aligned}
&SC(S_k) = \frac{\sum_{f=0.82\cdot f_P}^{1.17\cdot f_P} \Gamma_{S_k}(f_i)}{\sum_{f=0}^{F_S/2} \Gamma_{S_k}(f_i)} \\
&f_P = \arg \max_{f \in (3.5-10Hz)} (\Gamma(f_i))
\end{aligned} \tag{9.2}$$

where S_k is the *k*th estimated source, Γ_{Sk} is the power spectral density (PSD) of the *k*th source, f_P is the peak frequency in the frequency band of AF: 3.5 – 10 Hz, namely DF.

9.2.5 Time-frequency analysis of AA

The AA signal (MC-AA and ICA-AA) was divided into consecutive non-overlapping 20 s windows and PSD (Welch periodogram, Hamming window, 50% overlap, frequency resolution: 0.24 Hz) was computed for each.

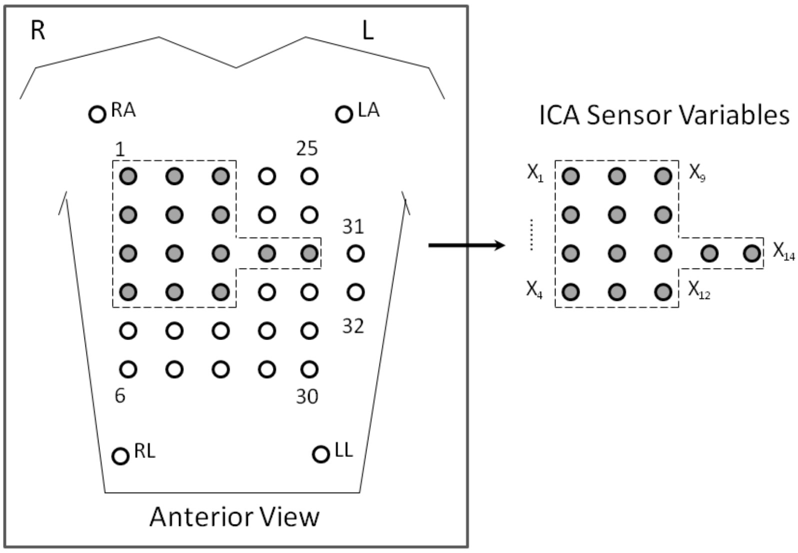

Figure 9.1 32-channel anterior view of BSPM. Dotted region indicates chest electrodes used for ICA.

9.2.6 Validation on standard database

The *Intracardiac Atrial Fibrillation Database* (IAFDB) from Physionet (www.physionet.org) was adopted for validation of MC estimation of DF.

Recordings whose intracardiac signals would allow reliable peak-detection were considered (n=17). Each recording was divided into consecutive non-overlapping 20 s windows. For each, MC-AA was extracted from lead V1 and DF estimated as the dominant peak frequency of PSD. The actual atrial fibrillatory rate (AAFR) was calculated as the inverse of the mean interval between consecutive peaks within the 20 s window.

9.3 Results

9.3.1 VA cancellation

Figure 9.2 shows MC compared to BA in VA cancellation.

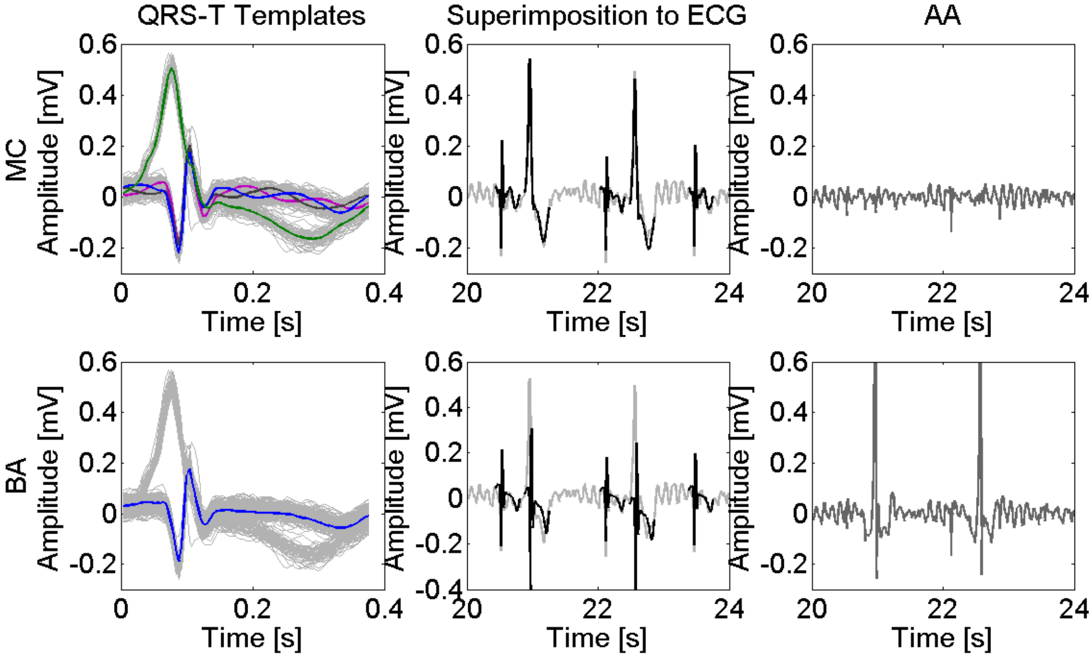

Figure 9.2 MC (top panels) compared to BA in VA cancellation.

Table 9.1 – VA cancellation: comparison of MC and BA.

		AA QRS-T Amplitude [μV]		
#Rec	#Cluster	MC	BA	*p value*
r1	17	224(98)	307(113)	*p<0.001*
r2	1	250(185)	244(180)	*N.S.*
r3	4	617(432)	708(120)	*p<0.001*
r4	1	192(86)	195(84)	*N.S.*
r5	1	274(183)	276(190)	*N.S.*
r6	5	141(123)	193(1167)	*p<0.001*
r7	11	424(492)	424(489)	*N.S.*
r8	11	161(60)	196(70)	*p<0.001*
r9	11	280(115)	349(160)	*p<0.001*
r10	1	224(199)	226(194)	*N.S.*
r11	1	326(265)	327(266)	*N.S.*
r12	1	262(226)	267(233)	*N.S.*
r13	3	302(111)	335(102)	*p<0.001*
r14	5	543(333)	610(507)	*p<0.01*

N.S. = not significant

Table 9.1 shows comparison between MC and BA in QRS-T cancellation (Median(inter-quartile range) is reported). In all cases for which multiple templates were generated (rows with #Cluster>1) there was a significant improvement (Wilcoxon rank-sum test (WRT), α=0.05) in QRS-T cancellation in MC with respect to BA.

Table 9.2 shows cumulative data analysis of QRS-T amplitude in MC-AA with respect to ECG in CH15. MC significantly reduces QRS-T amplitude with respect to ECG, though the ECG amplitude in the TQ segment remains significantly higher than that of MC-AA in the QRS-T, indicating that MC does not “over-cancel”.

Table 9.2 – QRS-T cancellation: cumulative data analysis

Amplitude [μV]				
QRS-T MC	QRS-T ECG	*p value*	TQ ECG	*p value*
260(223)	1239(1096)	*p<0.001*	194(188)	*p<0.001*

9.3.2 DF estimation

DF estimation difference (Δ_{DF}) is shown in Table 9.3 (Median(inter-quartile range) is reported). Statistical analysis (WRT, α=0.05) is presented for the two datasets: standard database (IAFDB) and experimental data (14 BSPM recordings). To compare DF estimation to ICA, MC-AA from the lead maximizing SC was selected. In both datasets the median value of Δ_{DF} is below the frequency resolution (0.24 Hz) used in PSD computation.

Table 9.3 – DF Estimation. Median(inter-quartile range)

	Δ_{DF} [Hz]	
	MC vs. AAFR	*p value*
IAFDB	0.03(0.37)	*N.S.(p=0.546)*
	MC vs. ICA	
14 Recordings	0.00(0.49)	*N.S.(p=0.208)*

N.S. = not significant

9.3.3 Time-frequency analysis

Figure 9.3 shows an example of PSD evolution for recordings r1 through r4.

Figure 9.4 shows an example of the spatio-temporal evolution of PSD for recording r. SC is higher (DF most prominent) in the right side of the torso.

Table 9.4 shows statistical analysis (WRT, α=0.05) of SC for the two methods (Median(inter-quartile range) reported). SC in ICA is significantly different (higher) from MC in 7 of 14 recordings, which according to (Castells *et al.*, 2005) may indicate higher performance (reliability) in the extraction of AA.

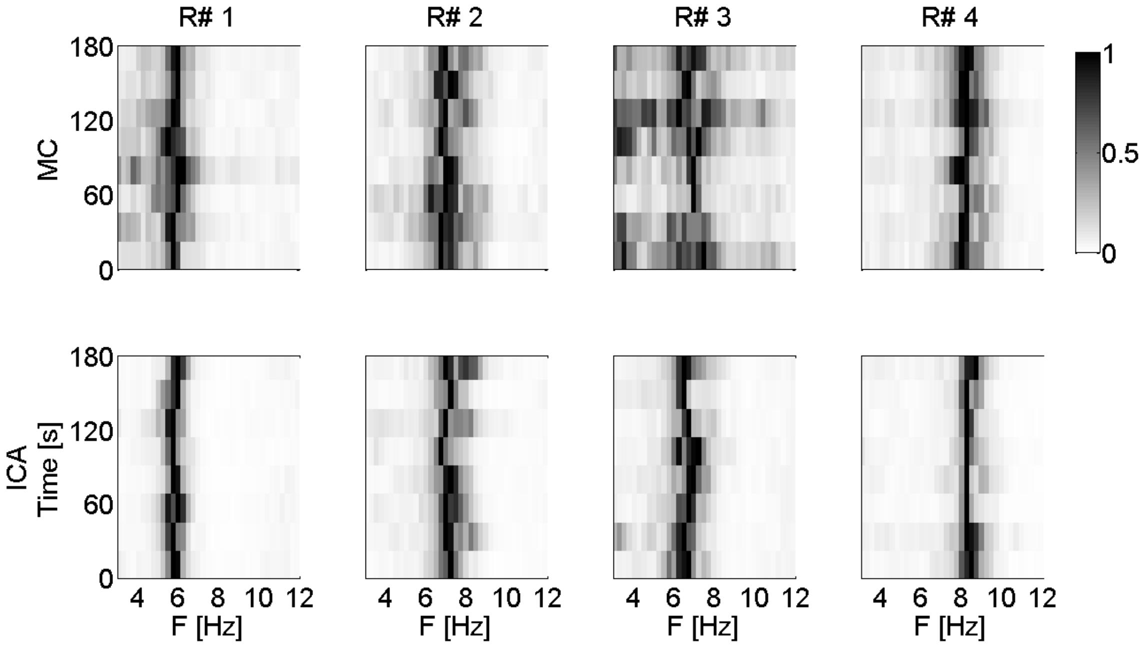

Figure 9.3 Normalized PSD temporal evolution of MC-AA (top panels) and ICA-AA.

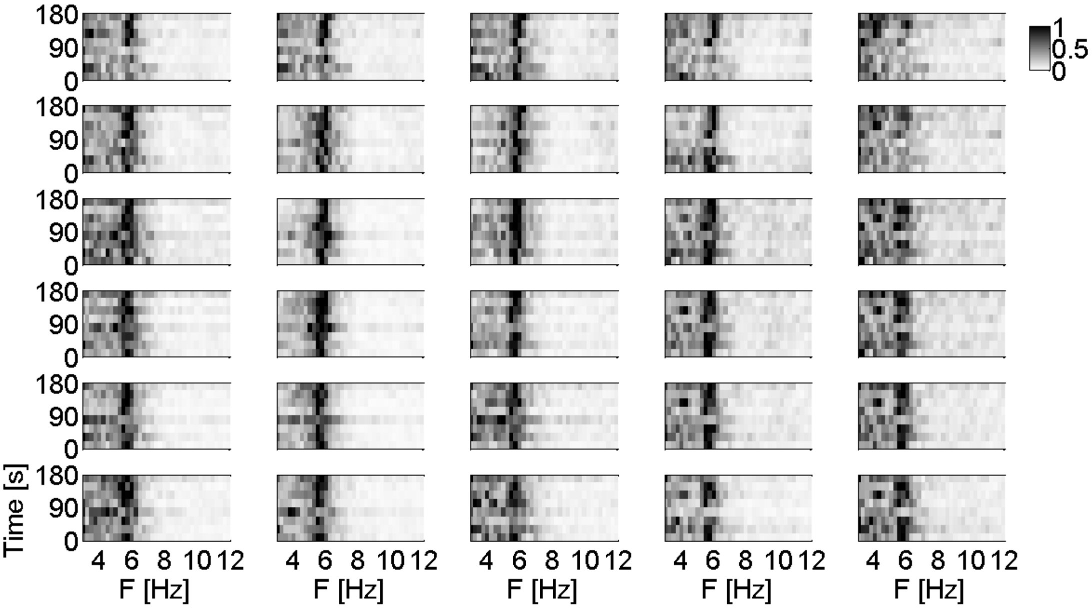

Figure 9.4 Spatio-temporal evolution of normalized PSD for recording r1, for the first 30 BSPM channels (following the order displayed in Figure 9.1).

Table 9.4 – SC: comparison of MC and ICA.

#Rec	SC [%] MC	SC [%] ICA	*p value*
1	57.5(6.4)	80.9(4.7)	*p<0.01*
2	58.8(3.9)	70.5(8.0)	*p<0.01*
3	61.7(9.0)	67.8(11.2)	*N.S.*
4	30.4(8.3)	61.6(5.9)	*p<0.005*
5	63.7(6.3)	60.7(16.4)	*N.S.*
6	53.2(7.9)	60.5(6.9)	*N.S.*
7	40.1(4.5)	56.0(23.7)	*N.S.*
8	48.7(9.0)	55.3(9.3)	*N.S.*
9	31.2(9.4)	51.9(6.2)	*p<0.01*
10	34.3(4.4)	43.5(6.2)	*p<0.01*
11	29.6(9.9)	38.0(6.6)	*p<0.01*
12	30.2(9.1)	33.0(3.6)	*N.S.*
13	20.3(3.3)	32.0(4.6)	*p<0.01*
14	28.4(4.3)	29.3(6.2)	*N.S.*
Average	39.5(27.2)	54.4(26.6)	*p<0.001*

9.4 Discussion and conclusions

A multi-template clustering based approach to VA cancellation (MC) was presented. The proposed method showed significant improvement (p<0.001) in VA cancellation with respect to “beat-averaging” approach in BSPM recordings for which multiple templates were generated (no significant difference in the others).

The validation on a standard database (IAFDB, Physionet) showed no significant difference in DF estimation (p=0.546) in 17 recordings.

The proposed method also showed no significant difference in DF estimation with respect to ICA in BSPM recordings (p=0.208) in spite of significantly lower SC (p<0.001). However, replication on a larger dataset (including multifocal ectopies) is required to confirm these results.

VA cancellation by MC allows spatial localization of time-frequency distribution of DF, as shown in Figure 9.4 where frontal-right channels exhibit a marked DF pattern. This degree of spatial resolution may only be achieved by single-lead source cancellation methods, which on the other hand suffer from VA residuals, as shown by significantly lower SC with respect to BSS methods.

References

Bollmann A, Husser D, Mainardi L, Lombardi F, Langley P, Murray A, Rieta JJ, Millet J, Olsson SB, Stridh M, Sörnmo L. Analysis of surface electrocardiograms in atrial fibrillation: techniques, research, and clinical applications. *Europace* 2006; 8:911–926.

Castells F, Rieta JJ, Millet J, Zarzoso V. Spatiotemporal blind source separation approach to atrial activity estimation in atrial tachyarrhythmias. *IEEE Trans Biomed Eng* 2005; 52:258–267.

Di Marco LY, Chiari L. A wavelet-based ECG delineation algorithm for 32-bit integer online processing. *Biomed Eng Online* 2011;10:23.

Fuster V, *et al.* ACC/AHA/ESC guidelines for the management of patients with atrial fibrillation: A report of the American college of cardiology/American Heart Association task force on practice guidelines and the european society of cardiology committee for practice guidelines and policy conferences (Committee to develop guidelines for the management of patients with atrial fibrillation). *Eur Heart J* 2001; 22:1852–1923.

Langley P, Rieta JJ, Stridh M, Millet J, Sörnmo L, Murray A. Comparison of Atrial Signal Extraction Algorithms in 12-lead ECGs with atrial fibrillation. *IEEE Trans Biomed Eng* 2006; 53:343–346.

Rieta JJ, Castells F, Sanchez C, Zarzoso V, Millet J. Atrial activity extraction for atrial fibrillation analysis using blind source separation. *IEEE Trans Biomed Eng* 2004; 51:1176–1186.

Stridh M, Sörnmo L. Spatiotemporal QRST Cancellation Techniques for Analysis of Atrial Fibrillation. *IEEE Trans Biomed Eng* 2001; 48:105–111.

Chapter 10: Spatial complexity and spectral distribution variability of atrial activity in surface ECG recordings of atrial fibrillation

Abstract

Considerable research effort has been devoted to the estimation of the degree of organization of atrial fibrillation (AF), to potentially support clinical decision making.

The aims of this study were to: *i)* analyse the temporal variability of spatial organization (complexity) and spectral distribution of AF in body surface potential maps (BSPM), proposing an automated implementation of the analysis; ii) assess the applicability to reduced lead-sets.

Twenty one persistent AF recordings of three minutes each (64 BSPM: 32 anterior, 32 posterior) were analysed. The relationship between spatial organisation (C) and its variability (CV) was quantified on automatically delineated TQ segments. The relationship between spectral concentration (SC) and spectral variability (SV) was quantified on the atrial activity (AA) extracted using principal component analysis. Three different lead-sets: 64, 32 anterior, and 10 anterior channels were considered.

Significant ($p<0.001$) correlation (ρ) was found: $\rho(CV, C) \geq 0.80$, $\rho(SC, SV) \leq -0.83$ for all lead-sets. The results suggest that a higher degree of spatial organization is associated with reduced variability of spatial organization over time, and lower spectral variability associated with more prominent spectral peak in the AF frequency band (4-10 Hz).

10.1 Introduction

During atrial fibrillation (AF), uncoordinated electrical wavefront patterns propagate through the atria, resulting in an irregular heart rhythm disturbance characterized by the lack of relationship between consecutive beats (Bonizzi *et al.*, 2010; Sih *et al.*, 1999). A long-standing hypothesis on the aetiology of this phenomenon was introduced in the early 1960s by Moe and co-workers (Moe and Abildskov, 1959; Moe *et al.*, 1964) who proposed the “multiple wavelet” theory, postulating that the persistence of atrial fibrillation depends on the average number of re-entering wavelets in the atria. According to this theory, the number of circulating wavelets is inversely related to the probability of their spontaneous and simultaneous termination, and directly related to the likelihood of AF persistence (Moe and Abildskov, 1959; Moe *et al.*, 1964; Wijffels *et al.*, 1995). Konings and co-workers (Konings *et al.*, 1994) classified patterns of human right atrial activation during electrically-induced AF in three categories, based on the complexity of atrial activation. Increasing AF frequency and irregularity was associated with increasing incidence of continuous electrical activity and re-entry. Further studies on intra-atrial electrograms in humans have provided evidence that atrial activation in AF is not entirely random (Censi *et al.*, 2000; Gerstenfeld *et al.*, 2000;

Richter *et al.*, 2011). Gerstenfeld and co-workers (Gerstenfeld *et al.*, 2000) have demonstrated the tendency for wave fronts to follow paths of previous excitation leading to transient similarities in the direction of wave propagation. Censi and co-workers (Censi *et al.*, 2000) detected spatiotemporal recurrent patterns in bipolar intra-atrial electrograms recordings from 19 subjects with chronic AF, suggesting that during AF a certain degree of local organization may exist, caused by deterministic mechanisms of activation. Richter and co-workers (Richter *et al.*, 2011) identified propagation patterns in intracardiac signals recorded during AF using partial directed coherence, a method that evaluates directional coupling between multiple signals in the frequency domain.

As a corollary to the wavelet theory, these findings suggest the presence of local organization, inversely related to the number of re-entering wavelets wandering throughout the atrial tissue, and directly related to the likelihood of AF spontaneous termination (Alcaraz and Rieta, 2010; Sih *et al.*, 1999).

Motivated by the potential clinical relevance in their support to AF treatment, further studies have been conducted in recent years with the goal of providing automatic algorithms for computer-aided evaluation of local organization of atrial activation in AF. Alcaraz and Rieta (Alcaraz and Rieta, 2009; Alcaraz and Rieta, 2010) proposed the use of sample entropy (SampEn) a non-linear regularity index to assess AF organization non-invasively from the electrocardiogram (ECG).

Konings and co-workers (Konings *et al.*, 1994) showed a positive correlation between atrial activation complexity and fibrillatory rate from intra-cardiac recordings. Bollman and co-workers (Bollmann *et al.*, 2006) suggested that analysis of non-invasively estimated atrial activity (AA) signals can be exploited, as the fibrillatory frequency of the AA is inversely related to the length of the averaged atrial fibrillatory cycle, and can be viewed as an index of average atrial refractoriness and AF organization. Asano and co-workers (Asano *et al.*, 1992) induced AF in patients undergoing an electrophysiological study and reported a significantly lower fibrillatory frequency in those where AF terminated spontaneously with respect to the others.

To complement the analysis of organized patterns in AF, alongside the temporal and spectral characterization, studies have addressed the spatial organization (or complexity). Adopting principal component analysis (PCA) as a measurement of spatial organisation on bipolar intra-cardiac recordings, Faes and co-workers (Faes *et al.*, 2001) found that atrial activation in AF could be described by a reduced number of principal components for more organized AA. Also based on PCA, Bonizzi and co-workers (Bonizzi *et al.*, 2010) recently proposed an automated non-invasive method for the assessment of the spatio-temporal organization of AA during AF, utilizing body surface potential maps (BSPM). In addition to its use as a measure of spatial organisation, PCA has also been validated as a tool to extract AA from the ECG (Langley *et al.*, 2006; Raine *et al.*, 2004; Raine *et al.*, 2005). Another well established source separation approach to atrial signal extraction from surface ECG is based on independent component analysis (ICA) (Castells *et al.*, 2005). However, both ICA and PCA approaches separate the atrial from ventricular source signals, and have been shown to produce similar performance (Langley *et al.*, 2006) in spite of substantially different modes of processing the ECG signal (Bollmann *et al.*, 2006).

The aims of this study were to: *i)* analyse the variability of spatial organization (complexity) and spectral distribution of AF in BSPM, proposing an automated implementation of the analysis; ii) assess the applicability to reduced lead-sets, with the goal of potentially supporting clinical decision making in AF treatment.

10.2 Methods

10.2.1 Data recordings

Twenty one non-invasive surface ECG recordings of AF (AF1... AF21), of three minutes each (64 BSPM: 32 anterior, 32 posterior), from twenty one patients (Age: 57±11) were considered for this study. All participants gave informed consent. The study was granted ethical approval by the NHS Research Ethics Committee, and was conducted in accordance with the ethical standards stated in the 1964 Declaration of Helsinki.

10.2.2 Body surface potential maps

The electrode map adopted for BSPM is shown in Figure 10.1. The horizontal inter-electrode distance was 6 cm, the vertical was 5 cm.

The BSPM also included limb-electrodes indicated in Figure 10.1 with the standard labeling (LA, RA, LL, RL). The ECG was acquired at a sample rate of 2048 samples/s, 24 bit/sample, with a sample resolution of 0.03 µV/LSB and pass-band of 0.05–500 Hz.

10.2.3 Pre-processing

The Wilson's central terminal (WCT) potential was calculated from the BSPM limb-electrodes and subtracted from the chest electrode potentials, to obtain 64 BSPM chest leads (anterior: CH1... CH32, posterior: CH33... CH64). The ECG recordings were band-pass filtered to a 3dB cut-off pass-band of 0.5–100 Hz to reduce baseline wander effects (lower cut-off frequency) and high frequency noise such as myoelectric artifacts, and down-sampled to F_S = 250 samples/s to comply with the ECG delineation algorithm described in the following section.

Three lead-sets were considered, with the goal of evaluating the feasibility of the analysis on reduced sets: 64 BSPM channels (LS_1), 32 BSPM anterior leads (LS_2), and a subset of 10 leads (LS_3) consisting of three bipolar limb leads ("modified" Lead I, II, III), three augmented limb leads (aVR, aVF, aVL) and four chest leads (CH15, CH21, CH28, CH32: close to V1, V2, V4, V5, respectively), as shown in Figure 10.1. Lead-set LS_3 was intended as the closest approximation to the standard 12-leads ECG that the available electrodes would allow.

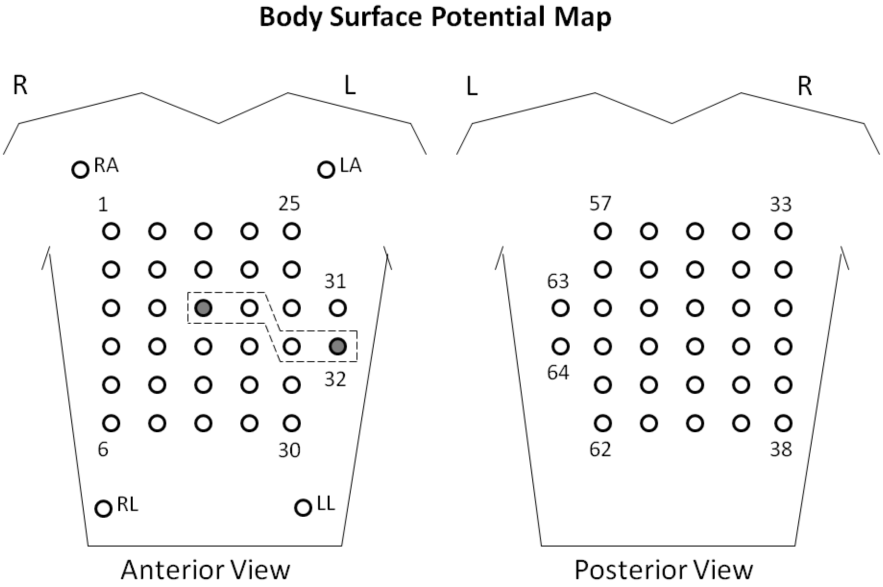

Figure 10.1 Body surface potential map layout: chest anterior (left) and posterior (right) view. Dashed shape delimits subset of chest leads used in LS_3. Channel 15 of anterior view (close to V1 position) and channel 32 (close to V5 position) are shaded. LA = left arm, RA = right arm, LL = left leg, RL = right leg.

10.2.4 Principal component analysis

PCA has been applied in recent years for the analysis of organization of atrial activation through the measurement of the cumulative variance of the PCs (Bonizzi *et al.*, 2010; Faes *et al.*, 2001). Furthermore, PCA is also a method of extracting the AA by suppression of the ventricular activity, allowing analysis of the continuous atrial component of the ECG (Bollmann *et al.*, 2006; Langley *et al.*, 2006; Raine *et al.*, 2004; Raine *et al.*, 2005). In the present study we exploited both these applications of PCA: firstly to quantify AF organization in TQ sections of the ECG where the AA can be readily seen without obscuring ventricular activity; and secondly, to extract the continuous AA from which subsequent spectral variability analysis was undertaken.

PCA is based on an orthogonal linear transformation of N observations of M random variables ($N \geq M$), resulting in uncorrelated output variables, namely the principal components, which are ordered in descending order of variance.

Considering N consecutive time samples (observations) for a generic set of M ($<N$) leads $l_1 \ldots l_M$, the vector $X^{(l_j)} = [X_{l_j}(1) \ldots X_{l_j}(N)]^T$ where $[\cdot]^T$ is the transpose operator, for lead l_j, $j=1 \ldots M$, can be viewed as N observations of a random process, which may be assumed to have zero-mean without loss of generality. PCA transformation may be written as:

$$PC_i(k) = \sum_{j=1}^{M} A_{i,j} \cdot X_{l_j}(k) \qquad (10.1)$$

where PC*i* is the i*th* principal component, *k* is the time sample index (k=1,... N), *A* is an *M*x*M* orthogonal matrix whose rows are the eigenvectors of the (estimated) covariance matrix R_X = E[X·X^T], where E[·] is the expected value operator, and X = [$X^{(l1)}$ ... $X^{(lM)}$] is the *N*x*M* observation matrix of the random process.

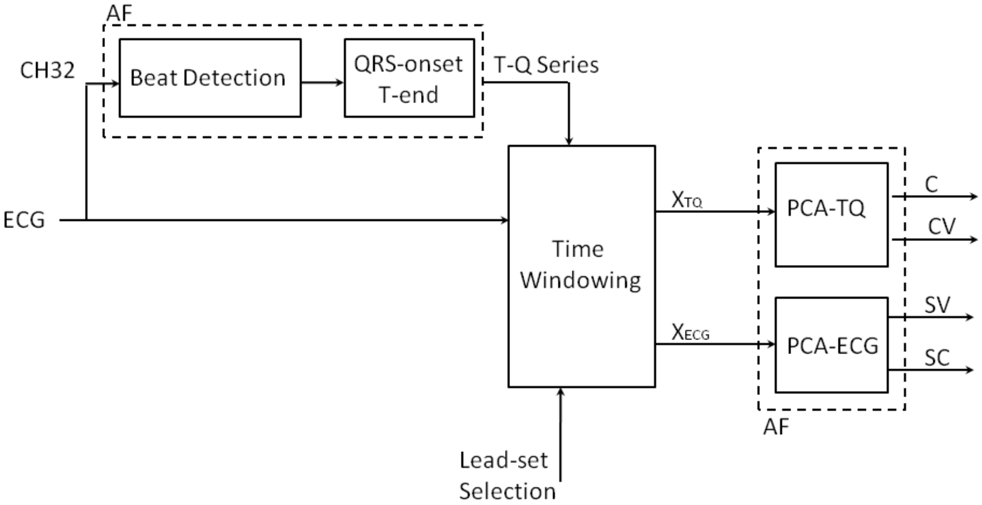

Figure 10.2 Block diagram of the automated process generating the indices. X_{TQ}, and X_{ECG} are the N_{TQ}x*M*, and N_{ECG}x*M* observation matrices generated by the time windowing process every 10 s. PCA output indices: *C*=spatial complexity, *CV*=spatial complexity variability, *SV*=temporal variability of spectral distribution, *SC*=spectral concentration.

The fraction of variability v_k (cumulative variance) expressed by the first *k* eigenvectors is given by:

$$v_k = \frac{\sum_{i=1}^{k} \lambda_i}{\sum_{i=1}^{M} \lambda_i} \qquad (10.2)$$

where λ_i is the i*th* eigenvalue of the (estimated) covariance matrix R_X.

In the present work, application of PCA had two specific objectives: 1) to measure the spatial complexity of the AA from TQ segments of the ECG (PCA-TQ), and 2) to extract the continuous AA from the ECG for spectral variability analysis (PCA-ECG), as shown in Figure 10.2.

10.2.4.1 PCA-TQ

The PCA-TQ computation consisted of the following steps:

i) ECG delineation: beat detection and time stamp of the fiducial points (T wave end and QRS onset) were automatically annotated for each beat by means of an established discrete-wavelet transform (DWT) based algorithm (Di Marco and Chiari, 2011) for single-lead ECG, adopting CH32 for LS_1, LS_2, and “modified” Lead II for LS_3. The reason for selecting the TQ interval is that it represents the portion of the ECG where the atrial activation is most visible, unobscured by the ventricular activity (Bonizzi *et al.*, 2010). Note that the delineation algorithm provided a beat-by-beat estimation of the TQ segment length, which varied according to the instantaneous heart rate, thus maximising the available AA within the TQ segment.

ii) Time windowing: The recording length of 180 s was divided into N_W (=18) consecutive non-overlapping 10 s windows. The window length of 10 s proposed by Bonizzi and co-workers (Bonizzi *et al.*, 2010) was adopted, as a trade-off between number of collected beats and data stationarity. For each 10 s window, TQ segments of consecutive beats were connected together to form the TQ series. Fig. 3 illustrates construction of the TQ series. The N_{TQ}xM observation matrix X_{TQ} of the TQ series was generated for each window, where N_{TQ} is the number of time samples composing the TQ series, and M is the number of leads in the selected lead-set.

iii) PCA computation: PCA was computed for every instance of X_{TQ}, namely every 10 seconds. Indices computed based on PCA are described in the following section.

It shall be noted, that this entire process does not involve spectral computation, which would lack physical meaning as the TQ series generation (TQ segment concatenation of consecutive beats) generates temporal gaps.

10.2.4.2 PCA-ECG

The PCA-ECG computation was performed in parallel to the above described PCA-TQ, with the goal of separating AA from ventricular activity (Bollmann *et al.*, 2006; Langley *et al.*, 2006; Raine *et al.*, 2004; Raine *et al.*, 2005) by transforming the ECG signal as a whole (i.e. preserving temporal consistency). For each 10 s window, PCA was applied to the N_{ECG}xM observation matrix X_{ECG}, where N_{ECG} is the number of time samples in the ECG signal, and M was the number of leads in the selected lead-set. It shall be noted that $N_{ECG} = 10 \cdot F_S > N_{TQ}$. Spectral analysis was performed on the continuous AA extracted by this method as described in section 10.2.7.

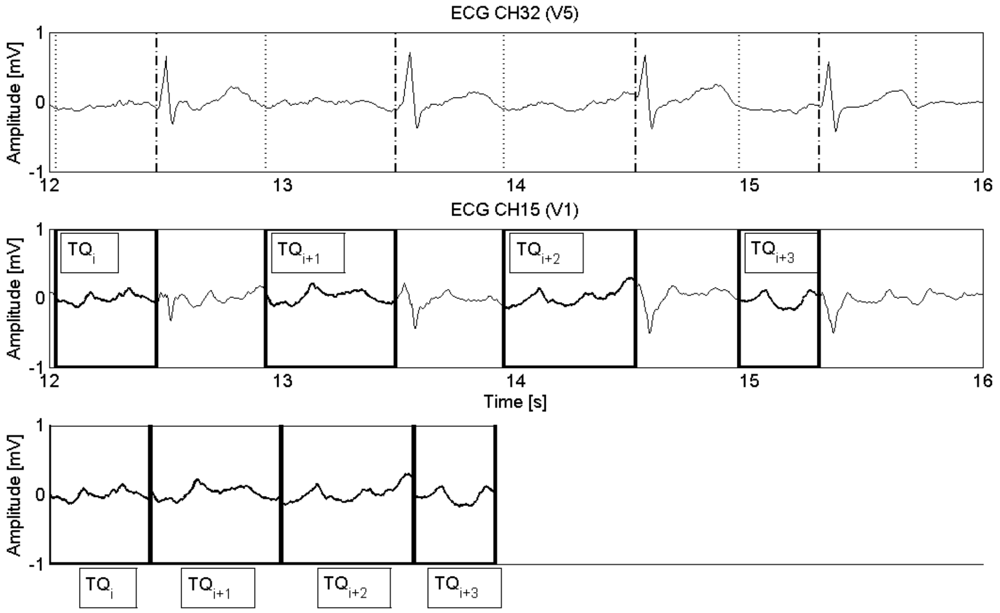

Figure 10.3 ECG delineation (top panel) on an arbitrary portion of recording AF1, TQ segments collected from CH15 (central panel) and TQ series generated by connecting consecutive TQ segments (lower panel). Dashed-dotted lines indicate QRS onset, dotted lines indicate T wave offset.

10.2.5 Spatial complexity

PCA offers the benefit of the intuitive concept of spatial distribution of variance of the signal being analyzed. It is therefore reasonable, as noted in previous studies (Bonizzi *et al.*, 2010; Faes *et al.*, 2001), to quantify spatial complexity in terms of PCA ability to concentrate the original information of the atrial activation signal in only k components ($k<M$), based on the assumption that in AF a more organized AA is reflected in a lower number of principal components (PCs) needed to describe its variance. An index C was defined accordingly, to quantify the spatial complexity of PCA-TQ representation of the X_{TQ} observation matrix. C was defined as the percentage residual cumulative variance of the first three PCs:

$$C=(1-v_3)\cdot 100=\left(1-\frac{\sum_{i=1}^{3}\lambda_i(LS_l)}{\sum_{i=1}^{M}\lambda_i(LS_l)}\right)\cdot 100 \qquad (10.3)$$

where λ_i is the i*th* eigenvalue of PCA-TQ. C indicates the residual variance which is not expressed by the first three PCs. It represents the degree of local complexity of the random process (X_{TQ} observation matrix), with higher values indicating higher degree of complexity. By definition, C ranges from 0 to 100.

10.2.6 Variability of spatial complexity

Spatial complexity variability was quantified in terms of deviation of the spatial complexity index over time. Mathematically, a new index *CV* was defined as:

$$CV = SD(C) \tag{10.4}$$

where *SD(·)* is the standard deviation operator. Lower values of *CV* indicate a higher degree of persistence of the spatial complexity (organization) over time.

10.2.7 Spectral concentration and variability

Spectral variability was quantified in terms of deviation of the power spectral distribution from an average template. Considering the *M* PCs available from PCA-ECG, power spectral density (PSD_{AF}) was estimated for each, in the frequency band of interest for AF (4–10 Hz) (Bollmann *et al.*, 2006; Raine *et al.*, 2004). For PSD_{AF} computation the input signal was preliminarily (first-order) detrended and zero-meaned. Welch periodogram was then applied, with Hamming windowing. Defining $\eta_k(i)$ as the PSD_{AF} of the k*th* PC computed for the i*th* 10 s window, the following templates were calculated:

$$\eta_T^k = \underset{i}{mean}\{\ \eta_k(i)\ \} \tag{10.5}$$

where $\eta^k{}_T$ is the PSD_{AF} template for the *k*th PC, *i* (=1,..., N_W) is the 10 s window index. Considering the definition of spectral concentration by Castells and co-workers (Castells *et al.*, 2005), the following was computed:

$$SC_k = \frac{\sum\limits_{f=f_P-0.5Hz}^{f_P+0.5Hz} \eta_T^k(f)}{\sum\limits_{f\,\min}^{10Hz} \eta_T^k(f)}$$
$$SC = \max_k\{SC_k\} \tag{10.6}$$

where f_P is the peak frequency of $\eta^k{}_T$ in the 4–10 Hz band, and f_{min} is defined as the lowest value between 4 Hz and f_P – 1Hz. SC is a measure of the focus of the spectral power within a narrow band around the dominant AF frequency. Considering the case of AF with highly stable re-entrant circuit, SC will be high. Conversely, in the case of AF with meandering or multiple and changing re-entrant circuits, SC would be comparatively low. As such SC can be regarded as a measure of stability of AF spectral components.

A spectral variability index (*SV*) quantifying temporal variability of spectral distribution was defined as:

$$\begin{aligned} K &= \underset{k}{argmax}\left\{SC(\eta_T^k)\right\} \\ SV &= \underset{i}{mean}\left\{\frac{RMSE(\eta_K(i),\eta_T^K)}{SD(\eta_T^K)}\right\} \end{aligned} \tag{10.7}$$

where *RMSE(·)* is the root-mean-square operator, *SD(·)* is the standard deviation, *i* (=1,..., N_W) is the window index, *K* is the index of the PC whose PSD_{AF} has the highest spectral concentration (i.e. the most prominent peak), and $\eta^K{}_T$ is the PSD_{AF} template obtained by averaging all $\eta_K(i)$.

Lower values of *SV* indicate a higher degree of temporal persistence of the spectral morphology in the band of interest.

A different approach was proposed for “stationarity” analysis by Bonizzi and co-workers (Bonizzi *et al.*, 2010), intended as a measure of repeatability of PCA representation over the sliding time-window. Our approach avoids the potential bias introduced by the (somehow arbitrary) choice of a reference window.

10.2.8 Statistical analysis

The following statistical analysis was undertaken:

I) Spatial complexity and variability of spatial complexity: analysis of variance was done according to the Kruskal-Wallis test (α=0.05) to compare spatial complexity (*C*) and variability of spatial complexity (*CV*) of atrial activation.

II) Temporal variability of spectral distribution and spectral concentration: linear correlation between temporal variability of the power spectral density distribution (*SV*) and the related spectral concentration *SC* was computed.

A significance level of α=0.05 was adopted for the null hypothesis test of non-zero correlation between two samples (two-tail test).

10.3 Results

Table 10.1 shows Pearson’s linear correlation between indices. A significant direct correlation ($\rho(CV, C) \geq 0.80$, $p<0.001$) was observed between spatial complexity (*C*) and its variability (*CV*) suggesting that reduced complexity may be associated with higher degree of temporal stability of spatial organisation. Correlation strength is maintained with decreasing number of leads *M* (from LS_1 to LS_3).

A significant inverse correlation ($\rho(SC, SV) \leq -0.83$, $p<0.001$) was observed between spectral variability index *(SV)* and spectral concentration (*SC*), indicating an inverse relationship between the prominence of the dominant AF frequency (DF) and the temporal variability of the spectral distribution in the AF frequency range. In other words, a more pronounced AF frequency peak was associated with a more temporally stable spectral distribution. Figure 10.4 shows linear regression for the indices pairs presented in Table 10.1.

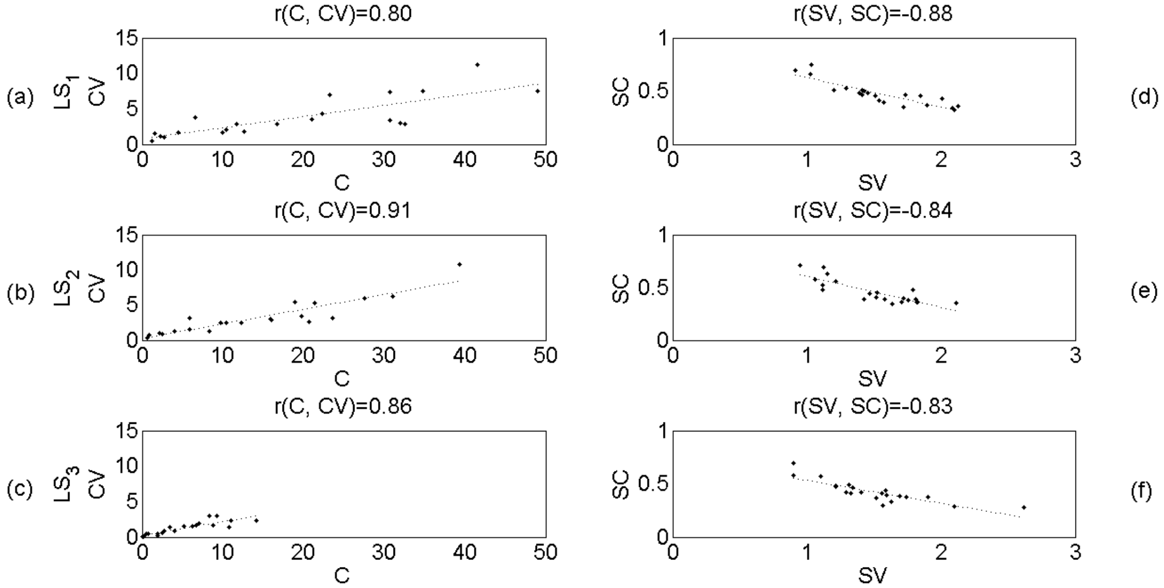

Figure 10.4 Linear correlation between spatial complexity (*C*) and spatial complexity variability (*CV*) for all lead-sets (panels a-c); between spectral variability (*SV*) and spectral concentration (S*C*) (panels d-f). All indices are dimensionless.

Table 10.1 – Linear correlation between indices (two-tail test).

Lead-set	$\rho_{CV,C}$	$\rho_{SC,SV}$
LS_1	0.80 ($p<0.001$)	-0.88 ($p<0.001$)
LS_2	0.91 ($p<0.001$)	-0.84 ($p<0.001$)
LS_3	0.86 ($p<0.001$)	-0.83 ($p<0.001$)

Abbreviations: *C*=spatial complexity, *CV*= variability of spatial complexity, *SV*=temporal variability of spectral distribution, *SC*=spectral concentration.

In Figure 10.5 contrasting cases of lowest vs. highest spatial complexity (panels a-c) and temporal spectral variability (panels d-f), for lead set LS_1 are shown. Extreme values of *C* and *SV* are highlighted in top panels. Panel b (c) shows an arbitrary strip of 4 s of the TQ series from the recording with lowest (highest) spatial complexity for all 64 channels simultaneously (*C*, *CV* are computed from PCA-TQ, as illustrated in Figure 10.2). Panel e (f) shows an arbitrary strip of 4 s of ECG from the recording with lowest (highest) spectral variability (SC, SV are computed from PCA-ECG, as illustrated in Figure 10.2).

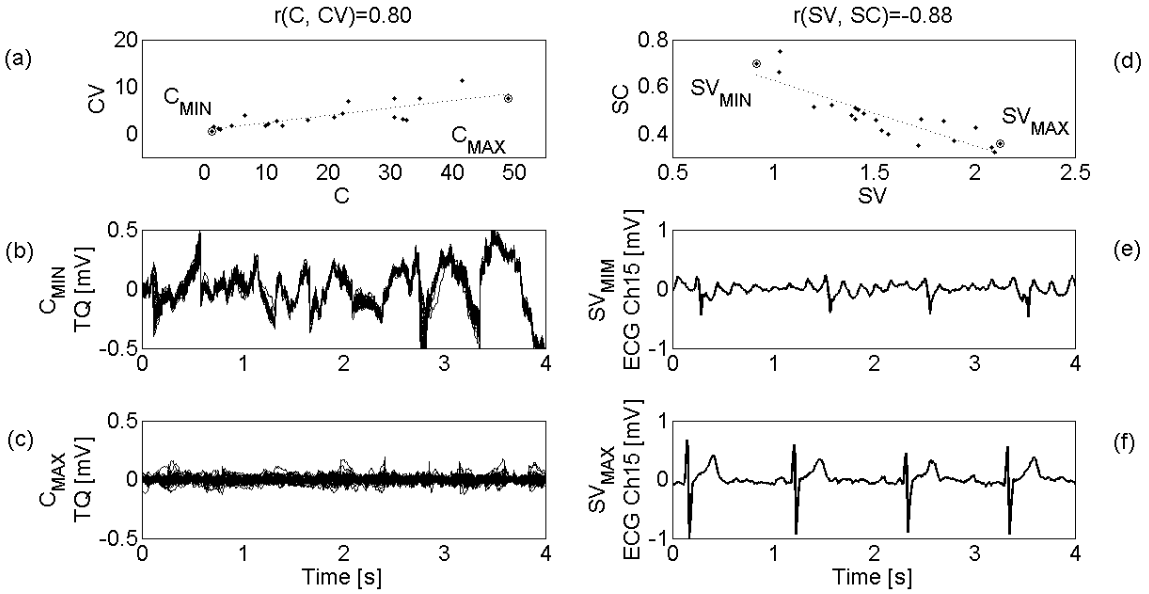

Figure 10.5 Contrasting cases of lowest vs. highest spatial complexity (panels a-c) and temporal spectral variability (panels d-f), for lead set LS_1. Circle-dot highlight on top panels shows extrema of C and SV. Panel b (c) shows an arbitrary strip of 4 s of the TQ series from the recording with lowest (highest) spatial complexity for all 64 channels simultaneously (overlapped traces). Panel e (f) shows an arbitrary strip of 4 s of of ECG from the recording with lowest (highest) spectral variability.

10.4 Discussion

The first aim of the present study was to analyze the variability of spatial organization (complexity) and spectral distribution of AF in BSPM, proposing an automated method for the analysis. A DWT-based ECG delineation algorithm (Di Marco and Chiari, 2011) was adopted for the purpose, to automatically generate the TQ time-series for spatial organization analysis.

Significant direct correlation ($p<0.001$) between spatial complexity (C) and its variability (CV) was found (Table 10.1) suggesting that higher spatial organization may be associated with more temporally stable atrial activation pattern, in accordance with the wavelet theory of AA in AF (Konings *et al.* 1994; Moe and Abildskov, 1959; Moe *et al.*, 1964; Wijffels *et al.*, 1995).

A strong inverse correlation ($p<0.001$) between temporal variability of the PSD spectrum in the AF band of interest (SV) and spectral concentration (SC) was also observed, suggesting that higher temporal persistence (regularity) of spectral distribution in the AF band may be associated with a more pronounced dominant fibrillatory frequency. To the authors' knowledge this is the first contribution to the quantification of such relationship in AF from surface ECG recordings.

The second aim was to assess the applicability of the proposed analysis to a reduced set of BSPM signals. Decreasing the number of leads M (i.e. the number of PCs) from 64 (32 anterior, 32 posterior channels) to 32 (anterior) improved correlation between spatial complexity (*C*) and spatial complexity variability (*CV*) as shown in Table 10.1 and Figure 10.4. This may be due to the position of the posterior electrodes which are farther away from the heart, and consequently less sensitive to the low amplitude atrial activity signal. Moreover, BSPM signals from posterior electrodes are also sensitive to slight body motion of the patient lying supine on the bed. Combined together, these two factors may suggest that posterior channels do not contribute to PCA analysis of spatial complexity, rather they act as source of noise.

Decreasing M to the lowest value (M=10) in LS_3, dramatically reduced the range of values of C and CV, as would be expected due to the decreased number of PCs. However, the strong correlation between C and CV was preserved, showing that the relationship persisted with the selected channels.

Correlation between spectral variability (*SV*) and spectral concentration (*SC*) was also not affected by decreasing M, as shown in Table 10.1 and Figure 10.4, suggesting that spectral information is preserved in the available PCs. Hence lead-set LS_3 may still carry spatial and spectral variability information in spite of a reduced number of leads.

In conclusion, in this work, higher spectral concentration (*SC*) was associated with reduced temporal variability of spectral distribution (*SV*). This may indicate that with higher values of *SC*, a shorter observation time is required to collect spectral distribution, from which the dominant atrial fibrillatory rate (a recognized index of average atrial refractoriness) can be calculated. This could be time and cost effective in clinical decision-making in AF treatment.

Moreover, it was shown that the results are not affected by the reduction of the number of leads (M), down to as few as 10 BSPM (LS_3). This may suggest that a simplified setup could also be considered, further reducing the cost of the BSPM acquisition protocol or that the methods could be applied equally to standard 12-lead ECG.

Lastly, reduced complexity (*C*) was associated with reduced complexity variability (*CV*) for all lead-sets, indicating that lower complexity AF cases might require shorter observation time for complexity index calculation. However, replication on a larger dataset would be necessary to validate the proposed indices.

References

Alcaraz R, Rieta JJ. Surface ECG organization analysis to predict paroxysmal atrial fibrillation termination. *Comput Biol Med* 2009; 39(8): 697–706.

Alcaraz R, Rieta JJ. The application of nonlinear metrics to assess organization differences in short recordings of paroxysmal and persistent atrial fibrillation. *Physiol Meas* 2010; 31(1): 115–30.

Asano Y, Saito J, Matsumoto K, Kaneko K, Yamamoto T, Uchida M. On the mechanism of termination and perpetuation of atrial fibrillation. *Am J Cardiol* 1992; 69(12): 1033–38.

Bollmann A, Husser D, Mainardi L, Lombardi F, Langley P, Murray A, Rieta JJ, Millet J, Olsson B, Stridh M, Sörnmo L. Analysis of surface electrocardiograms in atrial fibrillation: techniques, reseach, and clinical applications. *Europace* 2006; 8(11): 911–26.

Bonizzi P, de la Salud Guillem M, Climent AM, Millet J, Zarzoso V, Castells F, Meste O. Noninvasive assessment of the complexity and stationarity of the atrial wavefront patterns during atrial fibrillation. *IEEE Trans Bomed Eng* 2010; 57(9): 2147–57.

Castells F, Rieta JJ, Millet J, Zarzoso V. Spatiotemporal blind source separation approach to atrial activity estimation in atrial tachyarrhythmias. *IEEE Trans Bomed Eng* 2005; 52(2): 258–67.

Censi F, Barbaro V, Bartolini P, Calcagnini G, Michelucci A, Gensini GF, Cerutti S (2000) Recurrent patterns of atrial depolarization during atrial fibrillation assessed by recurrence plot quantification. *Ann Biomed Eng* 2000; 28(1):61-70.

Di Marco LY, Chiari L. A wavelet-based ECG delineation algorithm for 32-bit integer online processing. *Biomed Eng Online* 2011; 10(23).

Faes L, Nollo G, Kirchher M, Olivetti E, Gaita F, Riccardi R, Antolini R. Principal component analysis and cluster analysis for measuring the local organisation of human atrial fibrillation. *Med Biol Eng Comput* 2001; 39: 656–63.

Gerstenfeld EP, Sahakian AV, Swiryn S. Evidence for transient linking of atrial excitation during atrial fibrillation in humans. *Circulation* 1992; 86(2):375–82.

Konings KT, Kirchhof CJ, Smeets JR, Wellens HJ, Penn OC, Allessie MA. High-density mapping of electrically induced atrial fibrillation in humans. *Circulation* 1994; 89(4): 1665–80.

Langley P, Rieta JJ, Stridh M, Millet-Roig J, Sörnmo L, Murray A. Comparison of atrial signal extraction algorithms in 12-lead ECGs with atrial fibrillation. *IEEE Trans Bomed Eng* 2006; 53(2):343-346.

Moe GK, Abildskov JA. Atrial fibrillation as a self-sustaining arrhythmia independent of focal discharge. *Am Heart J* 1959; 58:59–70.

Moe GK, Rheinboldt WC, Abildskov JA. A computer model of atrial fibrillation. *Am Heart J* 1964; 67: 200–220.

Raine D, Langley P, Murray A, Dunuwille A, Bourke JP. Surface atrial frequency analysis in patients with atrial fibrillation: A tool for evaluating the effects of intervention. *J Cardiovasc Electrophysiol* 2004; 15:1021–1026.

Raine D, Langley P, Murray A, Furniss SS, Bourke JP. Surface atrial frequency analysis in patients with atrial fibrillation: Assessing the anti-arrhythmic effects of linear atrial lesions. *J Cardiovasc Electrophysiol* 2005; 16:838–844.

Richter U, Faes L, Cristoforetti A, Masè M, Ravelli F, Stridh M, Sörnmo L. A novel approach to propagation pattern analysis in intracardiac atrial fibrillation signals. *Ann Biomed Eng* 2011; 39(1):310–23.

Sih HJ, Zipes DP, Barbari EJ, Olgin JE. A high-temporal resolution algorithm for quantifying organization during atrial fibrillation. *IEEE Trans Bomed Eng* 1999; 46(4): 440–50.

Wijffels MC, Kirchhof CJ, Donald R, Allessie MA. Atrial fibrillation begets atrial fibrillation: a study in awake chronically isntrumented goats. *Circulation* 1995; 92(7): 1954–68.

Conclusions

The aim of this PhD thesis was to analyze the variability of surface ECG derived rhythms, at two different time scales: the discrete-event time scale, typical of beat-by-beat extracted features, and the “continuous” time scale of separated (in-band filtered) sources in the ECG, in selected scenarios relevant to psychophysiological and clinical research, respectively.

Variability analysis of discrete event series: the discrete event series (DES) of inter-beat interval (IBI) was considered. Heart rate variability (HRV) analysis was carried out in the time, frequency, and joint time-frequency domain, complemented by non-linear dynamics analysis, with the goal of assessing psychophysiological workload (PPW) in response to working memory engaging tasks.

A superior ability of regularity index (SampEn) in discriminating performance (task execution) from rest; and instantaneous energy variability (IEV_{LF+HF}) in discriminating difficult tasks from other sessions (rest and easy tasks) was shown in fourteen healthy young subjects, with respect to traditional HRV analysis, suggesting a potential use of the proposed indices in discriminating PPW levels in response to varying memory-search task difficulty.

Variability analysis of wavefront patterns: the atrial activation signal (AA) from atrial fibrillation (AF) recordings was considered. The signal was estimated from 64-channels body surface potential maps (BSPM). The goal was to analyze the temporal variability of spatial organization (complexity) and spectral distribution of AF, to propose an automatic implementation of the analysis, and to assess the applicability to reduced lead-sets, to potentially support clinical decision making in AF ablation therapy.

A novel source-cancellation method based on morphology clustering of the ventricular depolarization interval (QRS-T segment) was proposed for the estimation of the atrial activation wavefront in AF. A significant improvement in ventricular activity cancellation was shown with respect to established single-lead approaches in BSPM recordings, together with a reliable estimation of AF dominant frequency (DF).

Combined analysis of spatial complexity and spectral variability of atrial activation during AF was presented for BSPM recordings, based on a fully automated procedure. It was shown in twenty one patients with persistent AF that higher spectral concentration (SC) was associated with reduced temporal variability of spectral distribution. This finding suggests that with higher values of SC, a shorter observation time is required to collect spectral distribution, from which the dominant atrial fibrillatory rate (a recognized index of average atrial refractoriness) can be calculated. This could be time and cost effective in clinical decision-making in AF treatment. Moreover, it was shown that the results were not affected by the reduction of the number of leads, down to as few as 10 body surface potential maps (BSPM). This may suggest that a simplified setup could also be considered, further reducing the cost of the BSPM acquisition protocol or that the methods could be applied equally to standard 12-lead ECG.

In designing the methods for the two main objectives of the thesis, an online approach to signal processing was kept as general guideline, with the goal of contributing to real-world applicability of the proposed methods.

In this regard, an algorithm for automatic assessment of ambulatory ECG signal quality, and an automatic ECG delineation algorithm were designed and validated.

Automatic assessment of ambulatory ECG signal quality. An algorithm for the automatic assessment of ambulatory ECG recording quality, based on single-condition decision rule (SCDR) classification, was presented. Its performance in binary classification (‘acceptable’ vs. ‘unacceptable’ recording quality for diagnostic interpretation) was assessed on a standard database and compared to established supervised-learning classifiers (k-nearest neighbor, probabilistic neural network).

The proposed method showed high accuracy (Sc) in automatic classification of short 12-leads ambulatory ECG recordings (Sc=92.36%, for balanced training set; 93.40%, for unbalanced training set), higher than the best-performing supervised-learning classifier, in spite of its simple logic. The ability to provide additional information (rejection reason) to the classification output, suggests the proposed method may be a useful tool in automatic quality assessment of 12-leads ambulatory ECG recordings.

Automatic electrocardiogram delineation. A wavelet-based ECG delineation algorithm was presented, designed for online 32-bit integer linear algebra processing, with shift/add operations replacing multiplications and divisions. The QRS detector achieved excellent performance on standard databases (MIT-BIH Arrhythmia database, European ST-T Database), and very good accuracy in P, QRS, T delineation on the standard QT Database. Reliability and accuracy were close to the highest among the ones obtained in other studies, in spite of a simplified structure built on integer linear algebra which makes the proposed algorithm a suitable candidate for online QRS detection and ECG delineation under strict power constraints and limited computational resources, such as in wearable devices for long-term non-diagnostic ambulatory monitoring.

List of publications

Peer-reviewed international journals

Di Marco LY and Chiari L. A wavelet-based ECG delineation algorithm for 32-bit integer online processing. *Biomed Eng Online* 2011 Apr 3;10:23.

Di Marco LY, Bourke JP, Langley P. Spatial complexity and spectral distribution variability of atrial activity in surface ECG recordings of atrial fibrillation. *Med Biol Eng Comp* [in press]

Langley P, Dewhurst M, Di Marco LY, Adams P, Dewhurst F, Mwita J, Walker R, Murray A. Accuracy of algorithms for detection of atrial fibrillation from short duration beat interval recordings. *Med Eng Phys* [in press]

Dewhurst M, Di Marco LY, Langley P, Adams PC, Dewhurst F, Murray A, Orega GP, Mwita JM, Walker RW. Electrocardiographic P Wave Indices in an Elderly Tanzanian Population. *Europace* [conditionally accepted for publication 27 Jan 2012]

International conferences proceedings

Di Marco LY, Sottile R, Chiari L. Time-Frequency analysis of cardio-respiratory response to mental task execution. *Comput Cardiol* 2010;37:753−756.

Di Marco LY, King S, Bourke JP, Chiari L, Murray A, Langley P. Time-frequency analysis of atrial fibrillation comparing morphology-clustering based QRS-T cancellation with blind source separation in multi-lead surface ECG recordings. *Comput Cardiol* 2011; 38:269−272.

Langley P, Di Marco LY, King S, Di Maria C, Duan W, Bojarnejad M, Wang K, Zheng D, Allen J, Murray A. An algorithm for assessment of ECG quality acquired via mobile telephone. *Comput Cardiol* 2011; 38:281−284.

National conferences proceedings

Di Marco LY, Sottile R, Chiari L. Comparative Analysis Of Heart- And Pulse- Rate Variability During Mental Task Execution: The Role Of Pulse Transit Time Variability. Atti Congresso Nazionale di Bioingegneria 2010 (*proceedings of the national conference in biomedical engineering 2010*), Ed. Patron, pp 481−482.

Di Marco LY, Sottile R, Chiari L. Effects Of Working Memory Demand On Short-Term Heart Rate- And Pulse Transit Time- Variability. Atti Congresso Nazionale di Bioingegneria 2010 (*proceedings of the national conference in biomedical engineering 2010*), Ed. Patron, pp 483−484